Magnetic exchange interactions in BaMn₂As₂: A case study of the J_1-J_2-J_c Heisenberg model

D. C. Johnston,[1,2] R. J. McQueeney,[1,2] B. Lake,[3,4] A. Honecker,[5] M. E. Zhitomirsky,[6,7] R. Nath,[1,*] Y. Furukawa,[1,2]
V. P. Antropov,[1] and Yogesh Singh[1,†]

[1]*Ames Laboratory, Iowa State University, Ames, Iowa 50011, USA*
[2]*Department of Physics and Astronomy, Iowa State University, Ames, Iowa 50011, USA*
[3]*Hahn-Meitner-Institut, Glienicker Straße 100, D-14109 Berlin, Germany*
[4]*Institut für Festkörperphysik, Technische Universität Berlin, Hardenbergstraße 36, D-10623 Berlin, Germany*
[5]*Institut für Theoretische Physik, Universität Göttingen, D-37077 Göttingen, Germany*
[6]*Service de Physique Statistique, Magnétisme et Supraconductivité, UMR-E9001 CEA-INAC/UJF, 17 rue des Martyrs,
F-38054 Grenoble Cedex 9, France*
[7]*Max-Planck-Institut für Physik Komplexer Systeme, Nöthnitzer Straße 38, D-01187 Dresden, Germany*

BaMn₂As₂ is unique among BaT_2As₂ compounds crystallizing in the body-centered-tetragonal ThCr₂Si₂ structure, which contain stacked square lattices of $3d$ transition metal T atoms, since it has an insulating large-moment (3.9 μ_B/Mn) G-type (checkerboard) antiferromagnetic (AF) ground state. We report measurements of the anisotropic magnetic susceptibility χ versus temperature T from 300 to 1000 K of single crystals of BaMn₂As₂, and magnetic inelastic neutron scattering measurements at 8 K and ⁷⁵As nuclear magnetic resonance (NMR) measurements from 4 to 300 K of polycrystalline samples. The Néel temperature determined from the $\chi(T)$ measurements is $T_N = 618(3)$ K. The measurements are analyzed using the J_1-J_2-J_c Heisenberg model for the stacked square lattice, where J_1 and J_2 are, respectively, the nearest-neighbor (NN) and next-nearest-neighbor intraplane exchange interactions and J_c is the NN interplane interaction. Linear spin wave theory for G-type AF ordering and classical and quantum Monte Carlo simulations and molecular field theory calculations of $\chi(T)$ and of the magnetic heat capacity $C_{mag}(T)$ are presented versus J_1, J_2, and J_c. We also obtain band-theoretical estimates of the exchange couplings in BaMn₂As₂. From analyses of our $\chi(T)$, NMR, neutron scattering, and previously published heat capacity data for BaMn₂As₂ on the basis of the above theories for the J_1-J_2-J_c Heisenberg model and our band-theoretical results, our best estimates of the exchange constants in BaMn₂As₂ are $J_1 \approx 13$ meV, $J_2/J_1 \approx 0.3$, and $J_c/J_1 \approx 0.1$, which are all antiferromagnetic. From our classical Monte Carlo simulations of the G-type AF ordering transition, these exchange parameters predict $T_N \approx 640$ K for spin $S = 5/2$, in close agreement with experiment. Using spin wave theory, we also utilize these exchange constants to estimate the suppression of the ordered moment due to quantum fluctuations for comparison with the observed value and again obtain $S = 5/2$ for the Mn spin.

I. INTRODUCTION

The observations of superconductivity up to 56 K in several classes of Fe-based superconductors in 2008 (Refs. [1–4]) have reinvigorated the high-T_c field following the discovery of high-T_c superconductivity in the layered cuprates 25 years ago.[5,6] Interestingly, the Fe atoms have the same layered square lattice structure as the Cu atoms do. Even though the maximum T_c of the Fe-based materials is far below the maximum T_c of 164 K for the cuprates,[7] the Fe-based materials have generated much interest because the superconductivity appears to be caused by a magnetic mechanism[4] as also appears to be the case in the cuprates. One of the many motivations for carrying out detailed measurements on the Fe-based materials is to see if these studies can clarify the superconducting mechanism in the high-T_c cuprates for which a clear consensus has not yet been reached despite 25 years of intensive research.

Many studies of the magnetic properties of the Fe-based superconductors have been carried out.[4,8] For the FeAs-based materials such as Ba₁₋ₓKₓFe₂As₂ with the body-centered-tetragonal ThCr₂Si₂ structure, the magnetic susceptibility χ increases approximately linearly with increasing temperature above T_c or above the Néel temperature T_N of the non-superconducting parent compounds up to at least 700 K.[9,10]

In a model of local magnetic moments on a square lattice with strong antiferromagnetic (AF) Heisenberg interactions, this type of behavior is explained as being due to the measurement temperature (T) range being on the low-T side of a broad maximum in $\chi(T)$ at higher temperatures.[6] On the other hand, many magnetic measurements of the FeAs-based superconductors have been explained in terms of itinerant magnetism models, and indeed the consensus is pointing in this direction, although this view is not universal.[4]

In this context it is very useful to have a benchmark compound with the same ThCr₂Si₂-type structure and similar composition as many of the Fe-based superconductors, but for which a local moment model must be used to explain the magnetic properties. Such a compound is BaMn₂As₂ because it has an insulating ground state.[11,12] The crystal structure of BaMn₂As₂ is shown in Fig. 1.[13] It is a small-band-gap semiconductor[11,12] with an activation energy of 30 meV.[11] The electronic structure calculations of An *et al.*[12] for the predicted conventional G-type (checkerboard) AF state give a small band gap of 0.1–0.2 eV, qualitatively consistent with the experimental value of the activation energy[11] that is expected to be a lower limit to half the band gap. The anisotropic χ of single crystals was previously measured
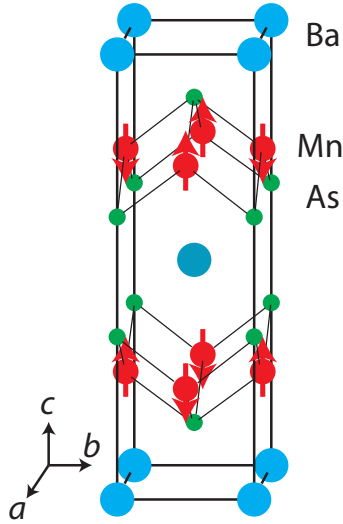
FIG. 1. (Color online) Crystal and magnetic structures of BaMn$_2$As$_2$ (Ref. [13]). The crystal structure is body-centered-tetragonal ThCr$_2$Si$_2$-type in which the Mn atoms form a square lattice within the *ab* plane, the axes of which are rotated by 45° with respect to the **a** and **b** unit cell axes. The Mn atoms in adjacent layers are directly above or below each other along the *c* axis. The magnetic structure is a G-type antiferromagnetic structure in which the magnetic moments of nearest-neighbor spins are antiparallel both in the *ab* plane and along the *c* axis. The ordered moment at $T = 0$ is 3.9(1) μ_B/Mn.[13]

at $T \leqslant 400$ K.[11] These data indicate that the compound is in a collinear AF state at these temperatures, with the ordered moment direction along the *c* axis and with a T_N significantly above 400 K. From subsequent magnetic neutron powder diffraction measurements, the Néel temperature was determined to be $T_N = 625(1)$ K and the AF structure was found to be a conventional G-type (checkerboard) structure in all three directions, as shown in Fig. 1, with an ordered moment direction along the *c* axis in agreement with the $\chi(T)$ data and with an ordered moment $\mu = 3.9(1)$ μ_B/Mn at 10 K, where μ_B is the Bohr magneton.[13] These characteristics are radically different from those of the similar FeAs-based metallic parent compound BaFe$_2$As$_2$ with the same room temperature crystal structure. BaFe$_2$As$_2$ has a much smaller ordered moment $\mu \approx 0.9$ μ_B/Fe and much smaller $T_N = 137$ K than BaMn$_2$As$_2$, the structure of BaFe$_2$As$_2$ distorts to orthorhombic symmetry below a temperature $T_S \approx T_N$ instead of remaining tetragonal as in BaMn$_2$As$_2$, the ordered moment direction is in the *ab* plane instead of along the *c* axis, and the in-plane AF structure is a stripe structure (see the bottom panel of Fig. 2 below) instead of G type.[4] These large differences between the magnetic properties of BaMn$_2$As$_2$ and BaFe$_2$As$_2$ evidently arise because BaMn$_2$As$_2$ is a local moment antiferromagnet, whereas BaFe$_2$As$_2$ is an itinerant antiferromagnet.

An intriguing aspect of the in-plane electrical resistivity $\rho(T)$ data for BaMn$_2$As$_2$ single crystals is that above ∼100 K the slope of the resistivity versus temperature changes from negative (semiconductor-like) to positive (metal-like).[11,12] The $\rho(T)$ of a material can be written in an effective single carrier

model as

$$\rho(T) = \frac{1}{e\, n(T)\mu(T)}, \quad (1)$$

where e is the magnitude of the electron charge, and $n(T)$ and $\mu(T)$ are, respectively, the effective conduction carrier density and the effective carrier mobility, respectively. Thus, a positive temperature coefficient of resistivity can be obtained for a band semiconductor if the increase in carrier concentration with increasing temperature is slower than the decrease in mobility with increasing temperature. Our ^{75}As nuclear magnetic resonance (NMR) measurements in Sec. XI were, in fact, initially motivated in order to address this issue. As stated in that section, we found no evidence for a Korringa contribution to the ^{75}As nuclear spin-lattice relaxation rate that would have indicated metallic behavior, and indeed we could interpret the data from 50 to 300 K in terms of a local moment insulator model. Furthermore, there is no evidence from the previously published neutron diffraction,[13] resistivity, or heat capacity[11,12] measurements for any phase transition from a band insulator at low temperatures to a metal at high temperatures. Thus, in the absence of experimental data to the contrary, our present interpretation of the positive temperature coefficient of resistivity above ∼100 K is as discussed below Eq. (1) above.

A related Mn-based compound is Sr$_2$Mn$_3$As$_2$O$_2$, which consists of Mn$_2$As$_2$ layers that are the same as in BaMn$_2$As$_2$, alternating along the *c* axis with MnO$_2$ layers with the same structure as the CuO$_2$ layers in the layered cuprate superconductor parent compounds.[14] Due to geometric frustration effects, the Mn spins in the MnO$_2$ layers do not show any obvious long-range magnetic ordering for $T \geqslant 4$ K, but the Mn spins in the Mn$_2$As$_2$ layers show long-range G-type AF ordering below $T_N = 340$ K with a low-temperature ordered moment $\mu = 3.50(4)$ μ_B/Mn.[14,15] Thus, in both BaMn$_2$As$_2$ and Sr$_2$Mn$_3$As$_2$O$_2$, the Mn spins in the Mn$_2$As$_2$ layers exhibit the same G-type AF structure and significant reductions in the ordered moments from the value $\mu = gS\mu_B = 5$ μ_B/Mn that would be expected for the high-spin $S = 5/2$ d^5 Mn^{+2} ion with spectroscopic splitting factor $g = 2$.

The main goal of the present work was to determine the magnitudes of the exchange interactions in the fiducial compound BaMn$_2$As$_2$ and their signs, that is, AF or ferromagnetic (FM). Experimentally, we extend the single-crystal anisotropic $\chi(T)$ measurements from 300 to 1000 K, significantly above T_N. We also report inelastic magnetic neutron scattering measurements at 8 K and ^{75}As NMR measurements from 4 to 300 K on polycrystalline samples. We analyze these data using the J_1-J_2-J_c Heisenberg stacked square spin-lattice model for which we develop extensive theory. This model has also been investigated recently by other groups.[16–23] We calculate the spin wave dispersion relations for this model. We report classical and quantum Monte Carlo simulations and molecular field theory calculations of $\chi(T)$ and the magnetic heat capacity $C_{mag}(T)$. We extract the values of J_1, J_2, and J_c by fitting our experimental data for BaMn$_2$As$_2$ by these theoretical predictions for the J_1-J_2-J_c model. From our classical Monte Carlo simulations of the heat capacity of coupled layers, we derive a formula for T_N versus the exchange parameters which yields a T_N very close to experiment

from the independently derived exchange constants, which indicates that the spin on the Mn ions is 5/2. We also utilize these exchange constants to determine from spin wave theory the suppression of the ordered moment due to quantum fluctuations for comparison with the observed value and again arrive at the estimate of $S = 5/2$ for the spin of the Mn^{+2} ions when the additional expected suppression of the ordered moment due to hybridization and/or to charge and/or magnetic moment amplitude fluctuations, which arise from both on-site and intersite interactions, are taken into account. Finally, we report band-theoretical calculations of J_1, J_2, and J_c for $BaMn_2As_2$.

The applicability of the local moment Heisenberg model to a specific compound depends on the degree of variation of atomic magnetic moments and interatomic exchange parameters found from electronic structure calculations for the relevant magnetic ordering configurations. Such variations are usually found to be small in magnetic insulators. In the case of $BaMn_2As_2$, our band theory analysis in Sec. XII indicates that insulating character is conserved for both the Néel and stripe antiferromagnetic structures, as observed, with a tiny metallicity appearing in the ferromagnetic case. As noted above, An *et al.* previously estimated that the band gap is 0.1–0.2 eV from electronic structure calculations for G-type AF order in $BaMn_2As_2$.[12] Moreover, our direct calculations of the atomic magnetic moment and exchange couplings for different spin configurations demonstrate that the ordered moment variations do not exceed 10%–12%, while the exchange coupling variation is only about 5%. The largest change appears for the ferromagnetic state, which, due to its high energy, is expected to contribute little to thermodynamic properties. Finally, our determination of a self-consistent set of antiferromagnetic exchange coupling parameters in $BaMn_2As_2$ from both static and dynamic experiments confirms the validity of our analyses in terms of the local moment Heisenberg model.

The remainder of the paper is organized as follows. The experimental details for the sample preparation and characterization of $BaMn_2As_2$ and for the various measurements are given in Sec. II. The J_1-J_2-J_c Heisenberg model is introduced and defined in Sec. III. The inelastic neutron scattering measurements of polycrystalline $BaMn_2As_2$ and the analysis of these data are presented in Sec. IV. This includes the presentation of spin wave theory for the J_1-J_2-J_c model of the G-type antiferromagnet in Sec. IV A that is used to fit the neutron data and to later obtain an estimate of the spin wave contribution to the heat capacity at low temperatures in Sec. VIII B and to analyze the ^{75}As nuclear spin-lattice relaxation NMR data below T_N in Sec. XI B. The high-temperature anisotropic magnetic susceptibility measurements of single crystals of $BaMn_2As_2$ are presented in Sec. V. The predictions of molecular field theory (MFT) and related topics for the J_1-J_2-J_c Heisenberg model are given in Secs. VI and VII and the Appendices. Comparisons of the MFT predictions with our experimental $\chi(T)$, $C_p(T)$, and ordered moment $\mu(T)$ data for $BaMn_2As_2$ are given in Sec. VIII. In this section we also calculate the spin wave contribution to the heat capacity at low temperatures assuming a negligible anisotropy gap in the spin wave spectrum and compare this contribution with the experimental heat capacity data at low

temperatures. Classical and quantum Monte Carlo simulations of T_N, $\chi(T)$, and $C_{mag}(T)$ in the J_1-J_2-J_c Heisenberg model are presented in Sec. IX and comparisons with the experimental T_N and $\chi(T > T_N)$ data are carried out in Sec. X. The NMR measurements and analysis are given in Sec. XI, and our band-theoretical estimates of the exchange couplings in $BaMn_2As_2$ are presented in Sec. XII. Our spin wave theory results for the suppression of the ordered moment are given in Sec. XIII. From a comparison with the experimental ordered moment, we infer that the spin on the Mn ions is 5/2. A summary of our results and of our most reliable values of the J_1, J_2, and J_c exchange constants and of the spin value derived for the Mn ions in $BaMn_2As_2$ is given in Sec. XIV.

II. EXPERIMENTAL DETAILS

A 25-g polycrystalline sample of $BaMn_2As_2$ was prepared by solid state synthesis for inelastic neutron scattering (INS) measurements. Stoichiometric amounts of Ba dendritic pieces (Aldrich, 99.9%), Mn powder (Alfa Aesar, 99.9%), and As chunks (Alfa Aesar, 99.9%) were ground and mixed together in a He-filled glovebox, pelletized, placed in a 50-mL Al_2O_3 crucible with a lid and sealed in a quartz tube under a 0.5 atm pressure of Ar gas (99.999%). The tube was placed in a box furnace and heated at a rate of 50 °C/h to 575 °C and kept there for 24 h. The furnace was then heated at 100 °C/h to 800 °C and kept there for 48 h before cooling to room temperature by turning off the furnace. The quartz tube was opened inside the glovebox and the product was ground and mixed thoroughly and pelletized again. The pellet was placed in the same crucible and sealed again in a quartz tube. The quartz tube was heated in the box furnace at 100 °C/h to 850 °C and kept there for 24 h and then heated at 100 °C/h to 900 °C and kept there for 24 h, followed by furnace cooling at ∼300 °C/h to room temperature. The resulting product was ground and pelletized and the above heat treatment was repeated. The resulting product was characterized by x-ray powder diffraction and the majority phase (≈83%) was found to be the desired $ThCr_2Si_2$ structure. The major impurity phase was identified to be tetragonal $Ba_2Mn_3As_2O$. $BaMn_3As_2O$ is an insulator, shows low-dimensional magnetic behavior with a broad maximum in $\chi(T)$ at 100 K and antiferromagnetic ordering at ≈75 K.[24,25] From x-ray diffraction measurements the weight fraction of this impurity phase in the INS sample was estimated to be ≈17%. The INS spectra at 8 K and at 100 K (not shown) exhibited no noticeable differences. Since 100 K is well above the purported ordering temperature of the impurity phase, this eliminates any concern for serious contamination of the magnetic INS data by this phase.

About 20 g of the above material was used for INS measurements. About 5 g of the polycrystalline material was used to grow single crystals. About 3 g of polycrystalline $BaMn_2As_2$ and 20 g of Sn flux (Alfa Aesar, 99.999%) were placed in an Al_2O_3 crucible and sealed in a quartz tube. The crucible was heated at 250 °C/h to 1000 °C and kept there for 24 h and then cooled at 5 °C/h to 575 °C and kept there for 5 h at which point the Sn flux was centrifuged off to give isolated single crystals of typical dimension $5 \times 5 \times 0.2$ mm^3. Energy-dispersive x-ray (EDX) measurements using a Jeol

scanning electron microscope confirmed the composition of the crystals to be $BaMn_2As_2$.

For the INS measurements, the powder sample of mass ≈ 20 g was characterized for phase purity by x-ray powder diffraction as discussed above. The INS measurements were performed on the Pharos spectrometer at the Lujan Center of Los Alamos National Laboratory. Pharos is a direct geometry time-of-flight spectrometer and measures the scattered intensity over a wide range of energy transfers $\hbar\omega$ and angles between $1°$ and $140°$ allowing determination of the scattered intensity $S(Q,\omega)$ over large ranges of momentum transfer $\hbar Q$ and $\hbar\omega$. The powder sample was packed in a flat aluminum can oriented at $135°$ to the incident neutron beam, and INS spectra were measured with incident energies E_i of 150 and 200 meV. The data were measured at a temperature $T = 8$ K, well below the antiferromagnetic ordering temperature of 625 K.[13] The time-of-flight data were reduced into $\hbar\omega$ and scattering angle (2θ) histograms and corrections for detector efficiencies, empty can scattering, and instrumental background were performed.

The high-temperature anisotropic $\chi(T)$ measurements of a $BaMn_2As_2$ single crystal took place in a physical properties measurement system (PPMS, Quantum Design, Inc.) at the Laboratory for Magnetic Measurements at the Helmholtz Zentrum Berlin für Materialien und Energie. For these measurements the vibrating sample magnetometer option was used. Data were collected with the magnetic field applied both parallel and perpendicular to the Mn layers. For field pointing within the ab plane a sample of mass 15.31 mg was used. The sample had to be cut for field parallel to c and the sample weight was 12.058 mg. For all measurements a constant magnetic field $H = 3$ T was used while the temperature was varied between 300 and 1000 K. To achieve these temperatures an oven setup provided as an option by Quantum Design was utilized. The crystal was fixed on a zirconia sample stick containing a wire system that acts as a heating element. The sample was glued on the stick with heat-resistant cement and wrapped in low-emissivity copper foil to minimize the heat leak from the hot region to the surrounding coil set. The measurements took place with heating rates of between 1 and 2 K per minute. The magnetic moment of the empty sample holder, 7.63 mg of cement and of the copper foil was measured separately and subtracted from the data.

The NMR measurements were carried out on a polycrystalline sample using the conventional pulsed NMR technique on ^{75}As nuclei (nuclear spin $I = 3/2$ and gyromagnetic ratio $^{75}\gamma/2\pi = 7.2919$ MHz/T) in the temperature range $4 \leqslant T \leqslant 300$ K. The measurements were done at a radio frequency of about 52 MHz. Spectra were obtained by sweeping the field at fixed frequency. The ^{75}As nuclear spin-lattice relaxation rate $1/T_1$ was measured by the conventional single saturation pulse method.

III. THE J_1-J_2-J_c HEISENBERG MODEL

A bipartite spin lattice is defined as consisting of two distinct spin sublattices in which a given spin on one sublattice only interacts with nearest-neighbor (NN) spins on the other sublattice. In the FeAs-based superconductors and parent compounds, when the magnetism is analyzed in a local
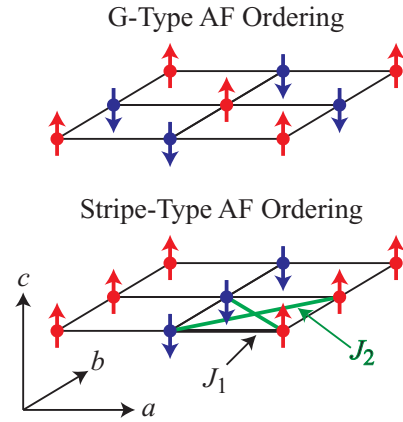

FIG. 2. (Color online) Collinear commensurate in-plane magnetic structures in the J_1-J_2-J_c model for the square lattice antiferromagnet. The top panel shows the G-type (Néel or checkerboard) AF structure where nearest-neighbor spins are aligned antiparallel. The bottom panel shows stripe-type ordering, along with the definitions of the in-plane exchange constants J_1 and J_2. A J_2 interaction is present for both diagonals of each square. According to Eqs. (4), the G-type in-plane ordering is favored if $J_2 < J_1/2$, whereas the stripe-type ordering is favored if $J_2 > J_1/2$. By examining the bottom panel, one sees that the stripe magnetic structure consists of two interpenetrating G-type magnetic structures, each respectively consisting of next-nearest-neighbor spins.

moment model, the magnetic lattice is found not to be bipartite.[4] In addition to the in-plane (J_1) and out-of-plane (J_c) NN intersublattice interactions, in-plane diagonal next-nearest-neighbor (NNN) intrasublattice interactions J_2 are also present along both diagonals of each square, as shown in Fig. 2. The spin Hamiltonian in the J_1-J_2-J_c Heisenberg model is

$$\mathcal{H} = J_1 \sum_{NN} \mathbf{S}_i \cdot \mathbf{S}_j + J_2 \sum_{NNN} \mathbf{S}_i \cdot \mathbf{S}_j$$
$$+ J_c \sum_c \mathbf{S}_i \cdot \mathbf{S}_j + g\mu_B H \sum_i S_i^z, \qquad (2)$$

where $\mathbf{S}_i$ is the spin operator for the ith site, g is the spectroscopic splitting factor (g factor) of the magnetic moments, μ_B is the Bohr magneton, and H is the magnitude of the magnetic field which is applied in the $+z$ direction. Throughout this paper, a positive J corresponds to an antiferromagnetic interaction and a negative J to a ferromagnetic interaction. The indices NN and NNN indicate sums restricted to distinct spin pairs in a Mn layer, while the index c indicates a sum over distinct NN Mn spin pairs along the c axis. This is the minimal model needed to explain our INS results below for $BaMn_2As_2$.

The classical energies of collinear commensurate ordered spin configurations in this model with $H = 0$ are analyzed as discussed in Ref. 4. We consider four competing magnetic structures in the J_1-J_2-J_c model. One is the simple FM structure. The other three are two AF stripe structures and the G-type (Néel) structure shown in Fig. 2. By definition, the NN spins in alternate layers are aligned antiferromagnetically in the G-type AF ordered state, whereas the stripe state can have either AF or FM spin alignments along the c axis which

depend on the sign of J_c. The classical energies of these states for $H = 0$ are[4]

$$E_{\text{FM}} = NS^2(2J_1 + J_c + 2J_2),$$
$$E_{\text{stripe}} = NS^2(-2J_2 \pm J_c), \qquad (3)$$
$$E_{\text{G}} = NS^2(-2J_1 - J_c + 2J_2),$$

where N is the number of spins S and a factor of $1/2$ has been inserted on the right-hand sides to avoid double-counting distinct pairs of spins. The $\pm$ signs in the expression for the stripe phase arise due to the possibilities of either antiferromagnetic ($-$sign) or ferromagnetic ($+$sign) alignment of adjacent spins along the c axis. From these expressions, the in-plane G-type AF magnetic structure observed in BaMn$_2$As$_2$ is lower in energy than the stripe structure if

$$J_1 > 0, \qquad J_1 > 2J_2 \quad \text{(G-type AF)}. \qquad (4)$$

In order that G-type AF ordering occurs along the c axis, one also requires that

$$J_c > 0 \quad \text{(G-type AF)}. \qquad (5)$$

These results place restrictions on the exchange coupling parameter space that is relevant to the G-type AF ordering observed in BaMn$_2$As$_2$. Equations (4) and (5) require both J_1 and J_c to be positive (antiferromagnetic), but J_2 can have either sign as long as it satisfies the second of Eqs. (4). The compound BaFe$_2$As$_2$, on the other hand, has an in-plane stripe-AF state at low temperatures (and with the ordered moment in the ab plane instead of along the c axis as in Fig. 1 for BaMn$_2$As$_2$),[4] which in a local moment model requires $J_1 < 2J_2$ according to Eqs. (3). The in-plane stripe phase can be considered to consist of two interpenetrating G-type AF sublattices, where in this case a sublattice consists of all NNN spins of a given spin and which are connected by an antiferromagnetic interaction J_2 (see the bottom panel of Fig. 2).

IV. INELASTIC NEUTRON SCATTERING (INS) MEASUREMENTS AND ANALYSIS

Figures 3(a) and 3(b) show images of the INS data taken at the base temperature of 8 K which share similar features at each incident energy. Unpolarized inelastic neutron scattering contains contributions from both magnetic and phonon scattering. The magnetic scattering intensity falls off with Q (or scattering angle 2θ) due to the magnetic form factor, while phonon scattering intensity increases like Q^2. One can then observe a large contribution from magnetic scattering between 60 and 80 meV, presumably due to spin wave excitations in the magnetically ordered phase, whose intensity only appears at small Q. On this intensity scale, strong phonon scattering is apparent below approximately 40 meV.

This separation of magnetic and phonon scattering is more clearly shown by plots of the Q dependence of the scattering averaged over different energy ranges, as shown in Fig. 4. For an energy range from 30 to 40 meV, the scattering is dominated by a large phonon contribution, whose intensity is proportional to Q^2, and a large constant background due to multiple scattering and other background contributions. Q-dependent oscillations arise from the powder averaging of
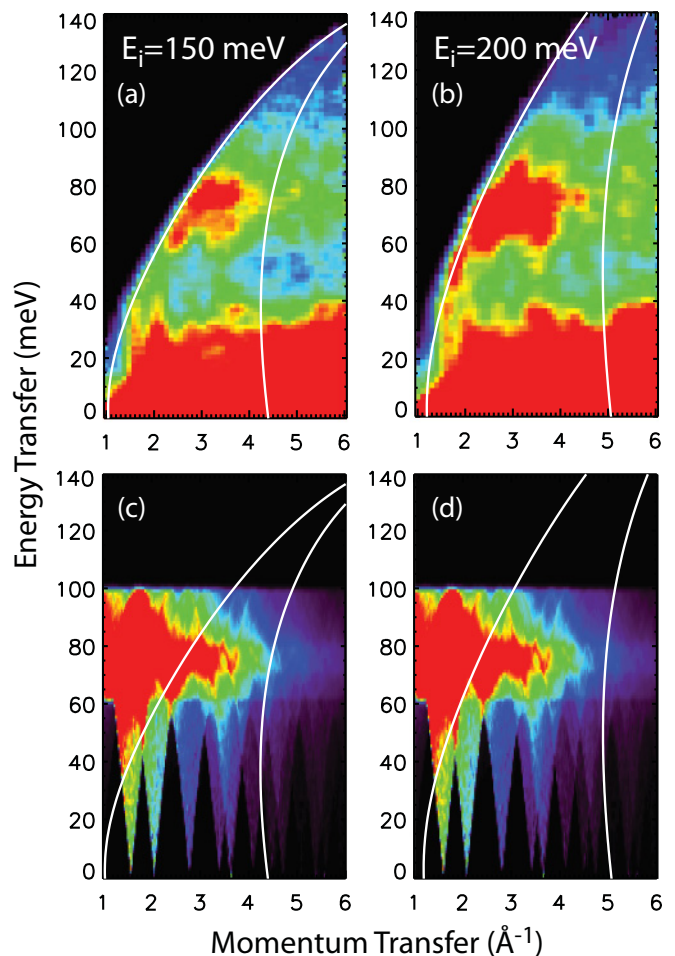

FIG. 3. (Color online) Inelastic neutron scattering data from a powder sample of BaMn$_2$As$_2$ as measured on the Pharos spectrometer with incident energies (a) $E_{\text{i}} = 150$ meV and (b) $E_{\text{i}} = 200$ meV. The white lines delineate scattering angles of $7°$ and $30°$ where the magnetic scattering was estimated. Panels (c) and (d) show calculations of the polycrystalline averaged spin wave scattering using a Heisenberg model. The calculations in (c) and (d) are identical; however, panel (c) shows the trajectories of the angle summation limits for $E_{\text{i}} = 150$ meV and (d) for $E_{\text{i}} = 200$ meV.

the coherent phonon scattering and weak magnetic scattering. At the higher energy ranges between 60 and 90 meV, the Q^2 phonon contributions are gone and magnetic scattering appears superimposed on a constant background. The magnetic scattering intensity falls off with Q as the magnetic form factor for the Mn^{2+} ion and is no longer visible above $\sim$6 Å^{-1}. Similar to the phonon cross section, Q-dependent oscillations in the magnetic scattering occur due to coherent scattering of spin waves.

The spin wave spectrum can be obtained by averaging the low-Q (low 2θ) data to improve statistics. However, the magnetic scattering, especially below $\sim$50 meV, must be separated from the phonon scattering and other background contributions. The pure phonon signal can be estimated from the high-angle spectra, where magnetic scattering is absent. The magnetic scattering component can then be estimated by subtracting the high-angle data (averaged from $2\theta = 50°$–$90°$) from low-angle data (averaged from $2\theta = 7°$–$30°$ and
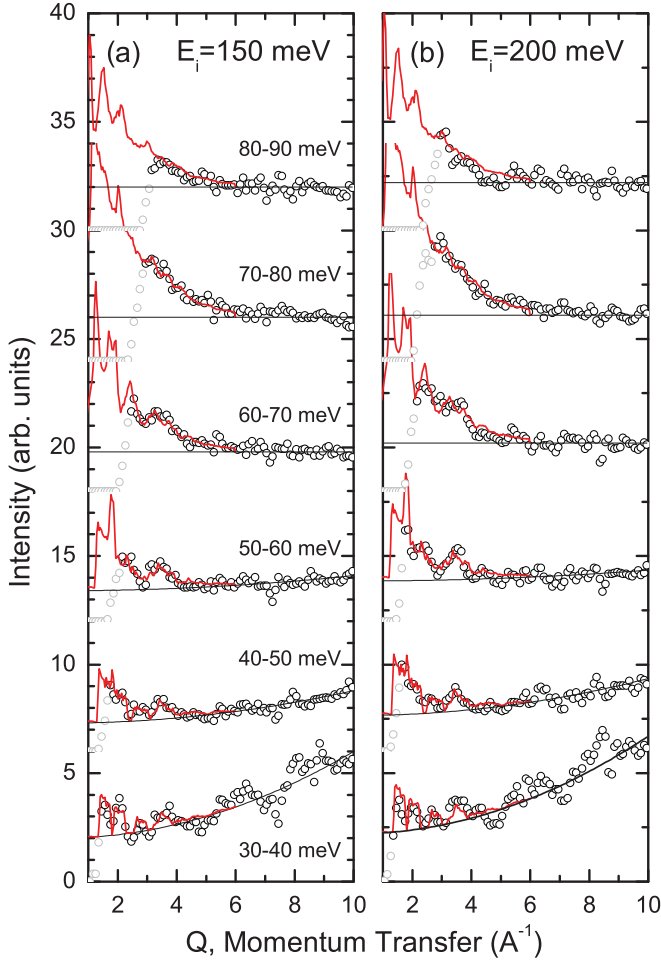
FIG. 4. (Color online) Q dependence of the inelastic neutron scattering intensity averaged over several energy ranges with incident energies (a) $E_i = 150$ meV and (b) $E_i = 200$ meV. The red lines show calculations of the polycrystalline averaged spin wave scattering using the J_1-J_2-J_c Heisenberg model.

indicated by the white lines in Fig. 3) after scaling by a constant factor. These spectra are shown in Fig. 5 and show a strong and broad magnetic peak at ~70 meV. At energies below 50 meV, the subtraction of the phonon intensity is subject to error since the phonon intensity may not scale uniformly to low Q due to coherent scattering effects and also due to the different Debye-Waller factors for each atomic species. It is difficult to quantify this error without detailed phonon models; however, most of the magnetic scattering occurs above the phonon cutoff. Thus, the errors introduced are only a problem below 50 meV and the isolated magnetic data in this energy range can contain large errors.

A. Spin waves in the J_1-J_2-J_c Heisenbeerg model for a G-type antiferromagnet

1. Spin wave theory

In order to analyze the Q and ω dependence of the magnetic spectra, we utilize a model of the spin wave scattering in BaMn$_2$As$_2$. Spin waves in insulators such as BaMn$_2$As$_2$ with the ThCr$_2$As$_2$ structure can be described by the Heisenberg
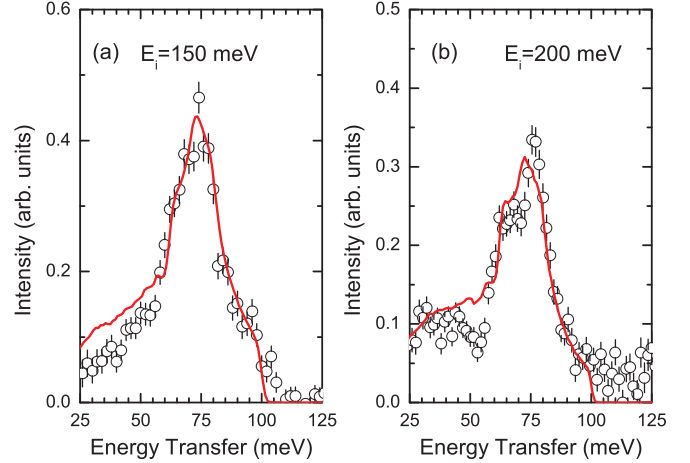

FIG. 5. (Color online) Energy dependence of the inelastic neutron scattering intensity averaged over a scattering angle range from 7° to 30° with incident energies (a) $E_i = 150$ meV and (b) $E_i = 200$ meV. The magnetic intensity was extracted from the total scattering as described in the text. The red lines show calculations of the polycrystalline averaged spin wave scattering using the J_1-J_2-J_c Heisenberg model.

Hamiltonian (2) except that here we set the magnetic field H in the last term to zero.

The spin wave dispersions for the G-type AF structure are obtained from a Holstein-Primakoff spin wave expansion of the Heisenberg model. When the single-ion anisotropy is zero, the dispersions with respect to the body-centered-tetragonal (bct) $I4/mmm$ unit cell containing two formula units of BaMn$_2$As$_2$ are

$$\left[\frac{\hbar\omega(\mathbf{q})}{2SJ_1}\right]^2 = \left\{2 + \frac{J_c}{J_1} - \frac{J_2}{J_1}[2 - \cos(q_x a) - \cos(q_y a)]\right\}^2$$
$$- \left\{\cos\left[(q_x + q_y)\frac{a}{2}\right] + \cos\left[(q_x - q_y)\frac{a}{2}\right]\right.$$
$$\left. + \frac{J_c}{J_1}\cos\left(\frac{q_z c}{2}\right)\right\}^2, \tag{6}$$

where $a = 4.15$ and $c = 13.41$ Å are the lattice parameters of the bct unit cell at our measurement temperature of 8 K.[13]

In the absence of an anisotropy-induced energy gap in the spin wave spectrum, the long-wavelength spin wave energies are described for an orthogonal (cubic, tetragonal, or orthorhombic) antiferromagnetically ordered spin lattice by the generic dispersion relation

$$E_{\mathbf{q}} = \hbar\omega(\mathbf{q}) = \hbar\sqrt{v_a^2 q_x^2 + v_b^2 q_y^2 + v_c^2 q_z^2}, \tag{7}$$

where v_a, v_b, and v_c are the spin wave velocities (speeds) along the respective axes. In our case of tetragonal symmetry we have

$$E_{\mathbf{q}} = \hbar\omega(\mathbf{q}) = \hbar\sqrt{v_{ab}^2\left(q_x^2 + q_y^2\right) + v_c^2 q_z^2}, \tag{8}$$

where $v_{ab} \equiv v_a = v_b$. For G-type AF ordering of a spin lattice with our bct unit cell, these velocities are derived from the

dispersion relation in Eq. (6) as

$$\hbar v_{ab} = 2J_1 Sa \sqrt{\left(1 - \frac{2J_2}{J_1}\right)\left(1 + \frac{J_c}{2J_1}\right)},$$

$$\hbar v_c = \sqrt{2}J_1 Sc \sqrt{\frac{J_c}{J_1}\left(1 + \frac{J_c}{2J_1}\right)}. \tag{9}$$

From the first of Eqs. (9) the in-plane spin wave velocity v_{ab} decreases with increasing J_2, consistent with expectation since, according to Fig. 2, a positive (AF) J_2 is a frustrating interaction for G-type AF ordering. Indeed, v_{ab} vanishes when $J_2 = J_1/2$, which is the classical criterion in Eq. (4) for the transition between the G-type and stripe-type in-plane AF ordering arrangements.

In order to make contact with previous spin wave calculations for isotropic and anisotropic primitive orthogonal spin lattices, one can change unit cell variables to those of the primitive tetragonal (pt) spin lattice containing one spin at each lattice point with lattice parameters a' and c'. Referring to the bct structure with lattice parameters a and c in Fig. 1, the pt spin-lattice parameters are related to these according to

$$a = \sqrt{2}\,a', \quad c = 2\,c'. \tag{10}$$

Furthermore, the pt unit cell is rotated about the c axis by 45° with respect to the bct unit cell, so the pt wave vectors q'_x, q'_y, and q'_z are related to those with respect to the bct cell q_x, q_y, and q_z by

$$q_x + q_y = \sqrt{2}\,q'_x, \quad -q_x + q_y = \sqrt{2}\,q'_y, \quad q_z = q'_z. \tag{11}$$

With these conversion expressions, the dispersion relation in Eq. (6) becomes

$$\left[\frac{\hbar\omega(\mathbf{q'})}{2SJ_1}\right]^2 = \left\{2 + \frac{J_c}{J_1} - \frac{2J_2}{J_1}[1 - \cos(q'_x a')\cos(q'_y a')]\right\}^2$$
$$- \left[\cos(q'_x a') + \cos(q'_y a') + \frac{J_c}{J_1}\cos(q'_z c')\right]^2. \tag{12}$$

Our dispersion relation (12) is identical to that in Refs. 21 and 22 derived from linear spin wave theory for the J_1-J_2-J_c model. Also, Eq. (12) with J_2 set to zero is identical to that in Eq. (5) of Ref. 26 and in Eq. (3) of Ref. 27 for the anistropic simple cubic G-type bipartite antiferromagnet.

Using Eqs. (10), for the primitive tetragonal spin lattice the spin wave velocities in Eqs. (9) become

$$\hbar v_{a'b'} = 2\sqrt{2}J_1 Sa' \sqrt{\left(1 - \frac{2J_2}{J_1}\right)\left(1 + \frac{J_c}{2J_1}\right)},$$

$$\hbar v_{c'} = 2\sqrt{2}J_1 Sc' \sqrt{\frac{J_c}{J_1}\left(1 + \frac{J_c}{2J_1}\right)}. \tag{13}$$

In a simple cubic bipartite spin lattice with one spin per lattice point and isotropic interactions with $c' = a'$, $J_c/J_1 = 1$, and $J_2 = 0$, the spin wave velocity is isotropic with magnitude $\hbar v' = 2\sqrt{3}J_1 Sa'$, which is the same as given previously in Table I of Ref. 26, where a' was set to unity and is the standard well-known result when magnetocrystalline anisotropy is negligible.[28]
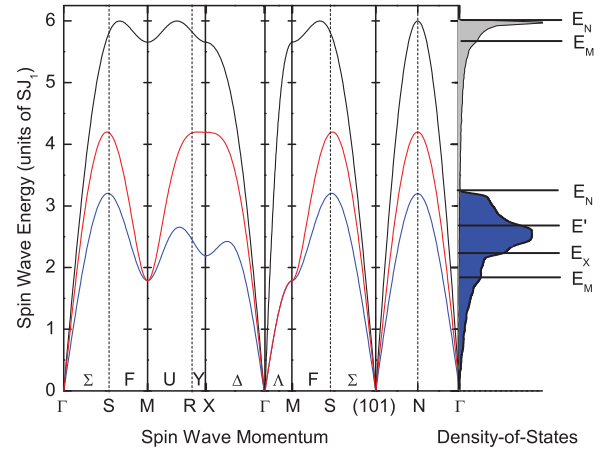

FIG. 6. (Color online) The spin wave dispersion of the J_1-J_2-J_c model along various symmetry directions for three different combinations of the exchange parameters: $J_2/J_1 = 0$ and $J_c/J_1 = 1$ (top black curve); $J_2/J_1 = 0$ and $J_c/J_1 = 0.1$ (middle red curve); and $J_2/J_1 = 0.25$ and $J_c/J_1 = 0.1$ (bottom blue curve). Energies are reported in units of SJ_1. The Γ point in the Brillouin zone corresponds to wave vector $\mathbf{q} = 0$. The $\mathbf{q}$ values corresponding to the high-symmetry M, X, and N points are given in Table I. These wave-vector directions are written with respect to the lattice translation vectors of the $I4/mmm$ chemical unit cell. The labels Σ, F, U, Y, Δ, and Λ correspond to high-symmetry lines in reciprocal space. In the far right-hand panel, the energy versus the spin wave density of states is shown for $J_2/J_1 = 0$ and $J_c/J_1 = 1$ (top gray region) and $J_2/J_1 = 0.25$ and $J_c/J_1 = 0.1$ (bottom blue region).

2. Application of spin wave theory to BaMn$_2$As$_2$

Spin wave dispersions using the bct notation in Eq. (6) are plotted in Fig. 6 (in units of SJ_1) for three different combinations of the exchange ratios J_2/J_1 and J_c/J_1. The notations in Fig. 6 and Table I for labeling the zone boundary reciprocal space positions are given by Kovalev.[29] The magnetic excitation wave-vector $\mathbf{q}$ values are in reciprocal lattice units given by (H, K, L) r.l.u. This is a shorthand for $\mathbf{q}$ expressed in inverse length units of the bct chemical unit cell according to

$$\mathbf{q} = \frac{2\pi H}{a}\,\hat{\mathbf{a}} + \frac{2\pi K}{a}\,\hat{\mathbf{b}} + \frac{2\pi L}{c}\,\hat{\mathbf{c}}.$$

TABLE I. Energies of various van Hove singularities in the spin wave density of states of G-type antiferromagnets with NN (J_1), NNN (J_2), and interlayer (J_c) exchange interactions.

$\mathbf{q}$	Label	van Hove singularity energy
(001)	E_M	$4SJ_1\sqrt{2\frac{J_c}{J_1}}$
$\left(\frac{1}{2}, \frac{1}{2}, 0\right)$	E_X	$2SJ_1\sqrt{\left(2 + \frac{J_c}{J_1} - 4\frac{J_2}{J_1}\right)^2 - \left(\frac{J_c}{J_1}\right)^2}$
$\left(\frac{1}{2}, 0, \frac{1}{2}\right)$	E_N	$2SJ_1\left(2 + \frac{J_c}{J_1} - 2\frac{J_2}{J_1}\right)$
$\left(\frac{1}{2}, \frac{1}{2}\,\frac{1}{2}\right)$	E_P	$2SJ_1\left(2 + \frac{J_c}{J_1} - 4\frac{J_2}{J_1}\right)$
$\left(\frac{3}{4}, \frac{1}{4}, 0\right)$	E'	$2SJ_1\sqrt{\left(2 + \frac{J_c}{J_1} - 2\frac{J_2}{J_1}\right)^2 - \left(1 - \frac{J_c}{J_1}\right)^2}$

In the $I4/mmm$ bct unit cell notation, the magnetic propagation vector for G-type AF ordering is $\tau_G = (1,0,1)$, which gives $\tau_G = (0,0,0)$ when translated by a reciprocal lattice vector to the Γ point in the Brillouin zone. This corresponds to the more familiar G-type wave vector $\tau'_G = (\frac{1}{2}, \frac{1}{2}, \frac{1}{2})$ in the pt cell according to the transformation $\mathbf{q'} = (\frac{H+K}{2}, \frac{H-K}{2}, \frac{L}{2})$, where H, K, L are referred to the $I4/mmm$ crystallographic unit cell, as shown in Eqs. (11).

For $J_2 = 0$ and $J_c/J_1 = 1$ (the top black curve in Fig. 6), the dispersion is that of an isotropic G-type antiferromagnet (similar to LaFeO$_3$[27]) with a maximum spin wave energy of $6SJ_1$. For the layered BaMn$_2$As$_2$ structure, J_c is expected to be much weaker than J_1. When $J_2 = 0$ and $J_c/J_1 = 0.1$ (the middle red curve in Fig. 6), the maximum spin wave energy is reduced to $\sim 4SJ_1$ and the zone boundary M-point spin wave at $\mathbf{q} = (001)$ is strongly reduced. If we now turn on antiferromagnetic NNN interactions with $J_2/J_1 = 0.25$ (the bottom blue curve in Fig. 6), we observe a further softening of the spin wave spectrum, most notably at the X point. When $J_2 > J_1/2$, the G-type ordering becomes unstable and the stripe-AF order is the new ground state with ordering wave vector at the X point as discussed above in Sec. III, and our spin wave expressions are no longer applicable. The spin wave theory for the stripe phase in the Fe-based superconductor parent compounds with the ThCr$_2$As$_2$ structure is reviewed in Ref. 4.

The powder-averaged spin wave scattering is closely associated with the spin wave density of states [SWDOS, $g(\omega)$]. The SWDOS is the distribution of spin wave energies and is determined by the summation over all wave vectors in the Brillouin zone ($\mathbf{q}$),

$$g(\omega) = \sum_{\mathbf{q}} \delta\left[\hbar\omega - \hbar\omega(\mathbf{q})\right]. \tag{14}$$

The SWDOSs versus energy $\hbar\omega$ are shown on the right-hand side of Fig. 6. It is observed that the SWDOS remains sharply peaked when $J_2 = 0$ and that J_2 acts to broaden the SWDOS. Table I indicates the energies of the various extremal features in the SWDOS (van Hove singularities) for ratios J_2/J_1 and J_c/J_1 that are associated with zone boundary spin wave energies.

B. Calculations of the scattered intensity

When performing an INS experiment on a powder, the resulting INS intensities arise from the averaging of the inelastic scattering structure factor $S(\mathbf{Q},\omega)$ over all orientations of the crystallites. Despite the orientational averaging, the spectra can show evidence of the spin wave dispersions, especially at low angles (within the first Brillouin zone) and in the vicinity of the first few magnetic Bragg peaks. Due to the weighting of the spin wave modes by coherent scattering intensities, the Q-averaged intensity, $S(\omega)$, as shown in Fig. 5 does not necessarily give the SWDOS. This is only true in the incoherent scattering approximation, which does not apply to the case of scattering from a magnetically ordered system. Therefore, model calculations of the powder-averaged spin wave intensities are necessary for accurate comparison to the data.

Numerical calculations of the spin waves in the Heisenberg model give not only the dispersion relation $\omega_n(\mathbf{q})$ for the nth (degenerate) branch [as shown in Eq. (6)], but also the spin wave eigenvectors, $T_{ni}(\mathbf{q})$, for the ith spin in the magnetic unit

TABLE II. Parameters of the Heisenberg model in Eq. (2) for BaMn$_2$As$_2$ determined from magnetic inelastic neutron scattering measurements at a temperature of 8 K. The Mn positions i in the top two rows refer to the crystallographic $I4/mmm$ unit cell with lattice parameters $a = 4.15$ and $c = 13.41$ Å at 8 K. The moment direction is along the c axis. The spin S of the Mn atoms is not independently determined from the measurements. Only the products of S with the exchange constants J_i can be modeled. All exchange parameters are positive (antiferromagnetic). Also shown are the low-energy spin wave velocities in the ab plane v_{ab} and along the c axis v_c, each multiplied by $\hbar$, calculated from the exchange constants using Eqs. (9).

i	σ_i	d_i
1	$+1$	$(0,0,0)$
2	-1	$(\frac{1}{2}, \frac{1}{2}, 0)$

Exchange constant	Value	Value (K)
SJ_1	(33 ± 3) meV	380
J_1 ($S = 2, 5/2$)	16.5, 13.2 meV	190, 150
SJ_2	(9.5 ± 1.3) meV	110
J_2 ($S = 2, 5/2$)	4.8, 3.8 meV	55, 44
SJ_c	(3.0 ± 0.6) meV	35
J_c ($S = 2, 5/2$)	1.5, 1.2 meV	18, 14
$S(2J_1 + J_c)$	69 meV	800
$2J_1 + J_c$ ($S = 2, 5/2$)	18.0, 14.4 meV	400, 320
J_2/J_1	0.29 ± 0.05	
J_c/J_1	0.09 ± 0.02	

Spin wave velocity	Value (meV Å)
$\hbar v_{ab}$	180
$\hbar v_c$	190

cell. The dispersion and associated eigenvectors can be used to calculate the spin wave structure factor for unpolarized neutron energy loss scattering from a single-crystal sample, $S_{\text{mag}}(\mathbf{Q},\omega)$, given by

$$
\begin{aligned}
S_{\text{mag}}(\mathbf{Q},\omega) = {} & \frac{1}{2}(\gamma r_o)^2 \left[1 + \frac{(\hat{\mu} \cdot \mathbf{Q})^2}{Q^2}\right] \\
& \times \sum_n \left| \sum_i F_i(\mathbf{Q}) \sigma_i \sqrt{S_i} T_{ni}(\mathbf{q}) e^{-i\mathbf{Q} \cdot \mathbf{d}_i} \right|^2 \\
& \times [n(\omega) + 1] \delta[\omega - \omega_n(\mathbf{q})],
\end{aligned} \tag{15}
$$

where the ith spin with magnitude S_i pointed in direction $\hat{\mu}$ is located at position $\mathbf{d}_i$ and $\sigma_i = \pm 1$ is the direction of the spin relative to the quantization axis $\hat{\mu}$ for a collinear spin structure, as shown in the top two rows of Table II. The vector $\mathbf{q} = \mathbf{Q} - \vec{\tau}$ is the spin wave wave vector in the first Brillouin zone. Finally, the function $n(\omega)$ is the temperature-dependent Bose factor and $F_i(\mathbf{Q}) = \frac{1}{2} g_i f_i(\mathbf{Q}) e^{-W_i(\mathbf{Q})}$ is a product of the spectroscopic splitting factor (g factor), magnetic form factor, and Debye-Waller factor for the ith spin, respectively. The constant $(\gamma r_o)^2 = 290.6$ mb allows calculations of the cross section to be reported in absolute units of [mb sr^{-1} meV^{-1} (formula

unit)$^{-1}$]. For BaMn$_2$As$_2$, all Mn ions in the magnetic cell are equivalent. The structure factor can then be written

$$S_{\text{mag}}(\mathbf{Q},\omega) = \frac{1}{2}(\gamma r_o)^2 SF^2(\mathbf{Q})\left[1 + \frac{(\hat{\mu}\cdot\mathbf{Q})^2}{Q^2}\right]$$

$$\times \sum_n \left|\sum_i \sigma_i T_{ni}(\mathbf{q})e^{-i\mathbf{Q}\cdot\mathbf{d}_i}\right|^2$$

$$\times [n(\omega) + 1]\,\delta[\omega - \omega_n(\mathbf{q})]. \qquad (16)$$

In the calculations, we use the isotropic magnetic form factor for Mn found in the International Crystallography Tables[30] and the Debye-Waller factor is set equal to unity. The differential magnetic cross section that is measured in the inelastic neutron scattering experiments is proportional to the structure factor.

To compare Heisenberg model spin wave results to the powder INS data, powder-averaging of $S_{\text{mag}}(\mathbf{Q},\omega)$ is performed by Monte Carlo integration over 25 000 $\mathbf{Q}$ vectors lying on a constant-Q sphere, giving the orientationally averaged $S_{\text{mag}}(Q,\omega)$ which depends only on the magnitude of Q. By a comparison of the total $S(Q,\omega)$ in Fig. 3, the Q cuts in Fig. 4, and the energy spectra in Fig. 5, we arrive at the following parameters: $SJ_1 = 33$ meV, $SJ_2 = 9.5$ meV ($J_2/J_1 = 0.29$), and $SJ_c = 3$ meV ($J_c/J_1 = 0.09$), as summarized in Table II. Figures 3(c) and 3(d) show that calculations of $S_{\text{mag}}(Q,\omega)$ at 8 K using these parameters compare well to the corresponding data in Figs. 3(a) and 3(b) and show clearly the coherent scattering of the powder-averaged spin waves. The most obvious coherent scattering feature is the necking down of acoustic spin waves in the vicinity of allowed magnetic Bragg reflections. The first two observed magnetic Bragg peaks are at $\mathbf{Q} = (101)$ and (103). Additional coherent scattering features can also be seen for zone boundary spin waves, where intensities tend to peak in between the allowed magnetic Bragg peaks. Figure 3 enforces the general agreement of the Heisenberg model calculations of the spin wave intensity with neutron scattering measurements.

More quantitative estimates of the agreement of the calculated spin waves and the data are shown in Figs. 4 and 5. The calculations can be summed over scattering angles in order to compare the equivalent angle-summed data, as shown in Fig. 5. The success of the Heisenberg model in estimating the measured spin wave intensities is better observed by plotting constant energy Q cuts, as shown in Fig. 4. The plots show Q oscillations of the experimental magnetic spin wave scattering above a background due mainly to phonon scattering and background/multiple scattering. A constant background and incoherent phonon scattering intensity (proportional to Q^2) are added to the calculated spin wave scattering in order to compare to the measured data. The agreement confirms the adequacy of the parameters.

The low-energy spin wave velocities in the ab plane v_{ab} and along the c axis v_c calculated from the exchange constants in Table II using Eqs. (9) are shown in Table II for our measurement temperature of 8 K. Remarkably, in spite of the layered nature of the spin lattice, the ab-plane and c-axis spin wave velocities are seen to have nearly the same value $\hbar v_{ab} \approx \hbar v_c \approx 180\text{--}190$ meV Å. For comparison, the spin wave velocities in the AFe$_2$As$_2$ compounds are in the ranges $\hbar v_{ab} \approx 280\text{--}570$ meV Å and $\hbar v_c \approx 57\text{--}280$ meV Å.[4]
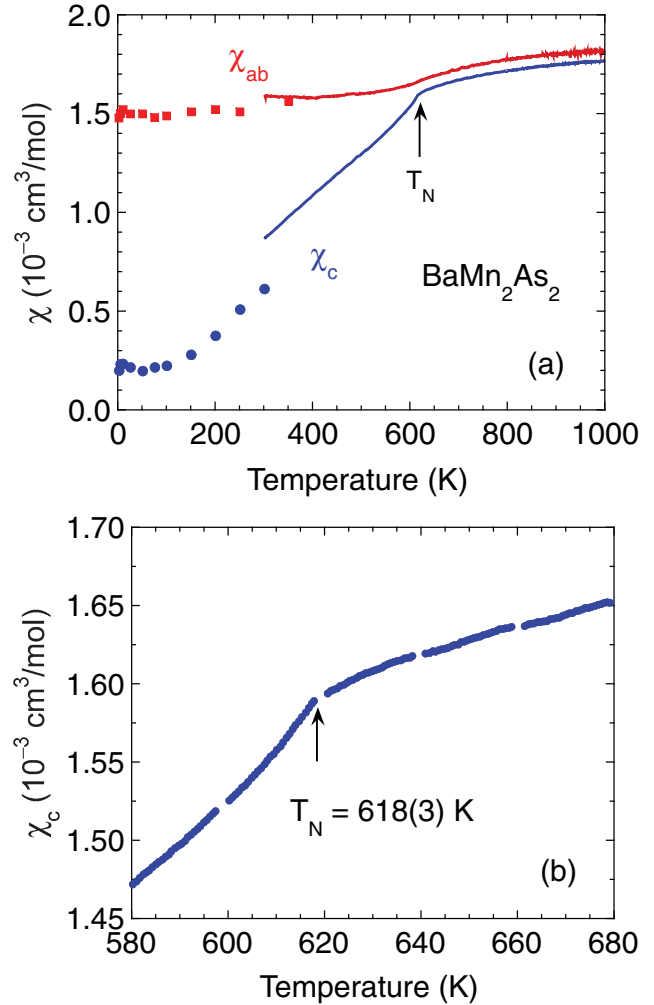

FIG. 7. (Color online) (a) Magnetic susceptibility χ versus temperature T of single crystals of BaMn$_2$As$_2$ with the applied magnetic field parallel to the c axis (χ_c) and to the ab plane (χ_{ab}). The individual symbols are the data previously reported in Ref. 11. The solid curves are the present data obtained in an applied magnetic field $H = 3$ T. The Néel temperature T_N is indicated. (b) Expanded plot of $\chi_c(T)$ for temperatures around T_N. The temperature of the maximum slope of $\chi_c(T)$ gives $T_N = 618(3)$ K.

V. MAGNETIC SUSCEPTIBILITY MEASUREMENTS

The anisotropic magnetic susceptibilites $\chi(T)$ of a single crystal of BaMn$_2$As$_2$ in an applied magnetic field $H = 3$ T are shown in Fig. 7(a) for temperatures of 300 to 1000 K, together with our previous data[11] below 350 K. Our $\chi_{ab}(T)$ data are consistent with the previous $\chi_{ab}(T)$ data over the temperature range of overlap (300–400 K),[11] but there is a difference between the c-axis data sets over that overlap temperature range for reasons that are not clear to us. The temperature of the maximum slope of $\chi_c(T)$ from Fig. 7(b) gives the Néel temperature as $T_N = 618(3)$ K, nearly the same as the value of 625(1) K determined from the previous magnetic neutron diffraction measurements on a powder sample.[13] Above T_N, the susceptibility is nearly isotropic and exhibits negative curvature. The susceptibility appears to reach a maximum at a temperature $T^{\text{max}} \approx 1000$ K, where the value of the

TABLE III. Parameters describing the magnetic behaviors of BaMn$_2$As$_2$. Here T_N is the Néel temperature, χ_{ab} is the magnetic susceptibility with the magnetic field aligned in the ab plane, χ_c is the magnetic susceptibility with the magnetic field aligned along the c axis, and $\chi_{ave} = (2\chi_{ab} + \chi_c)/3$ is the powder-averaged value of the susceptibility. Our $\chi(T)$ results and those of Ref. 11 are on single crystals. The T_N value listed for Ref. 13 was obtained from magnetic neutron diffraction measurements on a powder sample.

Property	Value	Reference
χ_{ab} (10 K)	$1.50(2) \times 10^{-3}$ cm^3/mol	11
χ_c (10 K)	$0.20(2) \times 10^{-3}$ cm^3/mol	11
T_N	625(1) K	13
T_N	618(3) K	This work
χ_{orb}	$0.20(2) \times 10^{-3}$ cm^3/mol	This work
χ_{ab} (T_N)	1.66×10^{-3} cm^3/mol	This work
χ_c (T_N)	1.60×10^{-3} cm^3/mol	This work
χ_{ave} (T_N)	1.64×10^{-3} cm^3/mol	This work
χ_{spin} (T_N)	1.44×10^{-3} cm^3/mol	This work
χ_{ab} (1000 K)	1.81×10^{-3} cm^3/mol	This work
χ_c (1000 K)	1.76×10^{-3} cm^3/mol	This work
χ_{ave} (1000 K)	1.79×10^{-3} cm^3/mol	This work
χ_{spin} (1000 K)	1.59×10^{-3} cm^3/mol	This work

average susceptibility is $\chi_{ave}^{max} = 1.79 \times 10^{-3}$ cm^3/mol and a "mol" refers to a mole of formula units (f.u.) unless otherwise stated. The values of the anisotropic susceptibilities at several distinctive temperatures are summarized in Table III.

One can partition the measured susceptibility $\chi(T)$ of a material into spin χ_{spin} and orbital χ_{orb} parts. Generally, the orbital part is independent of T but χ_{spin} does depend on T, so one obtains

$$\chi(T) = \chi_{orb} + \chi_{spin}(T). \tag{17}$$

The χ_{orb} generally consists of paramagnetic Van Vleck and diamagnetic core contributions, plus the Landau diamagnetism of conduction electrons which is not significant in semiconducting BaMn$_2$As$_2$. From Fig. 7(a), the measured $\chi(T > T_N)$ is (nearly) isotropic. Therefore, we infer that χ_{orb} is isotropic at all T. For a collinear antiferromagnetic insulator (semiconductor) such as BaMn$_2$As$_2$, one expects the spin susceptibility parallel to the ordered moment direction, $\chi_{c\ spin}$ in our case, to be zero at $T \to 0$. From Fig. 7(a) we then obtain

$$\chi_{orb} \approx 0.20(2) \times 10^{-3} \text{ cm}^3/\text{mol}, \tag{18}$$

which we have included in Table III. Thus, the spin susceptibility is given by

$$\chi_{spin}(T) = \chi(T) - \chi_{orb}. \tag{19}$$

We have listed the values of χ_{spin} at $T = T_N$ and $T = 1000$ K in Table III. It appears from Fig. 7(a) that $\chi(T)$ reaches a maximum at a temperature $T^{max} \approx 1000$ K. Then one obtains from Table III the product

$$\chi_{spin}^{max} T^{max} \approx 0.80 \frac{\text{cm}^3 \text{ K}}{\text{mol Mn}}. \tag{20}$$

Note that this value is for a mole of spins, not a mole of formula units. We use this value later when comparing theory and experiment.

The temperature dependence of $\chi(T)$ above T_N in Fig. 7(a) is opposite to that expected for a fully three-dimensional antiferromagnet, where χ decreases rather than increases above T_N.[31] However, the behavior we observe above T_N is common in low-dimensional antiferromagnets such as the tetragonal cuprate compound Sr$_2$CuO$_2$Cl$_2$, where the intralayer magnetic coupling within the Cu^{+2} spin $S = 1/2$ square lattice is much stronger than the interlayer coupling.[6] Such antiferromagnets exhibit a susceptibility with a broad maximum and the corresponding onset of strong short-range AF ordering at a temperature T^{max} of order the mean-field AF long-range transition temperature [see Eq. (41) below]. However, for the compound Sr$_2$CuO$_2$Cl$_2$ one estimates $T^{max} \sim 1500$ K but it exhibits long-range AF ordering only at a much lower temperature $T_N = 250$ K $\ll T^{max}$. The interlayer coupling J_c is much smaller than the in-plane coupling J_{ab} in quasi-two-dimensional antiferromagnets. The suppression of T_N with respect to T^{max} is due to fluctuation effects associated with the low dimensionality of the system.

In the following we consider what can be learned about the signs and strengths of the exchange interactions in BaMn$_2$As$_2$ from analysis of our experimental data on this compound in terms of molecular field theory. Later in Sec. IX we develop the theory for fitting the experimental data taking into account the intralayer magnetic correlations that are present above T_N, which we then apply to fit the $\chi(T > T_N)$ data in Fig. 7(a) in Sec. X.

VI. MOLECULAR FIELD THEORY

We will be analyzing various experimental data for BaMn$_2$As$_2$ using the Weiss MFT. To introduce the MFT, we first consider the known results for a local magnetic moment model on a bipartite spin lattice with equal numbers of spins **S** in the two spin sublattices i and j interacting with the same NN exchange constant J with the Heisenberg Hamiltonian

$$\mathcal{H} = J \sum_{NN} \mathbf{S}_i \cdot \mathbf{S}_j + g\mu_B H \sum_i S_i^z, \tag{21}$$

where g is the spectroscopic splitting factor (g factor), μ_B is the Bohr magneton, and H is the magnitude of the applied magnetic field, which is in the z direction. For such a quantum local moment system of identical spins interacting by NN interactions, if the susceptibility in the absence of J follows the Curie law $\chi_0 = C/T$, then in MFT the $\chi(T)$ above the magnetic ordering temperature follows the Curie-Weiss law[31]

$$\chi = \frac{C}{T + \theta}, \tag{22}$$

where the Curie constant C is

$$C = \frac{Ng^2\mu_B^2 S(S+1)}{3k_B}, \tag{23}$$

N is the number of spins, and k_B is Boltzmann's constant. Taking N to be Avogadro's number N_A and $g = 2$ gives a useful expression for the Curie constant per mole of spins as

$$C = 0.500\,20\, S(S+1) \frac{\text{cm}^3 \text{ K}}{\text{mol spins}}. \tag{24}$$

The Weiss temperature θ is

$$\theta = \frac{zJS(S+1)}{3k_{\mathrm{B}}}, \qquad (25)$$

where z is the coordination number of each spin. Here, positive θ corresponds to the case when J is positive (AF interactions), whereas a negative θ corresponds to the case when J is negative (FM interactions). If θ is positive, then the magnetic ordering temperature is $T_{\mathrm{N}} = \theta$ for AF ordering. On the other hand, if θ is negative, then FM ordering occurs at the Curie temperature $T_{\mathrm{C}} = |\theta|$.

As discussed in Appendix A, the Curie-Weiss law is not simply a mean-field expression.[6,32–34] It arises from the first $(1/T)$ term in the exact quantum mechanical high-temperature series expansion of the nearest-neighbor two-spin correlation function and is accurate in the limit that higher order $1/T^n$ terms in the two-spin correlation functions are negligible. Thus, the Curie-Weiss law, and hence our scaling expressions in Eqs. (82) and (87) below, begin to fail when $1/T^2$ and higher order terms in the two-spin correlation functions become significant compared to the $1/T$ term with decreasing T.

Another important conclusion from Appendix A is that the Weiss temperature in the Curie-Weiss law results from all the spins that a given spin interacts with, irrespective of the dimensionality of the spin lattice, of whether or not the spin lattice is bipartite (see Sec. VII) or whether all those interactions are the same, but where all spins are equivalent. Thus, if there are different interactions present of a given spin i with other spins j, in Eq. (25) for the Weiss temperature one can make the replacement $zJ \to \sum_{j=1}^{z} J_{ij}$, where z is the total number of spins that spin i has interactions with, giving the Weiss temperature as

$$\theta = \frac{S(S+1)\sum_{j=1}^{z} J_{ij}}{3k_{\mathrm{B}}}. \qquad (26)$$

VII. THE J_1-J_2-J_c HEISENBERG MODEL TREATED IN MOLECULAR FIELD THEORY

The Hamiltonian (2) represents a situation where there is coupling both between the two spin sublattices and within each sublattice, where the two sublattices 1 and 2 correspond to the red (up-pointing) and blue (down-pointing) magnetic moments in the top panel of Fig. 2, respectively. Consider a specific spin i in sublattice 1. This spin i has four in-plane NN in sublattice 2 coupled by J_1 and two out-of-plane NN in sublattice 2 coupled by J_c. Within the same sublattice 1, spin i is coupled to four in-plane NNN by J_2. Since there are multiple exchange constants present from a given spin to its NN and NNN spins, we have

$$\sum_{j=1}^{10} J_{ij} = 2(2J_1 + J_c + 2J_2)$$

and the Weiss temperature (26) becomes

$$\theta = \frac{2(2J_1 + J_c + 2J_2)\,S(S+1)}{3k_{\mathrm{B}}}. \qquad (27)$$

We cannot measure θ for BaMn$_2$As$_2$ because, according to Fig. 7, the temperature range required for the susceptibility

measurments to be in the Curie-Weiss regime would be far above 1000 K.

In MFT, the magnetic induction $\mathbf{B} = B\,\hat{\mathbf{k}}$ seen by each sublattice 1 and 2 is the sum of the applied field $\mathbf{H} = H\,\hat{\mathbf{k}}$ and the respective exchange field $\mathbf{H} = H_{\mathrm{exch}}\,\hat{\mathbf{k}}$; that is,

$$\begin{aligned} B_1 &= H + H_{1\,\mathrm{exch}}, \\ B_2 &= H + H_{2\,\mathrm{exch}}. \end{aligned} \qquad (28)$$

The MFT exchange field H_{exch} seen by each sublattice is, respectively,

$$\begin{aligned} H_{1\,\mathrm{exch}} &= \lambda_{\mathrm{s}} M_1 + \lambda_{\mathrm{d}} M_2, \\ H_{2\,\mathrm{exch}} &= \lambda_{\mathrm{d}} M_1 + \lambda_{\mathrm{s}} M_2, \end{aligned} \qquad (29)$$

where λ_{s} is the net molecular field coupling parameter for coupling within the **same** sublattice and λ_{d} is the net molecular field coupling parameter for coupling between the two **different** sublattices. We obtain in Eq. (35) below expressions for these λ values in terms of the J parameters in Hamiltonian (2).

We only consider here the limit of low applied fields H. In MFT, the magnetization of each sublattice 1 and 2 is given by the response to the applied field plus the exchange field as

$$\begin{aligned} M_1(T,H) &= \frac{\chi_0(T)B_1}{2} = \frac{\chi_0(T)}{2}(H + \lambda_{\mathrm{s}} M_1 + \lambda_{\mathrm{d}} M_2), \\ M_2(T,H) &= \frac{\chi_0(T)B_2}{2} = \frac{\chi_0(T)}{2}(H + \lambda_{\mathrm{s}} M_1 + \lambda_{\mathrm{d}} M_2), \end{aligned} \qquad (30)$$

where $\chi_0(T) \equiv \lim_{H\to 0} M/H$ is the temperature-dependent *spin* susceptibility of the whole system in the absence of the explicit exchange fields, the factors of $1/2$ are there because each sublattice only has half of the total number of spins, and M_i is the z-axis magnetization of the system induced by a magnetic field in the z direction with magnitude H. In the paramagnetic state, $M_2 = M_1$ and Eqs. (30) yield

$$M_i(H,T) = \frac{\chi_0(T)H/2}{1 - (\chi_0/2)(\lambda_{\mathrm{d}} + \lambda_{\mathrm{s}})},$$

where $i = 1,2$. Since $M = 2M_i$, one obtains the spin susceptibility $\chi(T) = 2M_i/H$ as

$$\chi(T) = \frac{\chi_0(T)}{1 - (\chi_0/2)(\lambda_{\mathrm{d}} + \lambda_{\mathrm{s}})}. \qquad (31)$$

The inverse susceptibility is

$$\frac{1}{\chi(T)} = \frac{1}{\chi_0(T)} - \frac{\lambda_{\mathrm{d}} + \lambda_{\mathrm{s}}}{2}. \qquad (32)$$

This is typical of molecular field theory, where the molecular exchange field just shifts the inverse susceptibility up or down by a temperature-independent amount that depends on the sign and magnitude of the net molecular field coupling constant. It is important to note, with respect to fitting experimental data by molecular field theory, that the presence of molecular fields cannot change the temperature of peaks in the susceptibility $\chi_0(T)$ that is assumed in the absence of explicit exchange couplings. For example, one could take $\chi_0(T)$ to be the susceptibility of the isotropic square lattice Heisenberg antiferromagnet such as in Fig. 17 below, which has a broad peak at $T \sim J/k_{\mathrm{B}}$. If one uses a molecular

exchange field to magnetically couple the square lattice layers, this molecular field cannot change the temperature of the broad AF short-range ordering peak.

To determine the magnetic ordering temperature(s) T_m, we set the applied field H to zero in Eqs. (30) and solve for nonzero M_1 and M_2. For the general case one obtains

$$\frac{\chi_0(T_m)}{2}(\lambda_s \pm \lambda_d) = 1, \tag{33}$$

so T_m depends on the assumed $\chi_0(T)$. From Eqs. (29), we see that for G-type AF ordering, we need to have λ_d be negative, so we take the minus sign in Eq. (33) to get

$$\frac{\chi_0(T_N)}{2}(\lambda_s - \lambda_d) = 1, \tag{34}$$

where now T_m is the antiferromagetic ordering (Néel) temperature T_N. Now we can use the solution for a λ in terms of the related J value(s) from Ref. 31 to get

$$\begin{aligned}\lambda_s &= -\left(\frac{2}{Ng^2\mu_B^2}\right)(4J_2),\\[6pt]\lambda_d &= -\left(\frac{2}{Ng^2\mu_B^2}\right)(4J_1 + 2J_c),\end{aligned} \tag{35}$$

which yield

$$\lambda_s - \lambda_d = \left(\frac{2}{Ng^2\mu_B^2}\right)(4J_1 + 2J_c - 4J_2). \tag{36}$$

Inserting this expression into Eq. (34) for G-type antiferromagnets gives

$$\left[\frac{\chi_0(T_N)}{Ng^2\mu_B^2/k_B}\right]\frac{4J_1 + 2J_c - 4J_2}{k_B} = 1. \tag{37}$$

This is a constraint on the exchange parameters in $BaMn_2As_2$ in addition to those in Eqs. (4). If $\chi_0(T)$ is the spin susceptibility per mole of spins, then N is Avogadro's number N_A. Taking $g = 2$ we have

$$\frac{N_A g^2 \mu_B^2}{k_B} = 1.500 \ \frac{cm^3}{mol} \tag{38}$$

and Eq. (37) becomes

$$\frac{4J_1 + 2J_c - 4J_2}{k_B} = \frac{1.500 \ cm^3/mol}{\chi_0(T_N)}. \tag{39}$$

In the following sections we assume that the spin susceptibility in the absence of any explicit exchange fields follows a Curie law, $\chi_0(T) = C/T$. Then Eqs. (24) and (39) yield

$$\frac{2J_1 + J_c - 2J_2}{k_B} = \frac{3T_N}{2S(S+1)}, \tag{40}$$

or

$$T_N = \frac{2(2J_1 + J_c - 2J_2)}{3k_B}S(S+1). \tag{41}$$

Substituting Eq. (41) into (36) gives

$$\lambda_s - \lambda_d = \frac{6k_B T_N}{Ng^2 S(S+1)\mu_B^2}. \tag{42}$$

It is useful to express differently how the NNN intrasublattice interaction J_2 affects T_N. From Eq. (41), one obtains

$$\frac{T_N(J_2)}{T_N(J_2 = 0)} = 1 - \frac{2J_2}{2J_1 + J_c}, \tag{43}$$

which is independent of the spin S and only depends on the ratio of the intrasublattice exchange constant J_2 to the net intersublattice exchange constant $2J_1 + J_c$. From Fig. 2 and Eq. (43), an antiferromagnetic $J_2 > 0$ is frustrating for G-type AF ordering and hence lowers T_N, whereas a ferromagnetic $J_2 < 0$ is nonfrustrating for G-type AF ordering and instead enhances T_N.

A. Néel temperature reduction factor f

One can define a Néel temperature reduction factor f for antiferromagnets by

$$f = \frac{\theta}{T_N}, \tag{44}$$

where θ is the positive AF Weiss temperature in the Curie-Weiss law in Eq. (22). For molecular field bipartite antiferromagnets with only nearest-neighbor interactions, $f = 1$.[31] However, there are four classes of AF materials in which f can be much different from unity: (1) materials in which fluctuation effects associated with a low dimensionality (0, 1, or 2) of the spin lattice are strong, (2) three-dimensional materials in which geometric frustration for AF ordering occurs, (3) spin lattices in which the signs of the exchange interactions of a spin with its neighbors frustrate the ordering, and/or (4) spin lattices that are not bipartite; that is, interactions between spins on the same sublattice occur. In each of these classes of materials, T_N can be strongly suppressed, sometimes to $T = 0$, which gives $f \gg 1$. Alternatively, it can occur that second neighbor interactions can enhance T_N but suppress $|\theta|$, as we see below in Eq. (45) if J_2 is negative (ferromagnetic). It can occur that a given compound belongs to more than one class.

One of us has discussed class (1) in the context of low-dimensional copper oxide compounds such as quasi-two-dimensional La_2CuO_4 containing a Cu^{2+} d^9 spin-1/2 square lattice and quasi-one-dimensional Sr_2CuO_3 containing Cu^{2+} d^9 spin-1/2 chains.[6] In these materials the AF correlation length ξ grows with decreasing T. In La_2CuO_4, long-range AF ordering occurs at $T_N \sim \pi(\xi/a)^2 J_c/k_B$, where the number of spins within an AF correlated area in the plane is $N_\xi \sim \pi(\xi/a)^2$, J_c is the interplane nearest-neighbor exchange coupling constant, and a is the square lattice parameter. A large number N_ξ of spins within a correlated area amplifies the effect of a small J_c. In Sr_2CuO_3, N_ξ grows much more slowly with decreasing T than in La_2CuO_4 because what is relevant here is the number of spins within a correlation length rather than within a correlation area, and the former is much smaller than the latter at the same temperature. Hence, one expects f for Sr_2CuO_3 to be much larger than for La_2CuO_4, as observed. The ξ and the Weiss temperature θ are determined by the in-chain or in-plane exchange coupling $J_{ab} \gg J_c$, respectively, and hence $T_N \ll \theta$ for both compounds.

Ramirez has extensively discussed class (2).[35] In frustrated three-dimensional antiferromagnets, the susceptibility follows a Curie-Weiss-like temperature dependence down to

temperatures much less than θ. One can describe the physics in two equivalent ways. In one view, the AF correlation length ξ does not grow as fast as one would predict from the Curie-Weiss law where one expects ξ to diverge at the mean-field $T_N = \theta$. An alternate equivalent explanation is that because the Curie-Weiss law holds to low temperatures $T \ll \theta$, which results in $f \gg 1$, the coefficients of the higher order $1/T^n$ terms ($n > 1$) in the high-temperature series expansions of the two-spin correlation functions in Eqs. (A4) and (A5) in Appendix A are strongly suppressed in frustrated antiferromagnets. $BaMn_2As_2$ likely belongs to classes (1), (3), and (4).

Using Eqs. (27) and (41) which assume $\chi_0 = C/T$ and J_1, $J_c > 0$, the ratio of the Weiss temperature to the Néel temperature for G-type antiferromagnets in the J_1-J_2-J_c model within MFT is

$$f = \frac{\theta}{T_N} = \frac{2J_1 + J_c + 2J_2}{2J_1 + J_c - 2J_2} = \frac{1 + \frac{2J_2}{2J_1+J_c}}{1 - \frac{2J_2}{2J_1+J_c}}, \quad (45)$$

which gives

$$\frac{2J_2}{2J_1 + J_c} = \frac{f - 1}{f + 1}. \quad (46)$$

Thus, f depends on the sign and magnitude of the NNN in-plane interaction J_2. For an antiferromagnetic $J_2 > 0$, one gets $f > 1$, whereas for a ferromagnetic $J_2 < 0$, one gets $f < 1$. The constraint on J_2 in Eqs. (4) that $J_2 < J_1/2$ still applies, giving an upper limit (for which $J_c = 0$) of

$$f < 3 \quad \text{(for G-type AF ordering).} \quad (47)$$

Using Eq. (46), one can rewrite Eq. (43) as

$$\frac{T_N(J_2)}{T_N(J_2 = 0)} = \frac{2}{f + 1}. \quad (48)$$

In MFT in the paramagnetic state, the spin susceptibility (22) follows the Curie-Weiss law $\chi(T) = C/(T + \theta)$, and $\chi(T)$ reaches a maximum at $T = T_N$. Therefore, we obtain the product

$$\chi_{\text{spin}}^{\text{max}} T^{\text{max}} = \chi_{\text{spin}}^{\text{max}}(T_N) T_N = \frac{C}{T_N + \theta} T_N$$
$$= \frac{C}{T_N(1 + f)} T_N = \frac{C}{1 + f}$$
$$= \frac{0.5002 \, S(S + 1)}{1 + f} \frac{\text{cm}^3 \, \text{K}}{\text{mol spins}}, \quad (49)$$

where we used Eq. (24) in the last equality. This gives

$$f = \frac{(0.5002 \, \text{cm}^3 \, \text{K/mol spins}) S(S + 1)}{\chi_{\text{spin}}^{\text{max}} T^{\text{max}}} - 1. \quad (50)$$

From Eqs. (40) and (49) one can solve for $2J_1 + J_c$ and J_2 to obtain

$$\frac{2J_1 + J_c}{k_B} = \frac{(3 \, \text{cm}^3 \, \text{K/mol}) T_N}{8 \chi_{\text{spin}}^{\text{max}} T^{\text{max}}},$$
$$\frac{J_2}{k_B} = \frac{2J_1 + J_c}{2k_B} - \frac{3T_N}{4S(S + 1)}. \quad (51)$$

Additional useful expressions include the following. From Eqs. (27), (41), and (44) one obtains

$$2J_1 + J_c = \frac{3k_B T_N(f + 1)}{4S(S + 1)}. \quad (52)$$

Then from Eq. (46) one gets

$$2J_2 = \frac{3k_B T_N(f - 1)}{4S(S + 1)}. \quad (53)$$

Now using Eqs. (52) and (53) we can rewrite the molecular field coupling constants in Eqs. (35) in the simple symmetric forms

$$\lambda_s = -\frac{T_N(f - 1)}{C}, \quad \lambda_d = -\frac{T_N(f + 1)}{C}, \quad (54)$$

where C is the Curie constant in Eq. (23).

B. Anisotropic $\chi(T)$ below T_N

We would like to compare our experimental anisotropic $\chi(T)$ data below T_N with the MFT predictions using the J_1-J_2-J_c model. We discuss first the perpendicular susceptibility $\chi_\perp$ and then the parallel susceptibility $\chi_\parallel$, where $\chi_\perp$ refers to the susceptibility with the applied magnetic field perpendicular to the easy axis of the collinear antiferromagnetic structure and $\chi_\parallel$ to the susceptibility when the applied magnetic field is parallel to it. For $BaMn_2As_2$, $\chi_\parallel = \chi_c$ and $\chi_\perp = \chi_{ab}$. In the Heisenberg model, above T_N the susceptibility is isotropic and hence $\chi_\parallel = \chi_\perp$. Below T_N, $\chi_\perp$ and $\chi_\parallel$ are no longer the same.

Below T_N of a collinear antiferromagnet, one always has $\chi_\parallel < \chi_\perp$ (see also Fig. 13 below). Since the magnetic energy of the system at low fields is $-(1/2)\chi H^2$, if the field is aligned along the ordered moment axis the spin system can lower its energy via a "spin-flop" transition where the ordered moment axis rotates to be perpendicular to the applied field. To prevent this from happening, one needs to have an anisotropy energy present that is not included in the Heisenberg Hamiltonian. Otherwise one could never measure $\chi_\parallel$. An important example of such an anisotropy energy is the axial single-ion anisotropy energy with the form DS_z^2 (for $S > 1/2$) and $D < 0$, and/or higher order forms, that arise from the spin-orbit interaction of the magnetic moments with the crystalline electric field of the lattice. Here we assume that an infinitesimal axial anisotropy is present with sufficient magnitude to prevent the ordered moment axis from flopping from the parallel to the perpendicular orientation when we are measuring the parallel magnetization in the limit of an infinitesmal field. We do not further consider the spin-flop transition in this paper.

The $\chi_\perp(T)$ and $\chi_\parallel(T)$ are derived for the J_1-J_2-J_c model at $T \leqslant T_N$ in Appendix B. For the perpendicular susceptibility, one obtains the constant value

$$\chi_\perp = \frac{1}{|\lambda_d|} = \frac{C}{T_N(1 + f)} = \frac{C}{T_N + \theta} = \chi(T_N), \quad (T \leqslant T_N),$$
$$(55)$$

using $f \equiv \theta/T_N$. This result is similar to that for a bipartite lattice,[31] except in that case one has $\theta = T_N$, whereas in our case we have $\theta = fT_N$ with, in general, $f \neq 1$ from Eq. (45). The estimated values of f from Eqs. (60) below
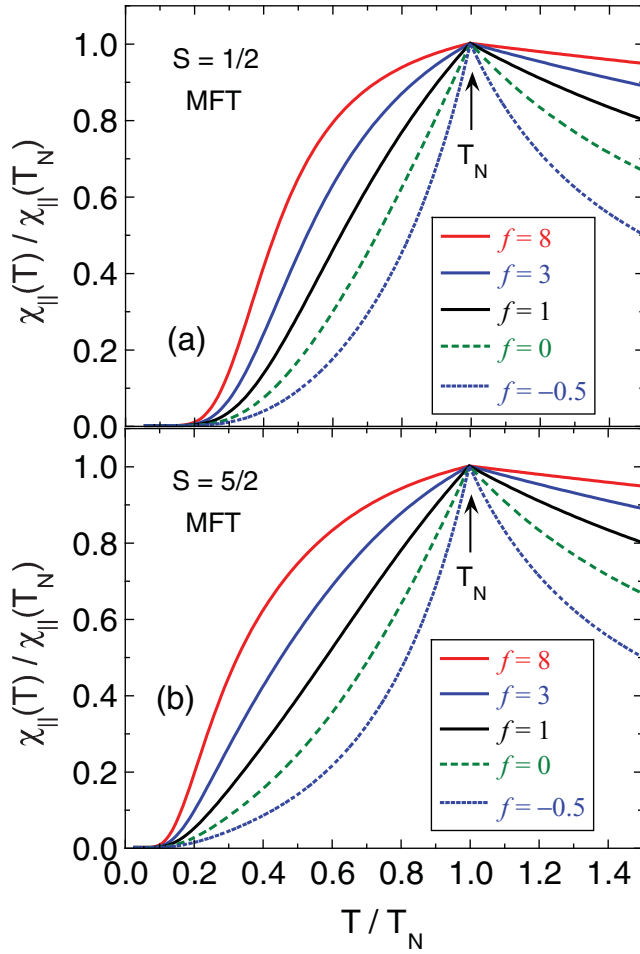
FIG. 8. (Color online) Parallel susceptibility $\chi_\parallel$ versus temperature T through the Néel temperature T_N for G-type AF ordering using the J_1-J_2-J_c model in MFT for various values of $f = \theta/T_N$, as listed, for spins (a) $S = 1/2$ and (b) $S = 5/2$. The order of the curves from top to bottom is the same as in the figure legends. At temperatures $T > T_N$, χ is isotropic. For $T < T_N$, the perpendicular susceptibility is constant, $\chi_\perp = \chi_\perp(T_N)$ (not shown). The G-type AF state is unstable against the stripe-AF state for $f > 3$.

are $\sim$3–5 in BaMn$_2$As$_2$; that is, T_N is much smaller than θ, but within MFT the susceptibility still follows the Curie-Weiss law $\chi = C/(T + \theta)$ down to T_N. This interesting behavior is the result of bond frustration for AF ordering (the antiferromagnetic NNN interaction J_2 frustrates the occurrence of G-type AF ordering) and has been noted as a property of geometrically frustrated antiferromagnets.[35]

The dependence of $\chi_\parallel(T)/\chi_\parallel(T_N)$ on $t \equiv T/T_N$ determined by solving Eqs. (B13), (B14), and (B18) is shown in Figs. 8(a) and 8(b) for spins $S = 1/2$ and $S = 5/2$, respectively, for various values of $f = \theta/T_N$. The value $f = 1$ corresponds to the conventional nonfrustrated bipartite stacked square spin lattice as in the top panel of Fig. 2 with $J_2 = 0$. Figure 8 shows that the presence of a nonzero diagonal coupling J_2 has a strong influence on $\chi_\parallel(T)/\chi_\parallel(T_N)$. Complementary plots of $\chi_\parallel(T)/\chi_\parallel(T_N)$ versus T/T_N at fixed $f = 0$, 1, and 3 for $S = 1/2$, 5/2, and 10 are shown in Fig. 9.
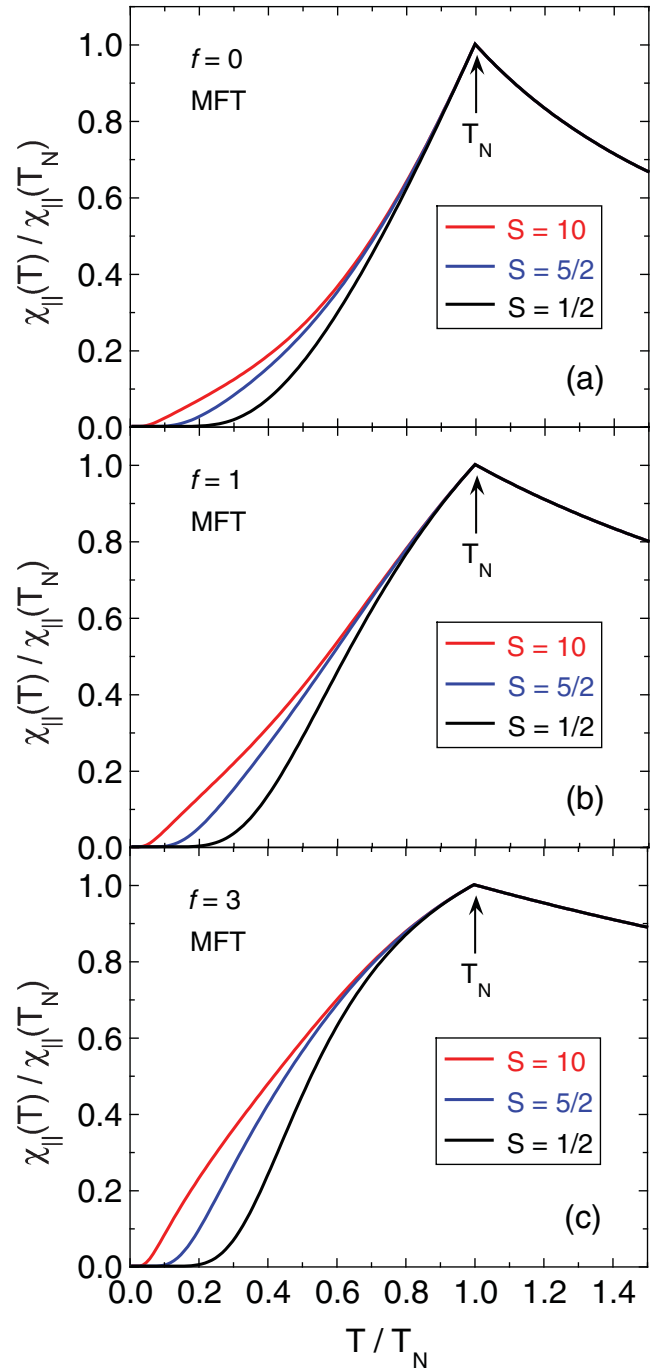

FIG. 9. (Color online) Parallel susceptibility $\chi_\parallel$ versus temperature T through the Néel temperature T_N for the J_1-J_2-J_c model in MFT for spins $S = 1/2$, 5/2, and 10 and $f = \theta/T_N$ values of (a) 0, (b) 1, and (c) 3. The order of the curves in each panel from top to bottom is the same as in the figure legends. The value $f = 1$ corresponds to the conventional bipartite lattice with $J_2 = 0$.

C. Ordered moment versus temperature below T_N

The ordered moment in the antiferromagnetic state of BaMn$_2$As$_2$, which is the staggered moment $\mu_z^\dagger$ in Eq. (B16), has been previously measured, but not modeled.[13] In Appendix C we determine the MFT predictions on the basis of the J_1-J_2-J_c model. In Fig. 10 are plotted the solutions
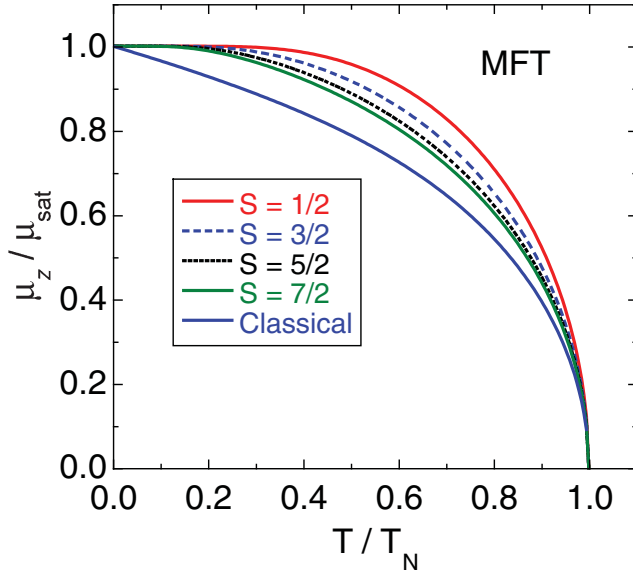
FIG. 10. (Color online) Ordered moment $\mu_z \equiv \mu_z^{\dagger}$ versus temperature T from molecular field theory of the J_1-J_2-J_c model for a collinear antiferromagnet for classical spins and for several quantum spins as listed, where the saturation moment is $\mu_{\mathrm{sat}} = gS\mu_{\mathrm{B}}$. The order of the curves from top to bottom is the same as in the figure legend. Remarkably, the results are independent of J_2.

of Eq. (C1) for the nonzero ordered moment $\mu_z \equiv \mu_z^{\dagger}$ versus reduced temperature T/T_{N} for classical spins and for four values of quantum spins. In contrast to quantum spins for which $\mu_z^{\dagger}$ approaches the respective saturation moment $\mu_{\mathrm{sat}} = gS\mu_{\mathrm{B}}$ exponentially fast for $T \to 0$ due to an energy gap between the ground state and the lowest excited states, the low-temperature classical behavior is linear. This results in a magnetic heat capacity $C_{\mathrm{mag}} \to \mathrm{constant} \neq 0$ as $T \to 0$ for classical spins, which violates the third law of thermodynamics, whereas for quantum spins $C_{\mathrm{mag}} \to 0$ as $T \to 0$ (see Fig. 11 below).

Interestingly, the parameter $f = \theta/T_{\mathrm{N}}$ that characterizes the influence of J_2 on the magnetism has disappeared from the expression for $\mu_z^{\dagger}(T)$ in Eq. (B16) when the temperature scale is normalized by T_{N}. Thus, Eq. (C1) and the plots in Fig. 10 are identical to the corresponding MFT predictions for an AF bipartite spin lattice with $J_2 = 0$. However, in our case with $J_2 \neq 0$, we must keep in mind that J_2 has already manifested its influence on the magnetism by changing T_{N}.

D. Zero-field magnetic heat capacity C_{mag} and entropy S_{mag} below T_{N}

The zero-field magnetic heat capacity $C_{\mathrm{mag}}(T)$ is derived in MFT in Appendix D as

$$\frac{C_{\mathrm{mag}}(t)}{R} = -\frac{3S}{S+1}\bar{\mu}_z^{\dagger}(t)\frac{d\bar{\mu}_z^{\dagger}(t)}{dt}, \qquad (56)$$

where $t = T/T_{\mathrm{N}}$ is the reduced temperature and $\bar{\mu}_z^{\dagger} = \mu_z^{\dagger}/\mu_{\mathrm{sat}}$ is the reduced ordered (staggered) moment. Since $\bar{\mu}_z^{\dagger}$ does not explicitly depend on J_2 as discussed above, neither does $C_{\mathrm{ave}}(T/T_{\mathrm{N}})$, but rather implicitly via the dependence of T_{N} on
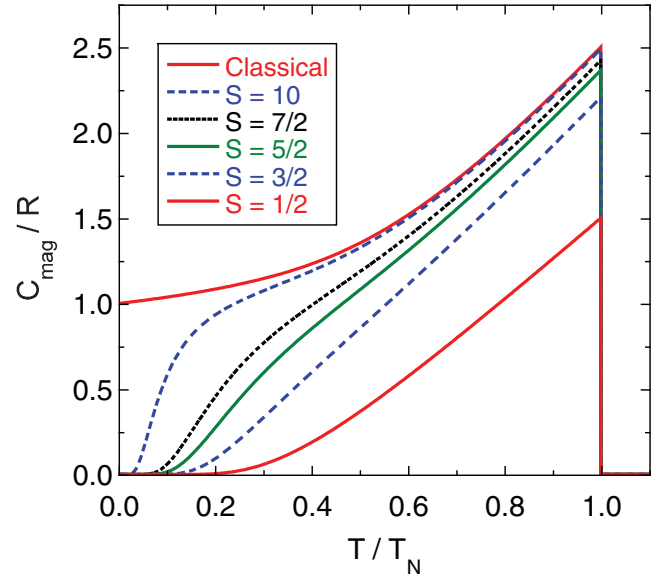

FIG. 11. (Color online) Magnetic component of the heat capacity C_{mag}, divided by the molar gas constant R, versus the ratio of the temperature T to the Néel temperature T_{N} according to the molecular field theory [Eq. (56)] of the J_1-J_2-J_c model for a collinear antiferromagnet for classical spins and for several quantum spins as listed. The order of the curves from top to bottom is the same as in the figure legend. As in Fig. 10, the results are independent of J_2.

J_2. The $\bar{\mu}_z^{\dagger}(t)$ is determined by numerically solving Eq. (C1). Inserting this result into (56), $C_{\mathrm{mag}}(T)$ was calculated for several spin values as plotted in Fig. 11. One observes a triangular shape for $C_{\mathrm{mag}}(t)$ near T_{N} for each S, which is characteristic of the mean-field solution, with a discontinuous increase ("jump") in $C_{\mathrm{mag}}(T)$ upon decreasing T through T_{N} given by[36]

$$\frac{\Delta C_{\mathrm{mag}}(T_{\mathrm{N}})}{R} = \frac{5}{2}\left[\frac{(2S+1)^2 - 1}{(2S+1)^2 + 1}\right], \qquad (57)$$

where $2S + 1$ is the Zeeman degeneracy in zero field for a spin S. There is not a large range of ΔC_{mag} possible upon varying the spin S. From Eq. (57) one obtains

$$\frac{\Delta C_{\mathrm{mag}}(T_{\mathrm{N}})}{R} = \frac{3}{2} \quad \left(S = \frac{1}{2}\right),$$

$$\frac{\Delta C_{\mathrm{mag}}(T_{\mathrm{N}})}{R} = \frac{5}{2} \quad (S = \infty),$$

consistent with Fig. 11.

The evolution in Fig. 11 of the low temperature $C_{\mathrm{mag}}(T)$ with increasing spin S is interesting. It develops a hump at a temperature that decreases with increasing S, until in the classical limit $S \to \infty$ the hump merges into the classical finite-value behavior for $T \to 0$. The hump is required in order that the entropy of the disordered spin system increase with increasing S (see below), since $C_{\mathrm{mag}}(T)$ is bounded from above by the classical prediction. For quantum spins, the heat capacity approaches zero exponentially at sufficiently low temperatures irrespective of the (finite) spin value, whereas for
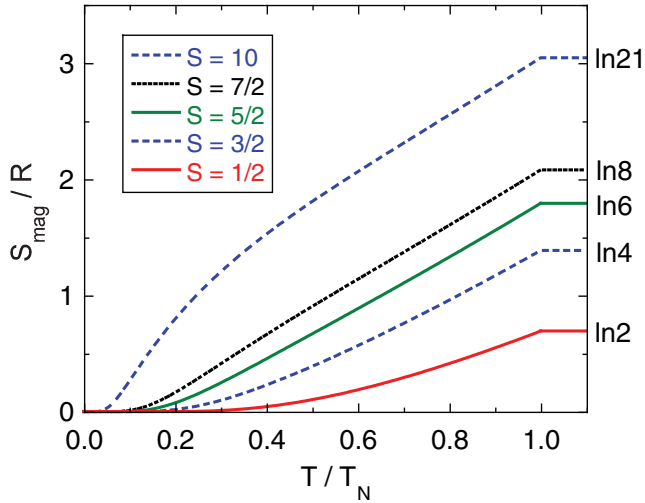
FIG. 12. (Color online) Magnetic entropy $S_{\rm mag}/R$ for quantum spins versus reduced temperature $T/T_{\rm N}$ according to molecular field theory for the quantum spins S indicated. The order of the curves from top to bottom is the same as in the figure legend. In the disordered state at $T > T_{\rm N}$, the magnetic entropy is the constant value $S_{\rm mag} = R \ln(2S + 1)$ for each S, as indicated along the right-hand ordinate.

classical spins the heat capacity approaches a nonzero finite value for $T \to 0$.

The magnetic entropy $S_{\rm mag}$ is determined from the magnetic heat capacity via

$$\frac{S_{\rm mag}(t)}{R} = \int_0^t \frac{C_{\rm mag}(t)/R}{t} \, dt. \tag{58}$$

The magnetic entropy obtained from Eq. (58) and from the data in Fig. 11 is plotted versus temperature for quantum spins in Fig. 12. The constant values for $T \geqslant T_{\rm N}$ as indicated by the notations on the right-hand ordinate agree with the values expected for disordered spins given by the molar magnetic entropy $S_{\rm mag} = R \ln(2S + 1)$. For classical spins the calculated entropy for $T \to 0$ is $S_{\rm mag}(T \to 0^+)/R = \lim_{T \to 0} \ln[T/(0\,{\rm K})] = \infty$, which violates the third law of thermodynamics.

VIII. COMPARISON OF THEORETICAL PREDICTIONS WITH EXPERIMENTAL DATA FOR BaMn₂As₂

A. Comparisons with molecular field theory

We expect the Mn^{+2} d^5 ion in BaMn₂As₂ to have the high-spin configuration with spin $S = 5/2$. On the other hand, the observed ordered moment is $\mu = 3.9(1)\,\mu_{\rm B}/$Mn (Ref. 13), suggesting from the relation $\mu = gS\mu_{\rm B}$ with $g = 2$ that $S = 2$. Therefore, in the following we consider both of these possibilities.

1. Néel temperature

Using Eq. (40) and $T_{\rm N} = 625$ K for BaMn₂As₂, one obtains

$$\frac{2J_1 + J_c - 2J_2}{k_{\rm B}} = 156 \text{ K} \quad (S = 2)$$

$$= 107 \text{ K} \quad (S = 5/2). \tag{59}$$

2. Magnetic susceptibility

Inserting the experimental $\chi_{\rm spin}^{\rm max} T^{\rm max}$ value from Eq. (20) into (50) gives

$$f = 2.75 \quad (S = 2),$$

$$= 4.47 \quad (S = 5/2). \tag{60}$$

According to Eq. (47), the value of f for $S = 5/2$ is not possible for G-type AF ordering and hence $S = 5/2$ is ruled out by this criterion. The f value for $S = 2$ suggests that interlayer coupling might have a significant effect on the observed magnetic susceptibility above $T_{\rm N}$. On the other hand, for the layered cuprate La₂CuO₄ one has $z = 4$, $J/k_{\rm B} = 1600$ K, $S = 1/2$, and $T_{\rm N} = 325$ K (Ref. 6), which yields a Weiss temperature $\theta = 1600$ K and $f = 4.9$, and the magnetism of this compound is known to be described very well by two-dimensional physics in the temperature range above $T_{\rm N}$ (Ref. 6). As a further comparison, the quasi-one-dimensional spin-1/2 chain compound Sr₂CuO₃ has $z = 2$, $J/k_{\rm B} = 2200$ K, $S = 1/2$, and $T_{\rm N} = 5.4$ K (Ref. 6), which yields $\theta = 1100$ K and $f = 200$. This large f value is the reason that Sr₂CuO₃ is often considered to be a model quasi-one-dimensional Heisenberg antiferromagnet.[6]

Again using the experimental $\chi_{\rm spin}^{\rm max} T^{\rm max}$ value from Eq. (20), Eqs. (51) yield

$$\frac{2J_1 + J_c}{k_{\rm B}} = 293 \text{ K} \quad (S = 2)$$

$$= 293 \text{ K} \quad (S = 5/2),$$

$$\frac{J_2}{k_{\rm B}} = 68 \text{ K} \quad (S = 2)$$

$$= 93 \text{ K} \quad (S = 5/2). \tag{61}$$

The above results, summarized in Table IV, are only approximate qualitative constraints on the exchange parameters in BaMn₂As₂, because they assume that the susceptibility follows the Curie-Weiss law above $T_{\rm N}$, which Fig. 7 shows is not accurate. In particular, if $J_c/J_1 \approx 0.1$, as determined from the neutron scattering results and the theoretical predictions in Sec. XII, one obtains unrealistically large $J_2/J_1 = 0.50$ and 0.67 for $S = 2$ and $S = 5/2$, respectively. The problem stems from the fact that $T^{\rm max}$ and $T_{\rm N}$ do not coincide, which is an inconsistency in the analysis.

A comparison of the MFT predictions below $T_{\rm N}$ of the anisotropic susceptibilities in Eqs. (55) and (B18) with the experimental data from Fig. 7(a) is shown in Fig. 13. For the MFT dashed-line predictions we used Eq. (17) with $\chi_{\rm orb} = 0.2 \times 10^{-3}$ cm³/mol and $\chi_{\rm spin}(T_{\rm N}) = 1.35 \times 10^{-3}$ cm³/mol. We used the value $T_{\rm N} = 625$ K and the MFT parameter $f = 2.75$ listed in Table IV for $S = 2$. The temperature dependences of the MFT predictions for the anisotropic susceptibilities are seen to be in semiquantitative agreement with the experimental data. We do not consider the case $S = 5/2$ because the large $f = 4.47 > 3$ in Eqs. (59) and Table IV for $S = 5/2$ makes the G-type AF structure unstable with respect to the stripe-AF structure in Fig. 2.

TABLE IV. Parameters determined from a fit of magnetic susceptibility data by molecular field theory of G-type antiferromagnetic $BaMn_2As_2$ with NN (J_1), NNN (J_2), and interlayer (J_c) exchange interactions.

Quantity	$S = 2$	$S = 5/2$
$f = \theta/T_N$	2.75	4.47
$(2J_1 + J_c - 2J_2)/k_B$ (K)	156	107
$(2J_1 + J_c)/k_B$ (K)	293	293
$2J_1 + J_c$ (meV)	25.2	25.2
$S(2J_1 + J_c)/k_B$ (K)	586	733
$S(2J_1 + J_c)$ (meV)	50.5	63.2
J_2/k_B (K)	68	93
J_2 (meV)	5.9	8.0
SJ_2/k_B (K)	136	233
SJ_2 (meV)	11.7	20.1

3. Ordered moment

The theoretical MFT results for the ordered moment versus temperature in Fig. 10 for $S = 3/2$ to $S = 5/2$ are nearly the same, so we do not expect to be able to differentiate between the two possibilities of $S = 2$ and $S = 5/2$ for the Mn spins in $BaMn_2As_2$ on the basis of the observed temperature dependence of the ordered moment. This expectation is confirmed in Fig. 14 where we compare the MFT predictions for $S = 1/2$, 2, and 5/2 from Eq. (C1) with the experimental data from magnetic neutron diffraction measurements in Ref. 13. Although the overall temperature dependence of the data agrees with MFT, the data are not quantitatively fitted by the prediction for any particular fixed S value.

4. High-temperature magnetic heat capacity

Here we compare our experimental heat capacity C_p data for $BaMn_2As_2$ single crystals at temperatures up to 350 K with the prediction of MFT for the magnetic heat capacity C_{mag} at high temperatures, that is, near room temperature. To do this

FIG. 14. (Color online) Ordered moment μ_z versus temperature T measured for $BaMn_2As_2$ from Ref. 13 (solid red circles). The Néel temperature T_N and saturation moment μ_{sat} are given in the figure. Also shown are the MFT predictions for quantum spins $S = 1/2$, 2, and 5/2 from Eq. (C1) (solid and dashed curves), where the order of the curves from top to bottom is the same as in the figure legend.

we need to estimate the lattice heat capacity contribution using the Debye model.

The heat capacity at constant pressure $C_p(T)$ for a single crystal of $BaMn_2As_2$, previously reported by Singh *et al.*,[11] is shown in Fig. 15 for the measured temperature range 2–350 K.
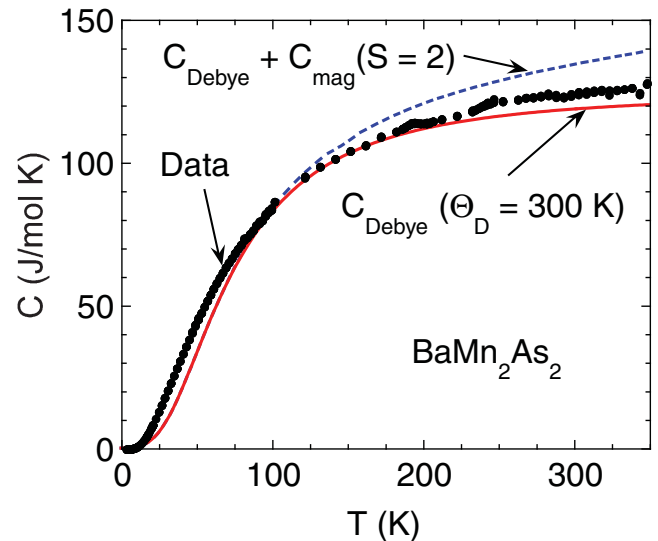
FIG. 15. (Color online) Heat capacity C versus temperature T. The experimental $C_p(T)$ data obtained for a single crystal of $BaMn_2As_2$ (Ref. 11) are shown as the solid black circles. The lattice heat capacity for a Debye temperature $\Theta_D = 300$ K is plotted versus T as the solid red curve. The sum of the lattice heat capacity and the magnetic heat capacity for spin $S = 2$ is shown as the dashed blue curve.
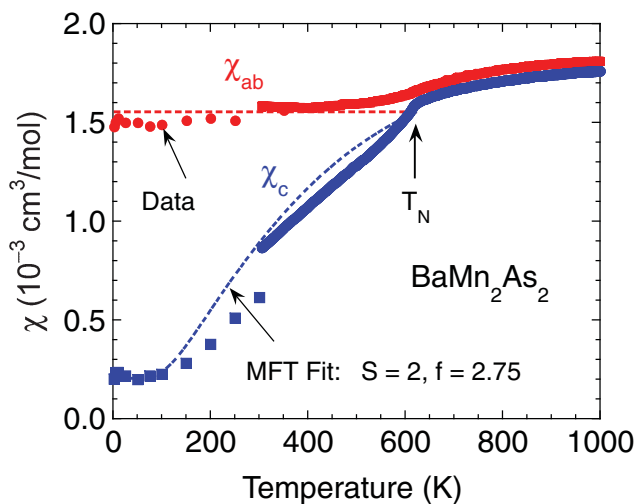

FIG. 13. (Color online) Comparison of the MFT prediction below T_N of the anisotropic susceptibilities in Eqs. (55) and (B18) versus temperature with the experimental data from Fig. 7(a).
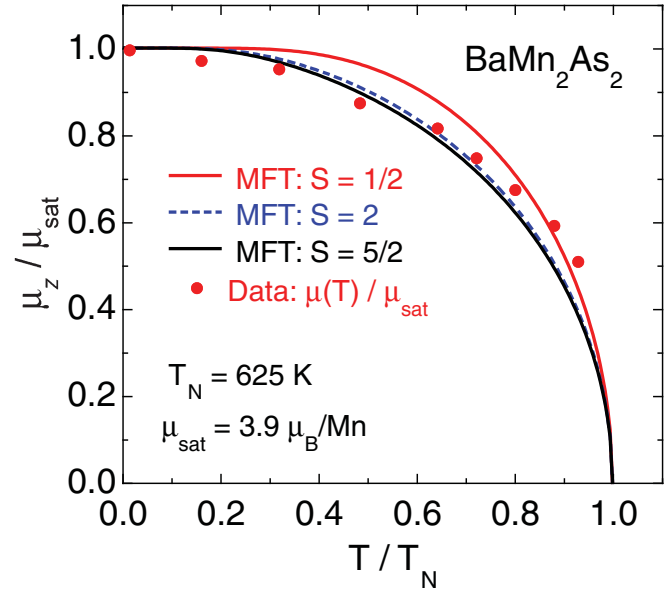
We fitted the data by the Debye function for the molar lattice heat capacity of acoustic phonons at constant volume, given by[31]

$$C_{\text{Debye}} = 9nR \left(\frac{T}{\Theta_D} \right)^3 \int_0^{\Theta_D/T} \frac{x^4 e^x}{(e^x - 1)^2} \, dx, \qquad (62)$$

where n is the number of atoms per formula unit ($n = 5$ here) for various values of the Debye temperature Θ_D. In order that $C_{\text{Debye}}(T)$ does not lie above the experimental data over any temperature range, the minimum value of Θ_D is about 300 K, for which the Debye function is plotted as the solid red curve in Fig. 15. The Θ_D is evidently temperature-dependent because the deviation of the curve from the experimental data varies nonmonotonically with temperature. From the same set of experimental $C_p(T)$ data,[11] at low temperatures $T \leqslant 5$ K a value $\Theta_D = 246(4)$ K was deduced using the Debye T^3 law [the low-temperature limit of Eq. (62)] given by[31]

$$C_{\text{Debye}} = \beta_D T^3, \quad \beta_D = 0.65(3) \, \frac{\text{mJ}}{\text{mol K}^4},$$
$$\Theta_D = \left(\frac{12\pi^4 Rn}{5\beta_D} \right)^{1/3}. \qquad (63)$$

The experimental data at the highest temperatures lie above the lattice heat capacity curve for $\Theta_D = 300$ K in Fig. 15, suggesting the presence of one or more heat capacity contributions in addition to that due to acoustic phonons.

We calculated the difference $C_p - C_V$ for the lattice heat capacity for the compound $BaFe_2As_2$, where C_V is the lattice heat capacity at constant volume, according to the thermodynamic relation $C_p - C_V = V_M \beta_V^2(T) B(T) T$, where V_M is the molar volume, β_V is the volume thermal expansion coefficient, and B is the bulk modulus. For the 200–300 K temperature range, using the values $\beta_V \approx 4.8 \times 10^{-5}$ K^{-1} (Ref. 37), $B = 6.6 \times 10^{12}$ dyne/cm^2 (Ref. 38), and $V_M = 61.5$ cm^3/mol (Ref. 4), we obtained $C_p - C_V = (9.3 \text{ mJ/mol K}^2)T$. This gives $(C_p - C_V)(300$ K$) = 2.8$ J/mol K, which is about a factor of two too small to account for the difference between the data and the Debye curve. It was not possible to calculate a value of $C_p - C_V$ specific to $BaMn_2As_2$ because $\beta_V(T)$ and $B(T)$ have not been measured for this compound.

The magnetic contribution $C_{\text{mag}}(T)$ to the heat capacity at high temperatures was calculated using the MFT prediction in Eq. (56). We chose to calculate it for spin $S = 2$ because the $S = 5/2$ possibility was ruled out by the large value of $f > 3$ for spin $S = 5/2$ in Eq. (60). Using $T_N = 625$ K, the $C_{\text{mag}}(T)$ from two moles of spins $S = 2$ per mole of $BaMn_2As_2$ was added to the Debye heat capacity and is plotted as the dashed blue curve in Fig. 15. Now the calculated curve lies above the experimental data around room temperature, indicating that the magnetic heat capacity is smaller than predicted by MFT. The $\chi(T)$ data in Fig. 7(a) appear to be approaching a maximum at a temperature $T^{\max} \approx 1000$ K that is far above $T_N = 625$ K, indicating the occurrence of strong short-range AF ordering above T_N (see also Sec. IX below). This removes spin entropy and decreases C_{mag} below the value expected from MFT at temperatures below T_N. This may be the reason for the suppression of $C_{\text{mag}}(T)$ in our measurements around room temperature.

B. Comparison of experiment with spin wave heat capacity theory at low temperatures in the J_1-J_2-J_c model

1. Theory

The lack of significant susceptibility anisotropy above T_N in Fig. 7 indicates that single-ion anisotropy is small. This anisotropy, if present, gives rise to an energy gap in the spin wave excitation spectrum. Here we assume that the anisotropy gap is infinitesmally small and calculate the low-temperature magnetic heat capacity of AF spin waves in the J_1-J_2-J_c model. This is an extension of the standard treatment for simple cubic spin lattices with isotropic NN exchange interactions.

The original 1952 papers by Anderson[39] and by Kubo[40] give a clear prescription of how to do this using a spin wave model with two AF sublattices 1 and 2 containing a total of N spins S. Their starting Heisenberg Hamiltonian is

$$\mathcal{H} = J \sum_{\langle ij \rangle} \mathbf{S}_i \cdot \mathbf{S}_j, \qquad (64)$$

where there is only a single J and the sum is over distinct nearest-neighbor spin pairs. In zero field and in the absence of significant anisotropy the diagonalized spin wave Hamiltonian contains the following term involving the excitation energies of spin waves

$$E = \sum_{\mathbf{q}} \left(n_{1\mathbf{q}} \hbar \omega_{1\mathbf{q}} + n_{2\mathbf{q}} \hbar \omega_{2\mathbf{q}} \right), \qquad (65)$$

where $\mathbf{q}$ is the wave vector of a spin wave excitation, $n_{i\mathbf{q}}$ is the occupation number of the mode for sublattice i, and the two terms correspond to excitations on the two degenerate spin wave branches $\omega_{1\mathbf{q}}$ and $\omega_{2\mathbf{q}}$ associated with the two spin sublattices, respectively. Since $n_{1\mathbf{q}} \hbar \omega_{1\mathbf{q}} = n_{2\mathbf{q}} \hbar \omega_{2\mathbf{q}} \equiv n_{\mathbf{q}} \hbar \omega_{\mathbf{q}}$ are degenerate, the excitation energy of the system can be written

$$E = 2 \sum_{\mathbf{q}} n_{\mathbf{q}} \hbar \omega_{\mathbf{q}}. \qquad (66)$$

The thermal-average energy of the spin waves is then

$$E_{\text{ave}} = 2 \sum_{\mathbf{q}} \frac{\hbar \omega_{\mathbf{q}}}{e^{\hbar \omega_{\mathbf{q}}/k_B T} - 1}, \qquad (67)$$

where $\langle n_{\mathbf{q}} \rangle = 1/(e^{\hbar \omega_{\mathbf{q}}/k_B T} - 1)$ is the Planck distribution function for the thermal-average number of quanta in an oscillator at energy $\hbar \omega_{\mathbf{q}}$. One converts the sum into an integral over $\mathbf{q}$ for a three-dimensional spin lattice via

$$\sum_{\mathbf{q}} \rightarrow \frac{N}{2} \frac{V_{\text{spin}}}{(2\pi)^3} \int_{-\pi/a}^{\pi/a} \int_{-\pi/b}^{\pi/b} \int_{-\pi/c}^{\pi/c} d\mathbf{q}, \qquad (68)$$

where V_{spin} is the volume per spin. The factor of $N/2$ arises because each spin sublattice has $N/2$ spins. Then Eq. (67) becomes

$$E_{\text{ave}} = \frac{N V_{\text{spin}}}{(2\pi)^3} \int_{-\pi/a}^{\pi/a} dq_x \int_{-\pi/b}^{\pi/b} dq_y$$
$$\times \int_{-\pi/c}^{\pi/c} dq_z \frac{\hbar \omega_{\mathbf{q}}}{e^{\hbar \omega_{\mathbf{q}}/k_B T} - 1}. \qquad (69)$$

Note that the integration in Eq. (69) is over the entire *Brillouin zone of the primitive direct lattice* (containing a

single spin), not over the Brillouin zone of the magnetic lattice. The reason for this important fact is that integrating over the Brillouin zone of a primitive space lattice with one spin in the basis sums up the response of a single spin, whereas if one were to integrate over an antiferromagnetic Brillouin zone, this zone would include the response of more than one spin. Indeed, the average energy per spin calculated this way does not depend on the type of magnetic ordering at all, even if the magnetic ordering is ferromagnetic or incommensurate. The only relevant difference between the thermal average energy per spin of different magnetic ordering configurations is the difference between the specific $\omega_{\mathbf{q}}$ functions and their degeneracies over the Brillouin zone of the primitive space lattice.

The dispersion relation for a general spin lattice is

$$\hbar\omega_{\mathbf{q}} = zJS\sqrt{1 - \gamma_{\mathbf{q}}^2}, \tag{70}$$

where

$$\gamma_{\mathbf{q}} = \frac{1}{z}\sum_{i=1}^{z} e^{i\mathbf{q}\cdot\mathbf{r}_i}, \tag{71}$$

z is the coordination number of a spin on one sublattice by spins on the other sublattice, and $\mathbf{r}_i$ is a vector from a spin to one of its z neighbors. We now need to make a point that will be illustrated using the spin wave spectrum of an isotropic two-dimensional square spin-S lattice ($z = 4$). In this case Eq. (71) yields

$$\gamma_{\mathbf{q}} = \tfrac{1}{2}[\cos(k_x a) + \cos(k_y a)]$$

and Eq. (70) gives the doubly degenerate dispersion relation as

$$\hbar\omega_{\mathbf{q}} = 4JS\sqrt{1 - [\cos(k_x a) + \cos(k_y a)]^2/4}. \tag{72}$$

This dispersion relation is plotted in Fig. 16. One sees that $\omega_{\mathbf{q}}$ has doubly degenerate branches arising from zero energy at the Γ point $(0,0)$, as expected, but also at the corners of the Brillouin zone at $(\frac{\pi}{a}, \frac{\pi}{a})$ and equivalent points. In a three-dimensional spin lattice with $J_c \neq 0$, using the dispersion relation in Eq. (12), one sees that the low-energy
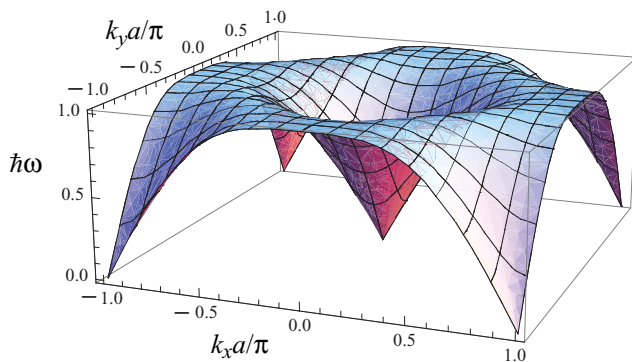

FIG. 16. (Color online) Spin wave dispersion relation $\hbar\omega/4J_1S$ of the isotropic two-dimensional square lattice over the Brillouin zone of the primitive tetragonal *space* lattice. The dispersion relation is doubly degenerate everywhere. At low temperatures, there are two distinct doubly degenerate spin wave branches that are relevant, one at the Γ point at $(0,0)$ and the other at $(\frac{\pi}{a}, \frac{\pi}{a})$ (and equivalent points).

points of the dispersion relation move from the $(\frac{\pi}{a}, \frac{\pi}{a}, 0)$ points in the corners of the two-dimensional Brillouin zone to the $(\frac{\pi}{a}, \frac{\pi}{a}, \frac{\pi}{c})$ and equivalent points at the other four corners of the three-dimensional Brillouin zone. Thus, in either case there is another multiplicative factor of two to include in Eq. (69) if we only integrate over the two degenerate Γ point branches for $T \to 0$.

Equation (69) is evaluated in Appendix E to yield the magnetic heat capacity per mole of spins at low temperatures due to the spin waves as

$$C_{\text{mag}} = \left(\frac{4\pi^2 R k_{\text{B}}^3 V_{\text{spin}}}{15\hbar^3 v_x v_y v_z}\right) T^3 \quad (T \ll T_{\text{N}}), \tag{73}$$

where R is the molar gas constant, V_{spin} is the volume per spin, and v_x, v_y, v_z are the spin wave velocities along the a, b, and c axes, respectively. This expression includes the contribution of the low-energy spin waves at the Brillouin zone corners and can be written in a form analogous to Eq. (63) for phonons as

$$C_{\text{mag}} = \beta_{\text{SW}} T^3, \quad \beta_{\text{SW}} = 2\left(\frac{2\pi^2 R k_{\text{B}}^3 V_{\text{spin}}}{15\hbar^3 v_x v_y v_z}\right). \tag{74}$$

By writing the Debye temperature in Eqs. (63) in terms of its constituent quantities,[31] one obtains the lattice heat capacity coefficient β_{D} per mole of atoms as

$$\beta_{\text{D}} = 3\left(\frac{2\pi^2 R k_{\text{B}}^3 V_{\text{atom}}}{15\hbar^3 v^3}\right), \tag{75}$$

where v is the sound wave speed, assumed isotropic, and V_{atom} is the volume per atom. This expression is similar to Eq. (74) except that the prefactor is three instead of two, due to the three sound wave polarization directions for each sound wave mode (two mutually perpendicular transverse polarizations and one longitudinal polarization), which are assumed to have the same wave speed v in the Debye model.

2. Application of the spin wave theory for the magnetic heat capacity to the J_1-J_2-J_c Heisenberg model and BaMn₂As₂

From the expressions for the spin wave velocities in the J_1-J_2-J_c model in Eq. (9), one has

$$v_x v_y v_z = v_{ab}^2 v_c$$
$$= \frac{4\sqrt{2}(J_1 S)^3 a^2 c}{\hbar^3}\left(1 + \frac{J_c}{2J_1}\right)^{3/2}\left(1 - \frac{2J_2}{J_1}\right)\sqrt{\frac{J_c}{J_1}}. \tag{76}$$

For BaMn₂As₂, there are two formula units, or four Mn atoms, per unit cell with volume $a^2 c$. The volume per spin is thus

$$V_{\text{spin}} = \frac{a^2 c}{4}. \tag{77}$$

Dividing Eq. (76) by Eq. (77) gives

$$\frac{v_x v_y v_z}{V_{\text{spin}}} = \frac{16\sqrt{2}(J_1 S)^3}{\hbar^3}\left(1 + \frac{J_c}{2J_1}\right)^{3/2}\left(1 - \frac{2J_2}{J_1}\right)\sqrt{\frac{J_c}{J_1}}. \tag{78}$$

Inserting Eq. (78) into (74) gives

$$\beta_{\text{SW}} = \frac{\pi^2 R}{60\sqrt{2}(J_1 S/k_{\text{B}})^3}$$
$$\times \left[\left(1 + \frac{J_c}{2J_1} \right)^{3/2} \left(1 - \frac{2J_2}{J_1} \right) \sqrt{\frac{J_c}{J_1}} \right]^{-1}. \quad (79)$$

From Table II, the exchange constants from the neutron data are $J_1 S/k_{\text{B}} = 380$ K, $J_2/J_1 = 0.29$ and $J_c/J_1 = 0.09$. Inserting these values into Eq. (79) gives the calculated value

$$\beta_{\text{SW}} = 0.13 \text{ mJ/mol spins K}^4 \quad \text{for} \quad \text{BaMn}_2\text{As}_2. \quad (80)$$

From Eq. (63), the observed β value per mole of Mn spins is 0.325 mJ/mol spins K^4. The calculated β_{SW} value is thus 40% of the measured value, so the observed β value contains a significant magnetic contribution if the anisotropy gap in the spin wave spectrum is negligible. However, an anisotropy gap would reduce the spin wave contribution to the heat capacity to exponentially small values at low temperatures.

IX. MONTE CARLO SIMULATIONS OF THE MAGNETIC SUSCEPTIBILITY AND MAGNETIC HEAT CAPACITY IN THE J_1-J_2-J_c MODEL

Both our classical and quantum Monte Carlo simulations were carried out within the framework of the J_1-J_2-J_c Heisenberg model introduced above in Sec. III. We have calculated the magnetic heat capacity and magnetic spin susceptibility versus temperature for various size lattices of quantum spins $S = 1/2, 1, 3/2, 2,$ and $5/2$ and for the classical model. We first motivate the scaling of the axes of our theoretical plots of $\chi(T)$, remark on the temperature regime over which this scaling is expected to hold, and then present our Monte Carlo simulation results. Then we compare our predictions for the magnetic susceptibility with the experimental susceptibility data for BaMn$_2$As$_2$ above T_{N} in Fig. 7 to obtain additional estimates of the exchange constants in this compound.

A. Scaling of the theoretical $\chi(T)$ axes

Using Eqs. (23) and (25) in the Heisenberg "J model" for a bipartite spin lattice with equal NN exchange, the Curie-Weiss law (22) can be rewritten as

$$\frac{\chi J}{N g^2 \mu_{\text{B}}^2} = \frac{1}{\frac{3k_{\text{B}}T}{JS(S+1)} + z}. \quad (81)$$

The quantity on the left-hand side of Eq. (81) is the theorist's definition of "χ", which is the susceptibility per spin, in units of $1/J$, with $g\mu_{\text{B}}$ set equal to 1. On the right-hand side, we see that if we use a temperature scale defined by $k_{\text{B}}T/[JS(S+1)]$, then all spin lattices with the same coordination number z but with different J and/or S will all follow the same universal curve at high temperatures. Therefore, in this paper we scale the calculated susceptibilities when $J_2, J_c = 0$ as

$$\frac{\chi J_1}{N g^2 \mu_{\text{B}}^2} \quad \text{versus} \quad \frac{k_{\text{B}}T}{J_1 S(S+1)}. \quad (82)$$

This is the same scaling of the temperature axis as for the magnetic heat capacity in Eq. (A10).

In the J_1-J_2-J_c model, according to Fig. 2 there are four in-plane next-nearest-neighbor interactions

$$J_2 = \alpha J_1, \quad (83)$$

two NN interactions along the c axis

$$J_c = \gamma J_1, \quad (84)$$

in addition to the $z_1 = 4 \equiv z$ nearest-neighbor interactions J_1. When these additional interactions are present, according to Eq. (26) the Weiss temperature becomes

$$\theta = \frac{z J_1 (1 + \alpha + \gamma/2) S(S+1)}{3k_{\text{B}}}, \quad (85)$$

and the form of the new Curie-Weiss law corresponding to Eq. (81) is

$$\frac{\chi J_1 (1 + \alpha + \gamma/2)}{N g^2 \mu_{\text{B}}^2} = \frac{1}{\frac{3k_{\text{B}}T}{J_1(1+\alpha+\gamma/2)S(S+1)} + z}. \quad (86)$$

A more accurate high-temperature scaling is obtained in this case by replacing J_1 in Eq. (82) by $J_1 + J_2 + J_c/2 = J_1(1 + \alpha + \gamma/2)$ and scaling the data according to

$$\frac{\chi J_1 (1 + \alpha + \gamma/2)}{N g^2 \mu_{\text{B}}^2} \quad \text{versus} \quad \frac{k_{\text{B}}T}{J_1(1 + \alpha + \gamma/2)S(S+1)}. \quad (87)$$

The scalings in Eqs. (82) and (87) are expected to be universal with respect to the spin and the exchange constants only at "high" temperatures. Appendix A shows that the calculations begin to deviate from the Curie-Weiss behavior when $1/T^2$ and higher order terms in the two-spin correlation functions become significant compared to the $1/T$ terms with decreasing T.

B. Classical Monte Carlo simulations

The classical Monte Carlo (CMC) simulations were performed on periodic $L \times L$ clusters for $J_c = 0$ and for $L \times L \times L_c$ clusters for $J_c \neq 0$ using a hybrid algorithm that combines Metropolis and over-relaxation sweeps.[41] In order to obtain statistically reliable data we have generated $\sim 10^5$ configurations at each temperature and then averaged the results over 50 independent annealing runs.

The spin Hamiltonian for our classical Monte Carlo simulations is the classical analogue of the quantum spin Hamiltonian (2), given by

$$\mathcal{H}_{\text{classical}} = J_1 S^2 \sum_{\langle ij \rangle} \hat{\mathbf{S}}_i \cdot \hat{\mathbf{S}}_j + J_2 S^2 \sum_{\langle ik \rangle} \hat{\mathbf{S}}_i \cdot \hat{\mathbf{S}}_k$$
$$+ J_c S^2 \sum_{\langle il \rangle} \hat{\mathbf{S}}_i \cdot \hat{\mathbf{S}}_k + g\mu_{\text{B}} H \sum_i S_i^z, \quad (88)$$

where S is the magnitude of the spin, $\hat{\mathbf{S}}$ is a classical spin unit vector, and $\hat{\mathbf{S}}_i \cdot \hat{\mathbf{S}}_k = \cos\theta_{ij}$. According to Eq. (88), the exchange parameters J_α are always combined with the classical spin magnitude S in the combination $J_\alpha S^2$.

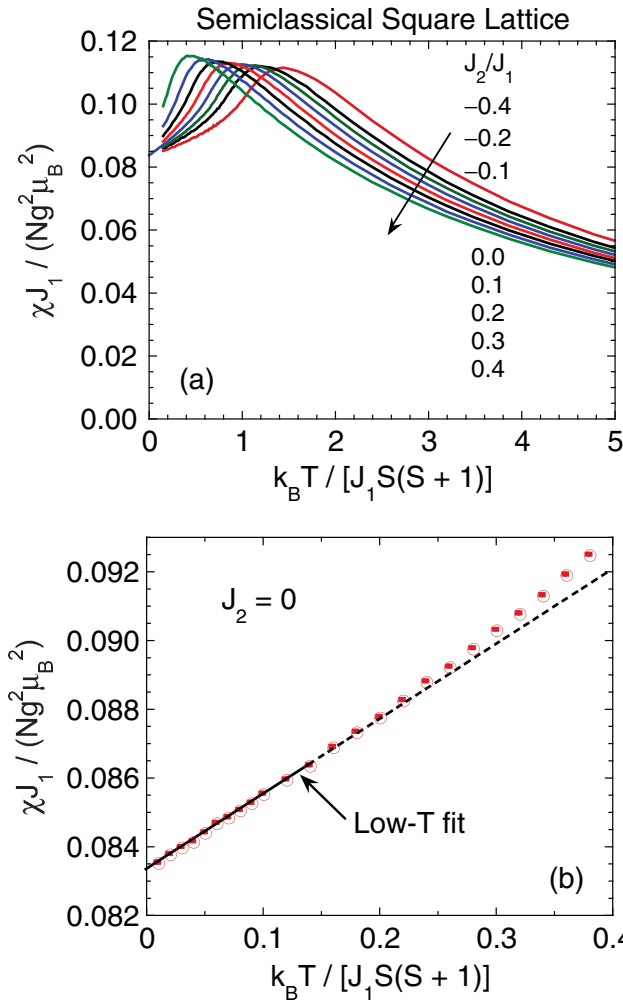In the following, we first consider our simulations for $J_c = 0$ and then for $J_c \neq 0$.

FIG. 17. (Color online) (a) Normalized magnetic spin susceptibility $\chi J_1/(Ng^2\mu_B^2)$ versus normalized temperature $k_BT/[J_1S(S+1)]$ for the classical spin S Heisenberg square lattice with $J_c = 0$ and $J_2/J_1 = -0.4$ to 0.4, with $S(S+1)$ replacing S^2. The lattice size is 80×80 in each case. (b) Expanded plot at low temperatures (open circles) of the data for $J_2 = 0$ in (a). The error bars are shown and are inside the open circles. A linear fit to the data up to a reduced temperature of 0.14 is shown as the solid straight line, and the dashed line is an extrapolation of the fit. The coefficients of the fit are listed in Eq. (89).

1. $J_c = 0$

The semiclassical magnetic spin susceptibilities χ versus T for the square lattice calculated using CMC simulations on 80×80 spin lattices are shown in Fig. 17(a) for $J_c = 0$ and $J_2/J_1 = -0.4$ to 0.4. Here, the term "semiclassical" means that S^2 in the final result of the classical simulations is replaced by the quantum mechanical expectation value $\langle S^2 \rangle = S(S+1)$. This replacement allows the classical simulations to merge smoothly with the quantum Monte Carlo simulations (see Fig. 23 below). We carried out simulations of various other $L \times L$ lattice sizes with $L = 10$–100 for $J_2/J_1 = 0$ and 0.2 and found that finite-size corrections to both the calculated magnetic susceptibility and magnetic heat capacity are negligible for $L \geqslant 50$.
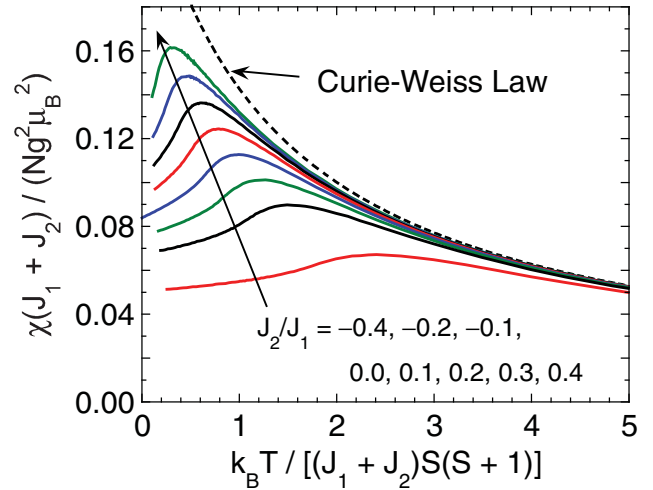

FIG. 18. (Color online) Normalized magnetic spin susceptibility $\chi(J_1 + J_1)/(Ng^2\mu_B^2)$ versus normalized temperature $k_BT/[(J_1 + J_2)S(S+1)]$ determined from classical Monte Carlo simulations for the spin S Heisenberg square lattice with $J_c = 0$ and $J_2/J_1 = -0.4$ to 0.4, as indicated, with $S(S+1)$ replacing the classical S^2. The lattice size is 80×80 in each case. The axis scaling is superior at high temperatures to that in Fig. 17(a). A plot of the Curie-Weiss law in Eq. (86) is shown by the black dashed curve.

The $\chi(T)$ data in Fig. 17(a) show two interesting trends. First, at high temperatures the Curie-Weiss law $C/(T+\theta)$ is obtained, in which the (positive) Weiss temperature θ is proportional to the sum of all interactions of a given spin with its neighbors according to Eq. (26). Thus, for a negative (ferromagnetic) J_2 that partially cancels the positive J_1, the susceptibility increases at a fixed T, and for a positive J_2 it decreases. Second, at low temperatures this trend is reversed. A negative ferromagnetic J_2 is nonfrustrating with respect to J_1 and reinforces the short-range ordering that causes the peak in $\chi(T)$. This moves the peak up in temperature and suppresses the susceptibility in the short-range ordered state at low temperatures below the peak temperature. The opposite behavior is found for a positive AF J_2 which is frustrating with respect to J_1. This J_2 suppresses the short-range AF ordering, which decreases the peak temperature and increases the susceptibility below the peak temperature compared to the case when $J_2 = 0$.

These trends are illustrated in a different way if the best high-temperature scaling for these plots, given in Eq. (87), is used, as shown in Fig. 18. In addition, the Curie-Weiss law from Eq. (86) is plotted in Fig. 18 as the blue dashed line. From a comparison of the simulation data with the Curie-Weiss prediction, one sees that the two-spin correlations higher order than present in the Curie-Weiss regime ($\sim 1/T$) begin to become observable on the scale of the figure for $T \lesssim 5(J_1/k_B)S(S+1)$. According to Eq. (85), this latter value is about four times the Weiss temperature θ, which has the value 4/3 on the horizontal scale in Fig. 18.

The data in Fig. 17(a) for $J_2 = 0$ were obtained down to a reduced temperature of 0.01, as shown in the expanded plot in Fig. 17(b). The lowest temperature data are linear in T. A
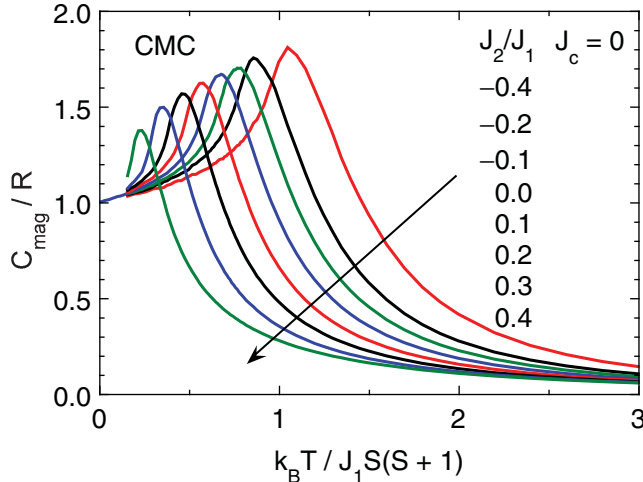
FIG. 19. (Color online) Classical Monte Carlo (CMC) simulations on 80×80 spin lattices of the magnetic heat capacity C_{mag} divided by the molar gas constant R versus the scaled temperature $k_B T / J_1 S(S+1)$ for $J_c = 0$ and $J_2/J_1 = -0.4$ to 0.4 as shown.

linear fit yielded

$$\frac{\chi J_1}{N g^2 \mu_B^2} = 0.083\,33(2) + 0.0218(3) \frac{k_B T}{J_1 S(S+1)}, \quad (89)$$

as shown by the solid line in Fig. 17(b). According to Takahashi's modified spin wave theory for the AF square lattice, the classical limit (A9) in Ref. 42 reads

$$\frac{\chi J_1}{N g^2 \mu_B^2} = \frac{1}{12} + \frac{1}{24\pi} \frac{k_B T}{J_1 S^2} + \mathcal{O}(T^3). \quad (90)$$

The zero-temperature reduced susceptibility $1/12 \approx 0.083\,33$ in Eq. (90) is the same as our value in Eq. (89) to within the errors of our Monte Carlo data, but the theoretical initial slope $1/(24\pi) \approx 0.013\,26$ is too small compared to our Monte Carlo value in Eq. (89). On the other hand, in a $1/D$ expansion where D is the dimensionality of the spins ($D = 3$ here), for the classical square spin lattice at low T Hinzke *et al.*[43] obtained

$$\frac{\chi J_1}{N g^2 \mu_B^2} = \frac{1}{12} + \frac{1}{32} \frac{k_B T}{J_1 S^2}. \quad (91)$$

The zero temperature susceptibility is the same as our and Takahashi's value but Hinzke *et al.*'s initial slope is $1/32 = 0.031\,25$, which this time is larger than our Monte Carlo value in Eq. (89). Thus, our value of the initial slope is bracketed by the predictions of the modified spin wave theory and the $1/D$ expansion.

The magnetic heat capacity is plotted in Fig. 19 according to Eq. (A10) versus the scaled temperature for exchange constant ratios $J_2/J_1 = -0.4$ to 0.4 on 80×80 spin lattices. The broad peaks in the curves decrease in temperature with increasing J_2. This is understandable in terms of the enhancement of short-range AF order for ferromagnetic (negative) J_2, which increases the temperature of the peak, and the frustration effect for antiferromagnetic (positive) J_2, which decreases the temperature of the peak. The peak values and the temperatures at which they occur are listed in Table V. It is interesting that the variation in $C_{\text{mag}}(T)$ with J_2 depends on the sign of J_2, in

TABLE V. Parameters obtained from semiclassical (SC) Monte Carlo and quantum Monte Carlo simulations of the magnetic heat capacity $C_{\text{mag}}(T)$ for the square lattice with no interlayer coupling ($J_c = 0$). Here $C_{\text{mag}}^{\text{max}}$ is the value of C_{mag} at a magnetic ordering peak, T^{max} is the temperature at which the maximum occurs, and SC means we have replaced S^2 with $S(S+1)$ in the temperature scaling of the classical Monte Carlo data. Note that the value of T^{max} is different than the temperature of the maximum in the magnetic susceptibility.

S	Lattice size	J_2/J_1	$\dfrac{C_{\text{mag}}^{\text{max}}}{R}$	$\dfrac{k_B T^{\text{max}}}{J_1 S(S+1)}$
1/2	32×32	0	0.4606(7)	0.801(2)
1	32×32	0	0.885(2)	0.690(4)
	64×64	0	0.879(2)	0.700(3)
3/2	32×32	0	1.159(2)	0.674(1)
2	32×32	0	1.325(2)	0.673(1)
	64×64	0	1.295(2)	0.684(2)
5/2	32×32	0	1.428(2)	0.673(2)
SC	80×80	-0.4	1.801(5)	1.055(3)
SC	80×80	-0.2	1.752(3)	0.861(3)
SC	80×80	-0.1	1.699(1)	0.777(2)
SC	80×80	0	1.666(1)	0.678(1)
SC	80×80	0.1	1.621(2)	0.575(1)
SC	80×80	0.2	1.567(2)	0.471(2)
SC	80×80	0.3	1.498(3)	0.352(3)
SC	80×80	0.4	1.378(3)	0.232(2)

contrast with expectation from the first term in the HTSE in Eq. (A9) in which the uniform J appears as the square and is hence independent of the sign. Thus, one cannot replace zJ^2 in Eq. (A9) with $\sum_j J_{ij}^2$. This constraint is not present when calculating the Weiss temperature in the Curie-Weiss law from Eq. (26), in which one includes the interactions of a given spin with all of its neighbors algebraically and on the same footing.

2. $J_c \neq 0$

The classical Monte Carlo simulations do not produce the same results as the molecular field theory does because the interaction between a spin and its neighbors is not approximated by the interaction of the spin with the *average* spin of its neighbors as in the molecular field theory. In particular, according to the Mermin-Wagner theorem,[44] a Heisenberg spin system in one or two dimensions, as in the J_1-J_2 model with only intraplanar exchanges, should not show long-range magnetic ordering at finite temperature. This theorem is respected in our classical simulations, but not in molecular field theory. On the other hand, when the simulations are carried out with $J_c \neq 0$, we find that long-range AF ordering does occur, as expected. Because a uniform magnetic field does not directly couple to the AF order parameter [the staggered moment, see Eq. (B16)], these AF phase transitions have rather subtle effects on the calculated uniform susceptibility. They are much more clearly manifested in the magnetic heat capacity which we also present and would also be clearly delineated in calculations of the staggered susceptibility in which the applied magnetic field has opposite directions for the two sublattices.

Throughout this section, we replace the classical variable S^2 with its quantum-mechanical counterpart $S(S+1)$. We show
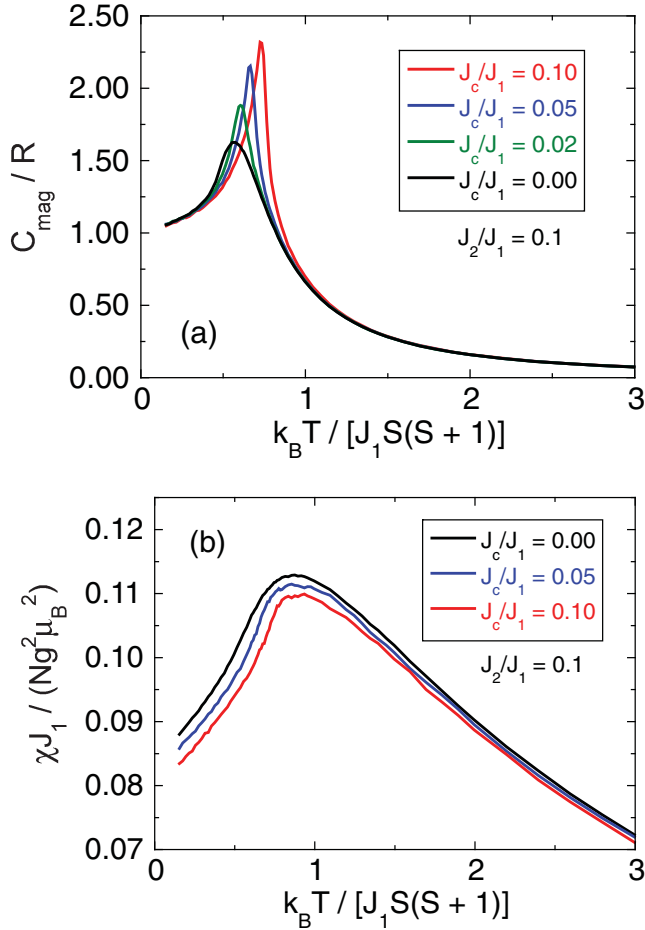
FIG. 20. (Color online) (a) Magnetic heat capacity and (b) magnetic susceptibility χ versus temperature T from classical Monte Carlo simulations for the spin S Heisenberg square lattice with $J_2/J_1 = 0.1$ and with $J_c/J_1 = 0, 0.02, 0.05,$ and 0.1, as indicated. The order of the curves from top to bottom is the same as in the respective figure legends. The lattice size in each case is $20 \times 20 \times 10$.
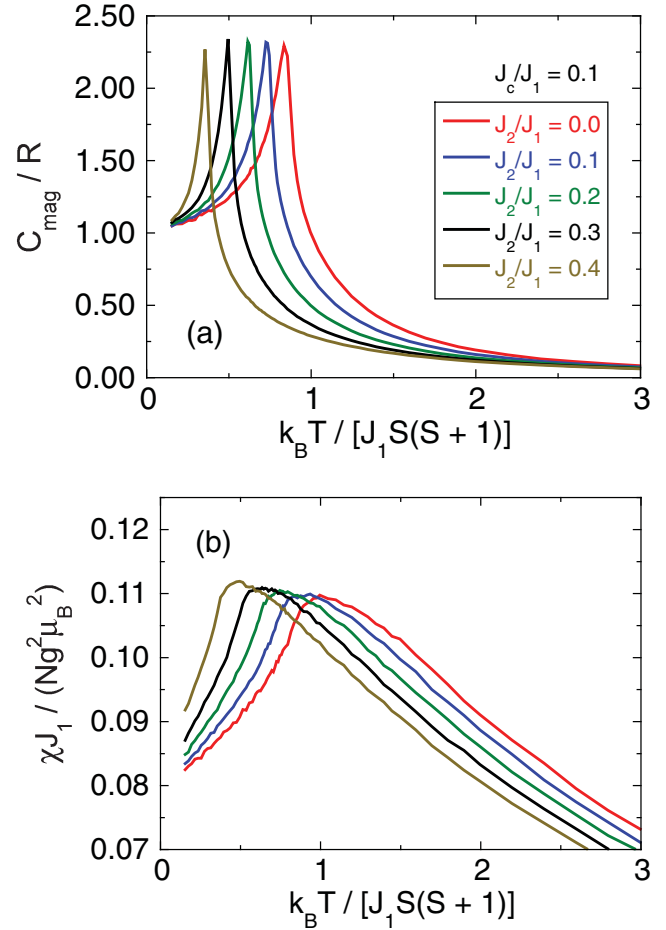

FIG. 21. (Color online) (a) Magnetic heat capacity C_{mag} and (b) spherically averaged magnetic susceptibility χ versus temperature T from classical Monte Carlo simulations for the spin S Heisenberg square lattice with $J_2/J_1 = 0$ to 0.4, as indicated, and with fixed $J_c/J_1 = 0.1$. The order of the curves from right to left is given in the figure (a) legend. The lattice size in each case is $20 \times 20 \times 10$.

our results in two formats. First, in Fig. 20 are shown the magnetic heat capacity C_{mag} and the spherically averaged magnetic susceptibility χ versus temperature T for fixed $J_2/J_1 = 0.1$ and variable $J_c = 0, 0.02, 0.05,$ and 0.1, where J_1, J_2, and J_c are all antiferromagnetic. From Fig. 20(a), one sees that $C_{\mathrm{mag}}(T)$ for $J_c = 0$ just shows a broad peak characteristic of short-range AF order. However, the C_{mag} quickly and clearly shows a cusplike behavior with increasing J_c at temperatures T_{N} corresponding to long-range AF order. Second, in Fig. 21 are shown $C_{\mathrm{mag}}(T)$ and $\chi(T)$ for fixed $J_c/J_1 = 0.1$ and variable $J_2/J_1 = 0–0.4$, where J_1, J_2, and J_c are again all antiferromagnetic. For all combinations of J_2/J_1 and J_c/J_1 we have studied, to within the errors the peak in C_{mag} at T_{N} coincides in temperature with the peak in $d(\chi T)/dT$ on the low-T side of the broad peak in $\chi(T)$, in agreement with the Fisher relation.[32] We note that the T_{N} and shape/magnitude of C_{mag} at T_{N} determined in our simulations may be affected by finite size effects.

The temperatures T_{N} of the peaks in $C_{\mathrm{mag}}(T)$ and the values of $C_{\mathrm{mag}}(T_{\mathrm{N}})$ at the peak, versus the exchange constant ratios J_2/J_1 and J_c/J_1, are listed in Table VI and plotted in Figs. 22(a)

and 22(b). For $J_2 = 0$, our T_{N} values are lower by $\lesssim 1\%$ than the values obtained by Yasuda *et al.* for $J_c/J_1 = 0.02, 0.05,$ and 0.1.[45] For $J_2 = 0$, a good fit to T_{N} versus J_c for various spin values was obtained in Ref. 46 using the expression[45]

$$\frac{k_{\mathrm{B}}T_{\mathrm{N}}}{J_1 S(S+1)} = \frac{A}{B - \ln(J_c/J_1)}, \tag{92}$$

where different values of the constants A and B were required for different spin values. We fitted the classical Monte Carlo data for $J_2 = 0$ in Fig. 22(a) using Eq. (92) and obtained a good fit with the values

$$A = 7.70, \quad B = 6.87, \tag{93}$$

which are both about a factor of two larger than the respective values $A = 3.96$ and $B = 3.01$ obtained in Ref. 46 for the classical limit $S = \infty$. The fit is shown as the solid red curve for $J_2/J_1 = 0$ in Fig. 22(a).

From Fig. 22(a), a positive antiferromagnetic J_2 frustrates the G-type AF ordering and depresses T_{N} approximately linearly with J_2, and the T_{N} for each J_c value extrapolates to zero at $J_2/J_1 \approx 0.6$, which is close to the value of 0.5

TABLE VI. Temperatures T_N of the magnetic ordering peaks in the molar magnetic heat capacity C_{mag} and the values of $C_{mag}(T_N)$ at the peak, versus the exchange constant ratios J_2/J_1 and J_c/J_1, obtained from classical Monte Carlo simulations. The T_N and C_{mag} values may be affected by finite size effects. Here R is the molar gas constant.

J_2/J_1	J_c/J_1	$k_B T_N/[J_1 S(S+1)]$	$C_{mag}(T_N)/R$
0	0.02	0.717(2)	1.890(3)
	0.05	0.773(1)	2.139(5)
	0.10	0.842(1)	2.29(2)
0.1	0.02	0.611(1)	1.879(4)
	0.05	0.667(1)	2.151(6)
	0.10	0.735(1)	2.318(5)
0.12	0.06	0.661(1)	2.190(6)
0.2	0.02	0.502(1)	1.880(8)
	0.05	0.557(1)	2.14(1)
	0.10	0.619(1)	2.32(1)
0.3	0.02	0.390(1)	1.839(2)
	0.05	0.439(1)	2.125(9)
	0.10	0.497(1)	2.343(7)
0.4	0.02	0.263(1)	1.784(8)
	0.05	0.313(1)	2.06(1)
	0.10	0.360(1)	2.26(1)

from Eq. (4) at which one classically expects the G-type AF order to become unstable with respect to the stripe-AF order. Therefore, we fitted the dependence of T_N on J_2/J_1 of all the data for $J_c/J_1 = 0.02$, 0.05, and 0.1 together using the expression

$$\frac{T_N(J_c, J_2)}{T_N(J_c, J_2 = 0)} = 1 - \left(\frac{J_2/J_1}{R_1}\right)^{R_2} \quad (94)$$

(not shown) and obtained the values

$$R_1 = 0.644, \quad R_2 = 1.082. \quad (95)$$

The fits are shown as the solid curves in Fig. 22(b). Thus, the global function to fit all of our $T_N(J_c/J_1, J_2/J_1)$ data is

$$\frac{k_B T_N}{J_1 S(S+1)} = \frac{A}{B - \ln(J_c/J_1)} \left[1 - \left(\frac{J_2/J_1}{R_1}\right)^{R_2}\right]. \quad (96)$$

The fits for T_N versus J_c at fixed $J_2/J_1 = 0.1$–0.4 are shown as the solid curves in Fig. 22(a). We see that Eq. (96), together with the four parameters in Eqs. (93) and (95), provide a good global fit to all 15 $T_N(J_c/J_1, J_2/J_1)$ data points in Fig. 22(a) from our CMC simulations.

C. Quantum Monte Carlo simulations

1. Magnetic susceptibility

Our quantum Monte Carlo (QMC) simulations were carried out with the ALPS[47,48] directed loop application[49] in the stochastic series expansion framework[50] using version ALPS 1.3. Up to about 1×10^9 sweeps were carried out for the 32×32 lattice and the sign-free situation $J_2 = 0$. In order to compensate for the sign problem introduced by $J_2 > 0$ this was increased to about 2×10^{11} sweeps on the 6×6 lattice for $J_2 = 0.1$. QMC simulations have been previously reported for
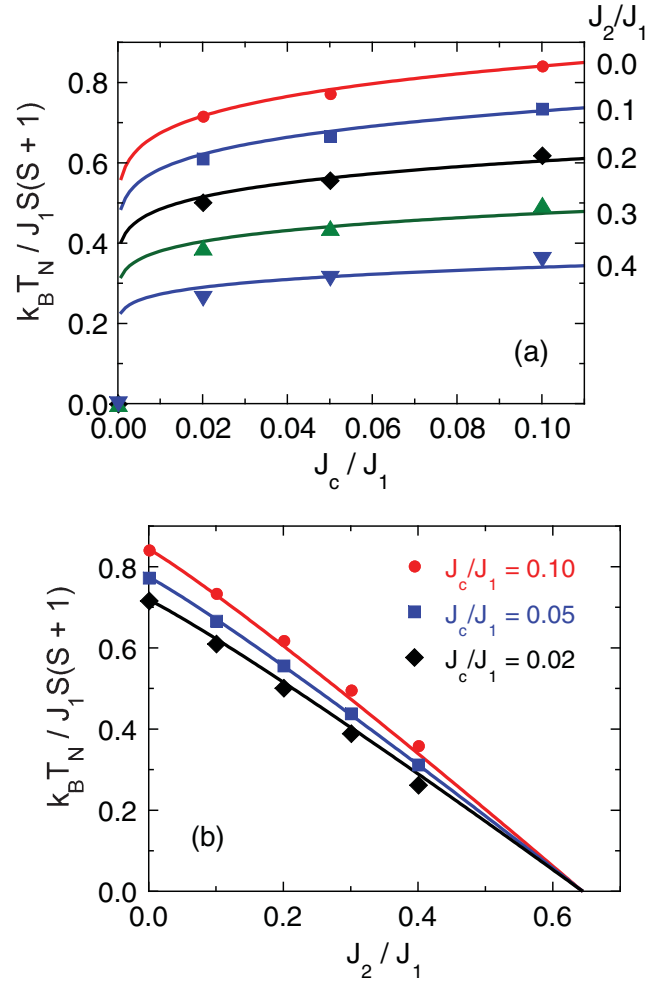

FIG. 22. (Color online) Antiferromagnetic ordering temperature T_N versus (a) the interlayer coupling J_c for fixed values of J_2/J_1 and (b) J_2/J_1 at fixed J_c/J_1. In (b), the order of the curves from top to bottom is the same as in the figure legend. The solid curves are a global fit to all the data by Eq. (96), using the parameters in Eqs. (93) and (95).

$S = 1$ over the temperature range $0.5 \leqslant k_B T/J_1 S(S+1) \leqslant 5$ by Harada *et al.*[51] We have extended these simulations to much lower temperatures (see Fig. 24).

Our QMC simulations of the magnetic spin susceptibilities versus temperature for the square lattice with quantum spins $1/2$ to $5/2$ with $J_2 = 0$ are shown in Fig. 23(a), and for $J_2/J_1 = 0.1$ and $S = 2$ and $5/2$ in Fig. 23(b). Various parameters obtained from these and the above semiclassical data are listed in Table VII as described in the caption. We checked by comparison of the data for the 32×32 lattice with 64×64 lattice data for $S = 1$ and $S = 2$ (see Table VII) that the 32×32 lattice data in Figs. 23 and 24 (below) are close to the thermodynamic limit; that is, finite size effects are smaller than the size of the symbols (except probably the lowest temperature datum for $S = 1/2$ in Fig. 24).

Hasenfratz and Niedermayer obtained the low-temperature limit of the spin susceptibility of the Heisenberg antiferromagnet on a square lattice from chiral perturbation theory, given
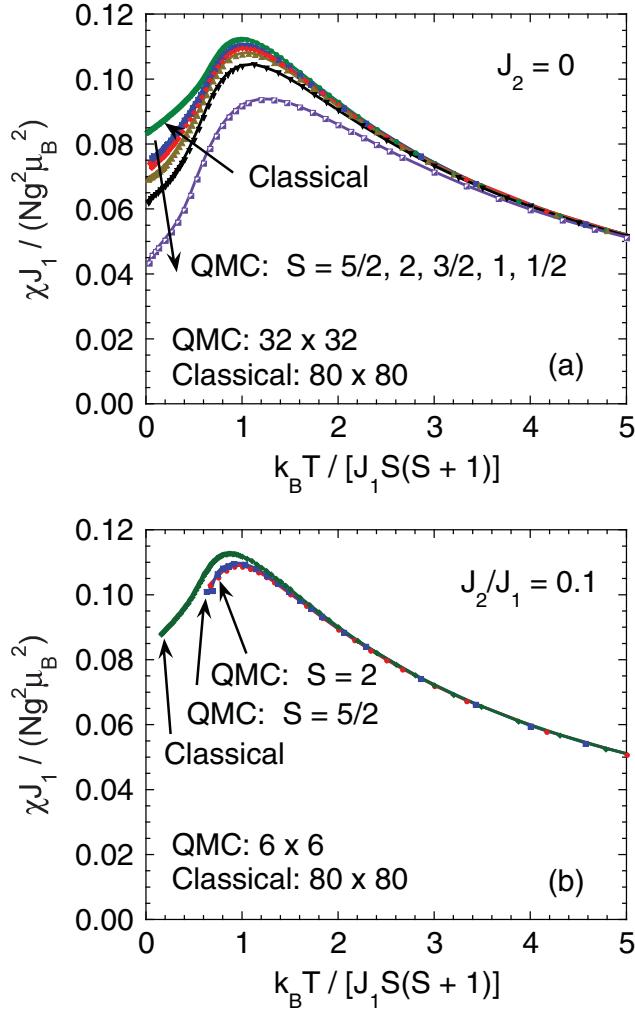
FIG. 23. (Color online) Normalized magnetic spin susceptibility $\chi J_1/(Ng^2\mu_B^2)$ versus normalized temperature $k_B T/[J_1 S(S+1)]$ determined from quantum Monte Carlo (QMC) simulations for quantum Heisenberg square lattices with (a) $J_2/J_1 = 0$ and spins $S = 5/2$, 2, 3/2, 1, and 1/2, and (b) $J_2/J_1 = 0.1$ and spins $S = 5/2$ and 2. The data for the semiclassical model (green) with $J_2/J_1 = 0$ and 0.1 are included in the two panels, respectively. The lattice size for each simulation is indicated in the respective figure.

by[52]

$$\chi(T) = \frac{2\chi_\perp(0)}{3}\left[1 + \left(\frac{k_B T}{2\pi\rho_S}\right) + \left(\frac{k_B T}{2\pi\rho_S}\right)^2 + \cdots\right], \quad (97)$$

where ρ_S is the spin wave stiffness, $\chi_\perp(0)$ is the zero-temperature perpendicular susceptibility given by

$$\frac{\chi_\perp(0) J_1}{Ng^2\mu_B^2} = \frac{\rho_S J_1 a^2}{(\hbar c)^2}, \quad (98)$$

c is the spin wave velocity, and a is the square lattice parameter. The $\chi_\perp(0)$ and ρ_S depend on the spin S and were calculated using spin wave theory (SWT) by Hamer *et al.* as[53]

$$\frac{\chi_\perp(0) J_1}{Ng^2\mu_B^2} = \frac{1}{8} - \frac{0.034\,446\,959\,42}{S}$$

$$+ \frac{0.002\,040\,06(7)}{S^2} + \mathcal{O}(S^{-3}) \quad (99)$$
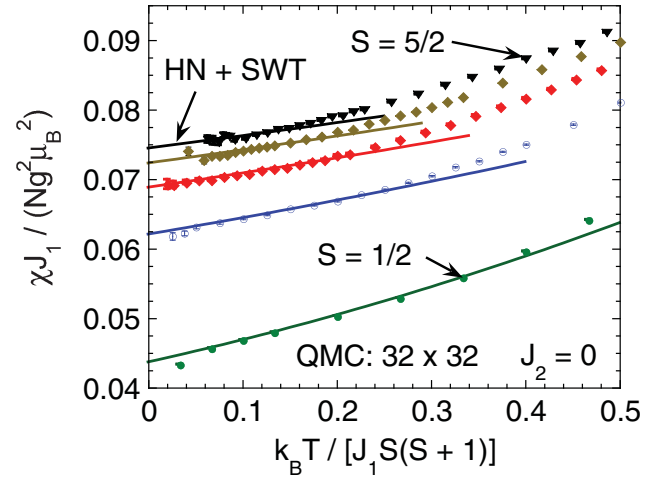

FIG. 24. (Color online) Normalized QMC magnetic spin susceptibility $\chi J_1/(Ng^2\mu_B^2)$ versus normalized temperature $k_B T/[J_1 S(S + 1)]$ data (symbols) at low temperatures from Fig. 23(a) for spins $S = 1/2$ (bottom), 1, 3/2, 2, and 5/2 (top). The error bars for the QMC data are also plotted. The corresponding Hasenfratz-Niedermayer + spin wave theory predictions (HN + SWT) for the low-temperature behaviors (Refs. 52 and 53) are also shown for these spin values as solid curves.

and

$$\frac{\rho_S}{J_1} = S^2 - 0.117\,628\,254\,4\,S - 0.010\,207\,987\,3$$

$$- \frac{0.003\,16(2)}{S} + \mathcal{O}(S^{-2}). \quad (100)$$

The low-temperature QMC data from Fig. 23(a) are shown in Fig. 24 together with the above predictions of Hasenfratz and Niedermayer (HN) combined with the SWT results of Hamer *et al.* The lowest-temperature QMC data for spins 1/2 to 5/2 in Fig. 24 are all seen to be in good agreement with the HN + SWT predictions. High-resolution calculations of $\chi(T)$ from the literature for the $S = 1/2$ square lattice Heisenberg antiferromagnet also confirm the form of Eq. (97).[54,55] For $S = 1$ our value of $\chi(0)$ from Fig. 24 disagrees with the value 0.071 97 given in Ref. 46. It was claimed in Ref. 42 that on the basis of spin wave theory, the next-order term above the T^1 term in Eq. (97) is $\mathcal{O}(T^3)$, as in Eq. (90) above, in disagreement with Eq. (97). However, the next higher order term is indeed the T^2 term.[56]

2. Magnetic heat capacity

The magnetic heat capacity C_{mag} versus temperature data from our QMC simulations for the square lattice with only NN interactions ($J_2 = J_c = 0$) are shown in Fig. 25 for spins $S = 1/2$, 1, 3/2, 2, and 5/2. Also shown for comparison are our CMC heat capacity data for $J_2 = J_c = 0$ from Fig. 20(a) and the first term in the HTSE $C_{\mathrm{mag}} \propto 1/T^2$ for the magnetic heat capacity from Eq. (A9) using the nearest-neighbor coordination number $z = 4$. The CMC and QMC data exhibit this HTSE behavior for temperatures $T \gtrsim 2J_1 S(S+1)/k_B$. The values of the heat capacities of the peaks in the simulation data for the spin values $S = 1$ to $S = 5/2$

TABLE VII. Calculated values of (i) the maximum spin susceptibilities χ^{max} and (ii) the temperatures T^{max} at which they occur for different lattice sizes, J_2/J_1 values, and quantum and semiclassical S values; (iii) the product $\chi^{\mathrm{max}}T^{\mathrm{max}}/3C$ where C is the Curie constant per mole of spins in Eq. (23); (iv) the value of the product $\chi^{\mathrm{max}}T^{\mathrm{max}}$ for the listed S assuming $g = 2$; and (v) the value of the product for an alternate semiclassical value of $S = 5/2$ assuming $g = 2$. By "semiclassical" (SC) is meant that S^2 in the final result of the classical calculation is replaced by the quantum mechanical expectation value $\langle S^2 \rangle = S(S + 1)$. In the last column is listed the molecular field Néel temperature T_{N}, normalized by $J_1 S(S + 1)/k_{\mathrm{B}}$, according to Eq. (41).

S	Lattice size	J_2/J_1	J_c/J_1	$\dfrac{\chi^{\mathrm{max}} J_1}{N g^2 \mu_{\mathrm{B}}^2}$	$\dfrac{k_{\mathrm{B}} T^{\mathrm{max}}}{J_1 S(S+1)}$	$\dfrac{\chi^{\mathrm{max}} T^{\mathrm{max}}}{3C}$	$\chi^{\mathrm{max}} T^{\mathrm{max}}$ (cm^3 K/mol)	$\chi^{\mathrm{max}} T^{\mathrm{max}}$ (cm^3 K/mol)	$\dfrac{k_{\mathrm{B}} T_{\mathrm{N}}}{J_1 S(S+1)}$
1/2	32×32	0	0	0.09370(3)	1.248(3)	0.1169(3)	0.1316(4)		1.33
1	32×32	0	0	0.10438(5)	1.090(3)	0.1138(3)	0.3415(11)		1.33
	64×64	0	0	0.10424(3)	1.085(3)	0.1131(4)	0.3394(11)		
3/2	32×32	0	0	0.10790(3)	1.050(4)	0.1133(5)	0.638(3)		1.33
2	32×32	0	0	0.10952(4)	1.030(4)	0.1128(5)	1.016(4)		1.33
	64×64	0	0	0.10957(6)	1.038(5)	0.1137(6)	1.024(6)		
5/2	32×32	0	0	0.11040(3)	1.018(3)	0.1144(8)	1.50(1)		1.33
2	6×6	0.1	0	0.10882(6)	0.966(5)	0.1051(6)	0.946(6)		1.20
5/2	6×6	0.1	0	0.10966(6)	0.959(4)	0.1052(5)	1.381(6)		1.20
							$S = 2$	$S = 5/2$	
SC	80×80	-0.4	0	0.11115(5)	1.453(4)	0.1615(5)	1.454(5)	2.121(8)	1.87
SC	80×80	-0.2	0	0.11173(5)	1.225(4)	0.1369(5)	1.232(5)	1.797(8)	1.60
SC	80×80	-0.1	0	0.11210(4)	1.120(3)	0.1256(4)	1.130(4)	1.649(5)	1.47
SC	80×80	0	0	0.11235(3)	0.999(2)	0.1122(3)	1.011(3)	1.470(4)	1.33
SC	80×80	0.1	0	0.11274(3)	0.876(3)	0.0988(4)	0.889(3)	1.297(5)	1.20
SC	$20 \times 20 \times 10$	0.1	0.02	0.11216(6)	0.874(5)	0.0980(6)	0.883(6)	1.287(8)	1.21
SC	$20 \times 20 \times 10$	0.1	0.05	0.1113(1)	0.878(7)	0.0977(9)	0.880(8)	1.28(1)	1.23
SC	$20 \times 20 \times 10$	0.1	0.1	0.1098(1)	0.896(5)	0.0984(6)	0.886(6)	1.29(1)	1.27
SC	$20 \times 20 \times 10$	0.12	0.06	0.11126(8)	0.853(7)	0.0949(9)	0.854(8)	1.25(1)	1.21
SC	80×80	0.2	0	0.11325(2)	0.750(2)	0.0849(3)	0.765(2)	1.115(3)	1.07
SC	$20 \times 20 \times 10$	0.2	0.02	0.11275(5)	0.749(10)	0.0844(12)	0.76(1)	1.11(1)	1.08
SC	$20 \times 20 \times 10$	0.2	0.05	0.11187(10)	0.755(10)	0.0845(12)	0.76(1)	1.11(1)	1.10
SC	$20 \times 20 \times 10$	0.2	0.1	0.11029(5)	0.767(7)	0.0846(8)	0.762(7)	1.11(1)	1.13
SC	80×80	0.3	0	0.11391(3)	0.616(2)	0.0702(3)	0.632(3)	0.921(3)	0.93
SC	$20 \times 20 \times 10$	0.3	0.02	0.1134(10)	0.614(10)	0.070(1)	0.63(2)	0.91(3)	0.95
SC	$20 \times 20 \times 10$	0.3	0.05	0.11257(7)	0.627(7)	0.0706(8)	0.635(8)	0.93(1)	0.97
SC	$20 \times 20 \times 10$	0.3	0.1	0.1108(10)	0.652(7)	0.072(2)	0.65(1)	0.95(2)	1.00
SC	80×80	0.4	0	0.11509(4)	0.468(2)	0.0539(3)	0.485(2)	0.707(3)	0.80
SC	$20 \times 20 \times 10$	0.4	0.02	0.1147(10)	0.468(7)	0.054(2)	0.48(1)	0.70(2)	0.81
SC	$20 \times 20 \times 10$	0.4	0.05	0.1136(10)	0.467(10)	0.053(2)	0.48(1)	0.70(2)	0.83
SC	$20 \times 20 \times 10$	0.4	0.1	0.11175(5)	0.497(3)	0.0555(4)	0.500(3)	0.729(5)	0.87

and the temperatures at which they occur are listed in Table V above.

We checked finite-size effects associated with the QMC data by simulating C_{mag} for 64×64 $S = 1$ and $S = 2$ lattices for comparison with the 32×32 lattices in Fig. 25. On the scale of the figure, the 64×64 data (not shown) were close to the 32×32 lattice size data. For example, the peak heights differ by less than 2% between the simulations for the different size lattices (see Table V).

According to Eq. (41), the Néel temperature in MFT occurs in Fig. 25 at a value of $4/3$ on the horizontal scale and with a heat capacity jump on cooling below T_{N} given by Eq. (57) as $\Delta C_{\mathrm{mag}}/R = 3/2$ for $S = 1/2$ and $= 5/2$ for $S = \infty$. The data in Fig. 25 are very different from these MFT predictions due to the presence of short-range magnetic ordering and the lack of long-range magnetic ordering[44] in these two-dimensional spin lattices at finite temperatures.

The expression of Hasenfratz and Niedermayer for the low-temperature magnetic heat capacity of the Heisenberg antiferromagnet on a square lattice from chiral perturbation theory, per mole of spins, is[52]

$$C_{\mathrm{mag}} = \frac{6\,\zeta(3)R}{\pi(\hbar v/a)^2}(k_{\mathrm{B}}T)^2 + O(T^4), \tag{101}$$

where $\zeta(x)$ is the Riemann zeta function with $\zeta(3) \approx 1.202\,06$ and a is the length of an edge of the square lattice unit cell. The spin wave velocity v for the AF Heisenberg square lattice is[53,57]

$$\frac{\hbar v}{a} = 2\sqrt{2}SJ_1\left[1 + \frac{0.157\,947\,421}{2S} + \frac{0.021\,52}{(2S)^2} + O(S^{-3})\right]. \tag{102}$$
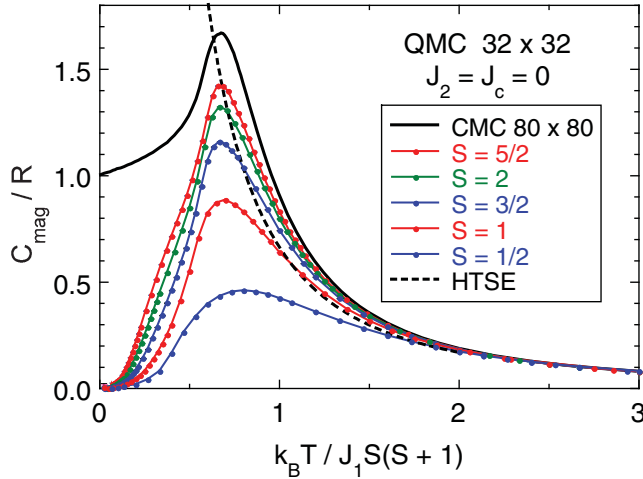
FIG. 25. (Color online) Magnetic heat capacity C_{mag} divided by the molar gas constant R versus normalized temperature $k_B T/[J_1 S(S+1)]$ for the square lattice with only nearest-neighbor couplings J_1 (exchange constants $J_2 = J_c = 0$). Quantum Monte Carlo (QMC) data (solid circles) for spins $S = 1/2$ (bottom), 1, 3/2, 2, and 5/2 (top) are shown, together with classical Monte Carlo (CMC) data from Fig. 20(a) (solid black curve at the top) and the first term in the high-temperature series expansion HTSE for the magnetic heat capacity from Eq. (A9) using $z = 4$ (dashed black curve). The error bars for the QMC data are also plotted, and the lines connecting the data points are guides for the eye. The order of the Monte Carlo data from top to bottom is the same as in the figure legend.

From Eqs. (101) and (102) one obtains

$$\frac{C_{mag}S^2}{R(k_B T/J_1)^2} = \frac{3\,\zeta(3)}{4\pi}\left[1 + \frac{0.157\,947\,421}{2S} + \frac{0.021\,52}{(2S)^2}\right]^{-2}$$
$$+ D(S)\left(\frac{k_B T}{J_1}\right)^2$$
$$\equiv A(S) + D(S)\left(\frac{k_B T}{J_1}\right)^2. \tag{103}$$

The factor $A(S)$ is 0.2063, 0.2441, 0.2578, 0.2649, and 0.2692 for $S = 1/2, 1, \ldots, 5/2$, respectively. Figure 26 shows our low-temperature $C_{mag}(T)$ data for $S = 1/2$, 1, and 3/2 plotted according to Eq. (103). The approximate extrapolated zero-temperature values are in accord with the above $A(S)$ values to within the data error bars. After setting $A(S)$ to the above respective fixed values, the initial slopes were estimated by fitting the data by Eq. (103), yielding $D(S) = 1.8$, 0.31, and 0.14 for $S = 1/2$, 1, and 3/2, respectively, as shown by the respective dotted lines in Fig. 26. The slope D decreases significantly with increasing S but remains positive from $S = 1/2$ up to $S = 3/2$. The sign of $D(S)$ was indeed predicted by Hofmann to be positive using the effective Lagrangian method.[58]

X. COMPARISON OF MONTE CARLO SIMULATIONS OF THE MAGNETIC PROPERTIES WITH EXPERIMENT

A. Néel temperature

Using Eq. (96), we can predict the Néel temperature from the values $J_1 S/k_B = 380$ K, $J_2/J_1 = 0.29$, and $J_c/J_1 = 0.09$
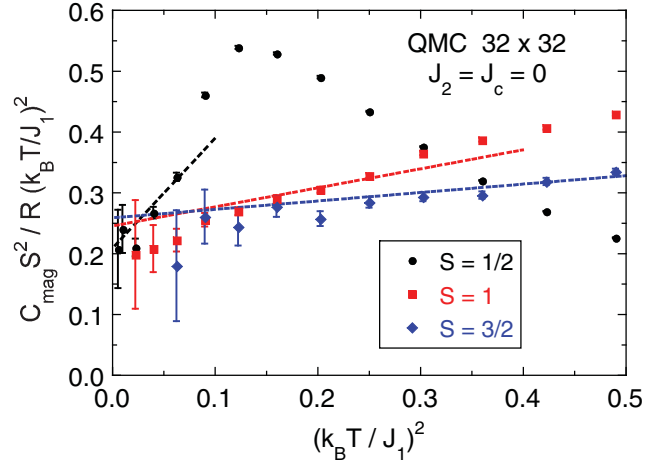

FIG. 26. (Color online) Low-temperature magnetic heat capacity C_{mag} times S^2 divided by the molar gas constant R and T^2 versus normalized temperature squared, $(k_B T/J_1)^2$, for the square lattice with only nearest-neighbor couplings J_1 (exchange constants $J_2 = J_c = 0$). Quantum Monte Carlo (QMC) data (solid symbols) for spins $S = 1/2$, 1, and 3/2 are shown, together with error bars. The dotted lines are fits of the data by Eq. (103) assuming the specific $A(S)$ y intercepts given in the text below Eq. (103). Only the slopes $D(S)$ were fitted. The fitting ranges of T^2 were 0–0.06 for $S = 1/2$, 0–0.25 for $S = 1$, and 0–0.5 for $S = 3/2$.

in Table II obtained from the fit of the inelastic neutron scattering data by spin wave theory. Note that the neutron fit only provides products of the J values with S. Using the above-given parameters, Eq. (96) predicts

(1) $T_N = 550$ K for $S = 2$,
(2) $T_N = 640$ K for $S = 5/2$.

A comparison of these values with the experimental value $T_N = 620$–625 K clearly favors spin 5/2 over spin 2 for the Mn ions. Indeed, the T_N calculated for $S = 5/2$ is remarkably close to the observed value.

B. Magnetic susceptibility

Our tables of calculated susceptibilities are in the form of Eq. (82). A very useful quantity for comparison with experimental susceptibility data is the product of the scaled maximum susceptibility $\chi^{max}J_1/Ng^2\mu_B^2$ and the scaled temperature at which the maximum occurs $k_B T^{max}/J_1 S(S+1)$. Setting N equal to Avogadro's number N_A so that χ is the susceptibility per mole of spins, the product of these two variables is

$$\left(\frac{\chi^{max}J_1}{N_A g^2\mu_B^2}\right)\left[\frac{k_B T^{max}}{J_1 S(S+1)}\right] = \frac{\chi^{max}T^{max}}{3C}, \tag{104}$$

where C is the Curie constant in Eq. (23). This product does not contain any exchange constants and hence is a potential diagnostic for the value of the spin S from experimental data. One cannot hope to obtain a good fit to an experimental $\chi(T)$ data set by the theoretical predictions unless one can at least fit the experimental $\chi^{max}T^{max}$ datum. The quantities $\chi^{max}J_1/Ng^2\mu_B^2$, $k_B T^{max}/S(S+1)J_1$, and $\chi^{max}T^{max}/3C$ are listed in Table VII for both the classical and quantum Monte Carlo simulations. Using the values of C obtained from
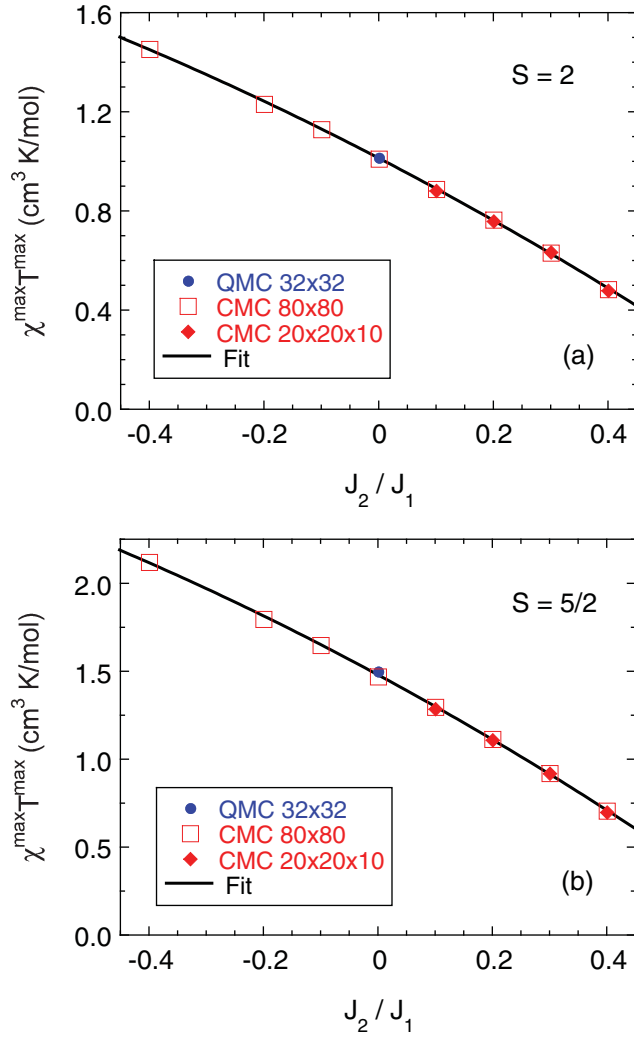
FIG. 27. (Color online) Product of the maximum susceptibility $\chi^{\max}$ per mole of spins and the temperature $T^{\max}$ at which it occurs for the J_1-J_2 model on a Heisenberg square spin lattice for spins (a) $S = 2$ and (b) $S = 5/2$, versus the ratio J_2/J_1 of the diagonal next-nearest-neighbor coupling to the nearest-neighbor coupling. Here a g factor $g = 2$ was assumed. The data were obtained using quantum Monte Carlo (blue, QMC) and classical Monte Carlo (red, CMC) simulations on the lattice sizes indicated. The $\chi^{\max} T^{\max}$ values obtained from CMC for the three-dimensional lattices are very insensitive to the coupling J_c between layers up to at least $J_c/J_1 = 0.1$, as shown in Table VII. The solid black curves in (a) and (b) are least-squares fits to the respective data by the second-order polynomials in Eqs. (105).

Eq. (23) using $g = 2$, the predicted values of $\chi^{\max} T^{\max}$ for direct comparison to our experimental datum are listed in Table VII for the quantum value of S in the QMC simulations and for classical values $S = 2$ and $S = 5/2$ in the CMC simulations, respectively. One sees from the table that the value of $\chi^{\max} T^{\max}$ is very sensitive to the ratio J_2/J_1 but that it hardly changes for a given J_2/J_1 as the interlayer coupling ratio J_c/J_1 is changed over the range from 0 to 0.1.

Plots of $\chi^{\max} T^{\max}$ versus J_2/J_1 are shown in Figs. 27(a) and 27(b) for $S = 2$ and $S = 5/2$, respectively. The data were

fitted by the second-order polynomials

$$
\chi^{\max} T^{\max} = 1.012 - 1.202 \left(\frac{J_2}{J_1}\right) - 0.2712 \left(\frac{J_2}{J_1}\right)^2,
$$

$$
\chi^{\max} T^{\max} = 1.478 - 1.757 \left(\frac{J_2}{J_1}\right) - 0.4146 \left(\frac{J_2}{J_1}\right)^2
$$

(105)

for $S = 2$ and $S = 5/2$, respectively, as shown by the respective solid curves in Fig. 27, where the units of the fits are cm^3 K/mol. The rms deviations of the fits from the data are 0.005 and 0.010 for $S = 2$ and $S = 5/2$, respectively.

A comparison of the calculated values of $\chi^{\max} T^{\max}$ in Fig. 27 and Eqs. (105) with the observed value $\chi^{\max} T^{\max} = 0.80$ cm^3 K/mol Mn in Eq. (20) indicates that the local moment model can reproduce the observed $\chi^{\max} T^{\max}$ value with the following combinations of parameters:

(i) $g = 2$, $S = 2$, and $J_2/J_1 \approx 0.17$;
(ii) $g = 2$, $S = 5/2$, and $J_2/J_1 \approx 0.36$.

In the J_1-J_2 model, the G-type AF magnetic structure that is observed in BaMn$_2$As$_2$ is stable against the stripe state as long as $J_2/J_1 < 1/2$ [Eq. (4)], which is satisfied by both of these estimates. We do not have simulation data for precisely these two values of J_2/J_1. Also, the parameter set $\{S, J_1, J_2, J_c\}$ is underdetermined by the experimental susceptibility data, so we have to make choices about some of the parameters when we fit the experimental data by the available classical Monte Carlo data. We choose $J_c/J_1 = 0.1$ because this value is indicated both from the neutron scattering fit in Table II above and from the theoretical results in Table IX below. For each of the two potential values $S = 2$ and $5/2$, we use the respective CMC J_2/J_1 simulation in Table VII that shows the closest agreement with the experimental $\chi^{\max}_{\mathrm{spin}} T^{\max}$ for that spin value, namely,

(1) Fit 1: $J_2/J_1 = 0.2$, $J_c/J_1 = 0.1$, $S = 2$;
(2) Fit 2: $J_2/J_1 = 0.4$, $J_c/J_1 = 0.1$, $S = 5/2$.

Next, we have a choice of how to obtain a precise fit to the magnitude of the experimental data by the simulation data for $J_2/J_1 = 0.2$ and 0.4, both with $J_c/J_1 = 0.1$. We could adjust the g factor, the orbital contribution to the susceptibility, and/or the spin value. At this stage such changes are just fitting parameters, so we arbitrarily choose to adjust the spin value slightly to obtain a good numerical fit of the particular simulation to the experimental value of $\chi^{\max}_{\mathrm{spin}} T^{\max}$ given in Eq. (20). Then we fix the value of J_1 by substituting the experimental value of $\chi^{\max}_{\mathrm{spin}} = 0.80 \times 10^{-3}$ cm^3/mol Mn and $g = 2$ into the expression $\chi^{\max} J_1/N_A g^2 \mu_B^2$ and equating that with the $\chi^{\max} J_1/N g^2 \mu_B^2$ value listed in Table VII. The parameters obtained from the two fits are listed in Table VIII. Remarkably, the value of J_1 is not sensitive to the values of S, J_2, or J_c, and a consistent value $J_1 \approx 210$ K $= 18$ meV is obtained for both fits. The two fits are compared with the experimental data from Fig. 7(a) in Fig. 28. When plotting the fits, the calculated spin susceptibility per mole of spins has to be multiplied by two (two atoms of Mn per formula unit) and then added to the orbital contribution given in Eq. (18). These fits are only valid in the paramagnetic regime above $T_N = 625$ K, but they are extrapolated to lower temperatures. The quality of the fits to the experimental data is reasonable for both fits. Thus, we cannot distinguish between the two possibilities $S = 2$ and $S = 5/2$ for the Mn spins on the basis of magnetic susceptibility measurements alone.

TABLE VIII. Parameters determined from a fit of magnetic susceptibility data for BaMn$_2$As$_2$ by classical Monte Carlo simulations. The value $J_c/J_1 = 0.1$ was chosen to agree with the inelastic neutron scattering and band-theoretical values which are both close to 0.1. The values of J_2/J_1 were fixed at the listed values by comparing the predicted values of $\chi_{\rm spin}^{\rm max} T^{\rm max}$ with the experimental values for $S = 2$ and $S = 5/2$. Then the spin value S was determined more precisely by fitting the respective CMC simulation to the experimental value of $\chi_{\rm spin}^{\rm max} T^{\rm max}$. Finally J_1 was found by fitting the experimental value of $\chi_{\rm spin}^{\rm max}$ to the theoretical value for the respective simulation.

Quantity	Fit 1	Fit 2
S	2.06	2.64
J_1	207 K = 17.8 meV	210 K = 18.1 meV
J_2	$\equiv$41.4 K = 3.6 meV	$\equiv$85 K = 7.3 meV
J_2/J_1	$\equiv$0.2	$\equiv$0.4
J_c	$\equiv$21 K = 1.8 meV	$\equiv$21 K = 1.8 meV
J_c/J_1	$\equiv$0.1	$\equiv$0.1

XI. ^{75}As NMR MEASUREMENTS AND ANALYSIS

A. ^{75}As NMR spectrum

As shown in Fig. 1, each As atom is coupled to four Mn atoms. Thus, through ^{75}As NMR one can probe the magnetism of the Mn sublattice in BaMn$_2$As$_2$. Figure 29 shows typical ^{75}As NMR spectra in the magnetically ordered state at different temperatures $T < T_N$ for a polycrystalline sample of BaMn$_2$As$_2$. At low temperatures, along with the most intense central line the spectrum contains extra shoulderlike features on either side. The broad linewidth is attributed to the random orientation of the internal field with respect to the external field in the powder sample. ^{75}As has an electric quadrupolar moment

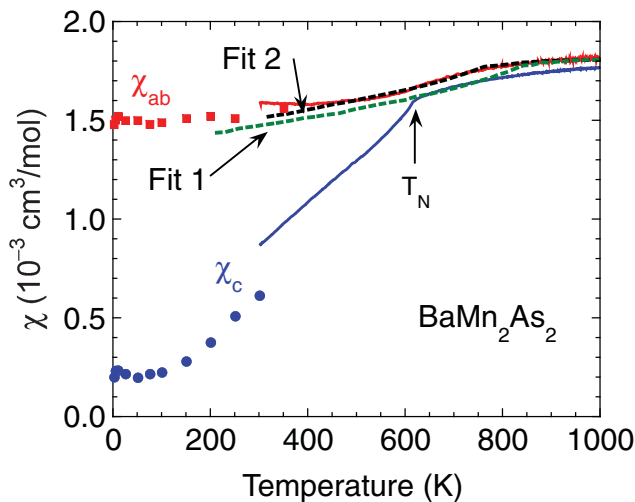FIG. 28. (Color online) Two fits (Fit 1 and Fit 2, dashed curves) of the high-temperature magnetic susceptibility χ of BaMn$_2$As$_2$ from Fig. 7(a) by CMC simulations. The fits are only valid above T_N but are extrapolated to lower temperatures. The fit parameters are given in Table VIII. The temperatures of the breaks in slope of the fits are discernable and denote the predicted Néel temperatures in Eq. (96) for the respective parameters, which are somewhat above the observed value.
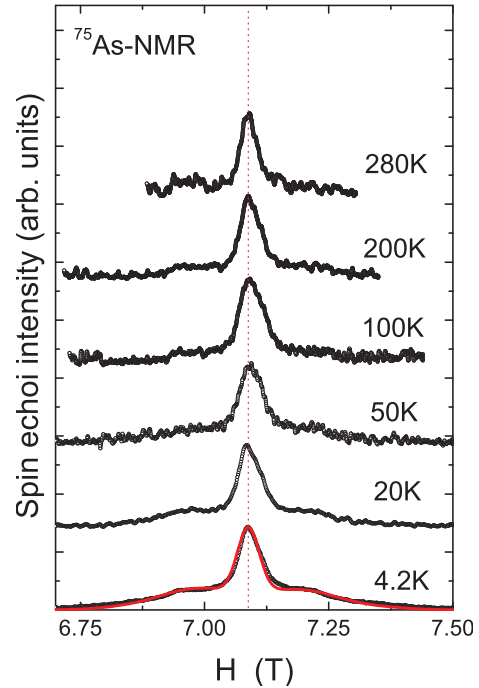

FIG. 29. (Color online) ^{75}As NMR spectra for polycrystalline BaMn$_2$As$_2$ at different temperatures. The solid red line is a fit to the spectrum at 4.2 K.

that interacts with the local electric field gradient (EFG) in the crystal giving rise to the splitting of the NMR line. Thus, in principle, one should see in the ^{75}As spectra three allowed transitions: an $I_z = -\frac{1}{2} \leftrightarrow +\frac{1}{2}$ central transition and two $I_z = \pm\frac{1}{2} \leftrightarrow \pm\frac{3}{2}$ satellite transitions. Therefore, in an attempt to fit the experimental spectra taking into account both the EFG and the isotropic spin shift effects, we find that the spectrum at 4.2 K can be fitted reasonably well with isoshift $K_{\rm iso} \simeq 0.38\%$, quadrupolar frequency $\nu_Q \simeq 2.1$ MHz, width of central peak 0.43 kOe, width of satellite 1.13 kOe, and EFG asymmetry parameter $\eta \simeq 0.0$. The fit is shown as the solid red curve through the data at 4.2 K in Fig. 29. The value of ν_Q is comparable to that reported for BaFe$_2$As$_2$ in the ordered state.[59]

The linewidth and position were found to be almost temperature independent. As shown in Ref. 13 from magnetic neutron diffraction data, the sublattice magnetization is nearly saturated at 300 K. Since the NMR linewidth in the ordered state is a measure of the sublattice magnetization, the independence of the linewidth over our temperature range is consistent with the neutron diffraction results.

The internal field at the ^{75}As site can be analyzed by taking the crystal symmetry into consideration, which has been adopted in an analysis of the hyperfine field at the ^{75}As site in BaFe$_2$As$_2$ by Kitagawa et al.[59] According to their analysis, for a G-type antiferromagnetic spin structure the internal field at the ^{75}As site is zero due to a perfect cancellation of the off-diagonal hyperfine field produced by four in-plane NN Mn spins when the spin moments are parallel to the c axis. Thus, the spin components along this axis do not produce any magnetic broadening in the ^{75}As NMR spectra. Only the ab plane components of the ordered Mn spin can produce an internal field perpendicular to the c axis at the ^{75}As site. On the other

hand, for a stripe-type AF spin structure, a *c*-axis component of the spin moments produces an internal field $H_{int} = z'BS$ along the *a* axis, where z' is the number of nearest-neighbor Mn spins of the ^{75}As site, B is the off-diagonal hyperfine coupling constant, and S is the Mn spin.

Assuming that the broadening of the NMR spectra originates from H_{int} at the ^{75}As site, H_{int} is estimated to be $\sim$215 Oe from the spectral width. Using the ordered moment $\mu = 3.9\ \mu_B$/Mn and $z' = 4$, the off-diagonal hyperfine coupling constant B is estimated to be $\sim$14 Oe/μ_B for the case of stripe-type AF order. Such a small B is of the order of the nuclear-nuclear dipolar field and is not likely due to transferred hyperfine couplings. For the G-type AF structure, the *ab*-plane components can be produced by a canted component of the Mn spins when the magnetic field is applied perpendicular to the ordered moment axis, that is, perpendicular to the *c* axis. Using the perpendicular component of the spin susceptibility $\chi_\perp = 1.3 \times 10^{-3}$ cm^3/mol from Fig. 7(a) and $H = 7.1$ T that we used for measurements of the spectra, the *ab* component of the ordered Mn moment μ_{ab} is evaluated to be 0.0083 μ_B/Mn in this field. Now using $H_{int} = 215$ Oe and $\mu_{ab} = 0.0083\ \mu_B$, the off-diagonal hyperfine coupling constant is calculated to be $B = 6.5$ kOe/μ_B. This value of B is comparable to $B = 4.3$ kOe/μ_B reported in BaFe$_2$As$_2$.[59] Thus, our ^{75}As NMR spectra observed in the AF ordered state are consistent with the G-type AF structure reported from the neutron experiment.[13]

B. Nuclear spin-lattice relaxation rate

The longitudinal nuclear magnetization recovery curve following saturation was fitted by the double exponential function[60]

$$1 - \frac{M(t)}{M(\infty)} = 0.1\, e^{-t/T_1} + 0.9\, e^{-6t/T_1},$$

as expected for the center line of the spectrum of the ^{75}As nuclear spin $I = \frac{3}{2}$, where $1/T_1$ is the ^{75}As nuclear spin-lattice relaxation rate and $M(t)$ and $M(\infty)$ are the nuclear magnetization at time t after saturation and the equilibrium nuclear magnetization at time $t = \infty$, respectively. The extracted $1/T_1$ as a function of temperature is shown in Fig. 30, where $1/T_1$ is seen to increase rapidly with increasing temperature. In the AF state, this rapid increase in $1/T_1$ with T is a clear signature of relaxation due to scattering of magnons by the nuclear spins. According to Beeman and Pincus,[61] in the AF state for magnetic insulators, $1/T_1$ is mainly driven by such magnon processes, leading to a power law T-dependence.[61–63] For $T \gg \Delta/k_B$, where Δ is the anisotropy gap in the spin wave spectrum, it either follows a T^3 behavior due to a two-magnon Raman process or a T^5 behavior due to a three-magnon process, while for $T \ll \Delta/k_B$, it follows a thermally activated behavior $1/T_1 \propto T^2 e^{-\Delta/k_B T}$. As seen from Fig. 30, our ^{75}As $1/T_1$ data in the T range $50 \leqslant T \leqslant 300$ K follow a T^3 behavior rather than a T^5 behavior, indicating that the relaxation is mainly governed by the two-magnon Raman process. A T^3 fit over this T range yields

$$\frac{1}{T_1} = (2.51 \times 10^{-6}\ \text{s}^{-1}\ \text{K}^{-3})\, T^3, \tag{106}$$
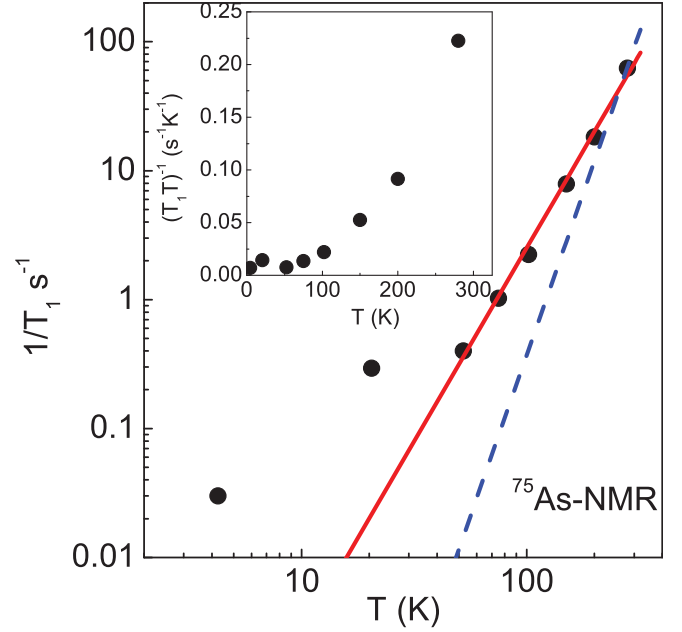

FIG. 30. (Color online) Nuclear spin-lattice relaxation rate ($1/T_1$) measured at the ^{75}As site versus temperature T. The solid and dashed lines represent T^3 and T^5 behaviors, respectively. The slope of the former line fitted to the 50–300 K data is 2.51×10^{-6} s^{-1}K^{-3}. (Inset) $(T_1 T)^{-1}$ versus T.

as shown in Fig. 30. The lack of activated behavior down to 50 K indicates that Δ/k_B is smaller than 50 K.

For the two-magnon process, $1/T_1$ is determined by the slopes of the spin wave dispersion relations at $\omega \sim 0$ and thus by the spin wave velocities. The spin wave velocities within the *ab* plane and along the *c* axis in terms of the exchange constants in the J_1-J_2-J_c Heisenberg model are given above in Eqs. (9). Since the spin wave velocity depends on the direction of propagation, $1/T_1$ should also depend on the spin wave direction. Based on the $1/T_1$ expression for the two-magnon process reported by Beeman and Pincus,[61] we have calculated the $1/T_1$ for BaMn$_2$As$_2$ with the body-centered-tetragonal structure ($I4/mmm$) arising from the two spin wave velocities as

$$\left(\frac{1}{T_1}\right)_i^{-1} = \left(\frac{A}{\hbar}\right)^2 \frac{4z'z\hbar \sin^2\theta}{(2\pi)^3} (k_B T)^3 \frac{(a^2 c)^2}{(\hbar v_i)^4 \alpha^2}$$
$$\times \int_{\Delta/k_B T}^{\infty} \frac{x}{e^x - 1}\, dx, \tag{107}$$

where $z' = 4$ is the number of Mn nearest neighbors to a given ^{75}As site (see Fig. 1), $z = 4$ is the number of nearest-neighbor Mn spins interacting with a given Mn spin, $i = ab$ with $\alpha = a$ or $i = c$ with $\alpha = c$, and θ denotes the angle between the local hyperfine field at the ^{75}As site and the anisotropy axis (*c* axis) which is the Mn ordered moment axis. We also have

$$\frac{A}{\hbar} = \gamma_n g \mu_B A_{hf},$$

where g is the electronic g factor, A_{hf} is the hyperfine coupling constant and γ_n is the ^{75}As nuclear gyromagnetic ratio given by $^{75}\gamma_n/2\pi = 7.2919$ MHz/T. Using $g = 2$ and

$A_{hf} = 6.5$ kOe/μ_B that was estimated from the spectrum analysis, one obtains

$$\frac{A}{\hbar} = 6.0 \times 10^7 \text{ s}^{-1}. \tag{108}$$

For $T \gg \Delta/k_B$ as in our temperature range 50–300 K where $1/T_1 \propto T^3$, the integral in Eq. (107) approaches its maximum value $\pi^2/6$, so Eq. (107) reduces to

$$\left(\frac{1}{T_1}\right)_{ab}^{-1} = \left(\frac{A}{\hbar}\right)^2 \frac{z'z\hbar a^2 c^2 k_B^3 \sin^2\theta}{12\pi(\hbar v_{ab})^4} T^3. \tag{109}$$

$$\left(\frac{1}{T_1}\right)_c^{-1} = \left(\frac{A}{\hbar}\right)^2 \frac{z'z\hbar a^4 k_B^3 \sin^2\theta}{12\pi(\hbar v_c)^4} T^3$$

$$\equiv C_{ab \text{ or } c} T^3. \tag{110}$$

The ratio $R_{ab/c}$ of the relaxation rates for ab-plane and c-axis spin waves should be independent of T. If we assume that the hyperfine coupling A of the electronic spins to the nuclear spins is isotropic, then $R_{ab/c}$ obtained using Eqs. (9), (109), and (110) is given by

$$R_{ab/c} = \frac{(1/T_1)_{ab}}{(1/T_1)_c} = \left(\frac{c}{a}\right)^2 \left(\frac{v_c}{v_{ab}}\right)^4$$

$$= \frac{1}{4}\left(\frac{c}{a}\right)^6 \left[\frac{(J_c/J_1)(1+J_c/2J_1)}{(1-2J_2/J_1)(1+J_c/2J_1)}\right]^2. \tag{111}$$

Taking $a = 4.15$ and $c = 13.41$ Å for the lattice parameters at 8 K (Ref. 13), and $J_2/J_1 = 0.29$ and $J_c/J_1 = 0.09$ from the neutron scattering fit in Table II, Eqs. (111) yield

$$R_{ab/c} = 13. \tag{112}$$

Thus, the nuclear spin-lattice relaxation rate due to spin waves traveling in the ab plane is much larger than that due to c-axis spin waves and we therefore assume that Eq. (109) gives the observed $1/T_1$ to a good approximation.

Since A_{hf} was estimated in Eq. (108), one can obtain information on the exchange constants from the coefficient of the T^3 fit in Eq. (106). Inserting $\hbar v_{ab}$ from Eqs. (9) into (109) gives

$$\left(\frac{J_1}{k_B}\right)^4 = \frac{1}{C_{ab}}\left(\frac{A}{\hbar}\right)^2 \left(\frac{c}{a}\right)^2 \frac{z'z\hbar\langle\sin^2\theta\rangle}{192\pi k_B S^4}$$

$$\times \left[\left(1 - \frac{2J_2}{J_1}\right)\left(1 + \frac{J_c}{2J_1}\right)\right]^{-2}. \tag{113}$$

Our single fit parameter C_{ab} in Eq. (106) can only be used to determine a single exchange constant or a single combination of them. We therefore estimate J_1 using the above values $J_2/J_1 = 0.29$ and $J_c/J_1 = 0.09$ derived from our inelastic neutron scattering experiments. In Eq. (113), we also use $z' = 4$, $z = 4$, we take S to be the ordered spin $\langle S \rangle = 2$ (from magnetic neutron diffraction experiments),[13] and $\langle\sin^2\theta\rangle = (1/2)\int_0^\pi \sin^3\theta \, d\theta = 2/3$ (i.e., considering an average over all angles). Using Eq. (113), we then obtain

$$\frac{J_1}{k_B} = 160 \text{ K}, \quad J_1 = 14 \text{ meV} \quad S \equiv 2. \tag{114}$$

This value is close to the value $J_1 = 16$ meV estimated in Table II for $S = 2$ from our neutron scattering data. If we take

the spin to be $S = 5/2$, the value of J_1 from Eq. (113) would be a factor of $(5/4)^4 = 2.4$ times smaller.

The overall temperature dependence of $1/T_1$ in BaMn$_2$As$_2$ in Fig. 30 is similar to that reported for KMnF$_3$ (Ref. 64). In KMnF$_3$, a deviation from power law behavior was observed at low temperatures and $1/T_1$ shows a broad maximum. This broad feature at low temperature was attributed to the effects of defects or extrinsic impurities. Thus, in BaMn$_2$As$_2$, the deviation of the data below 50 K from the higher-temperature T^3 fit in Fig. 30 is likely due to relaxation associated with defects and/or extrinsic impurities.

For a metallic system, one would expect a Korringa-like behavior [$(T_1 T)^{-1} = $ constant] as has been observed in (Ba,Ca)Fe$_2$As$_2$ (Refs. 59, 65, and 66) and RFeAsO$_{1-x}$F$_x$ ($R =$ La, Pr) (Refs. 67 and 68) in the paramagnetic state. In these compounds, $(T_1 T)^{-1}$ is also constant at low temperature below T_N due to their metallic character and increases sharply near T_N. In contrast, $(T_1 T)^{-1}$ in BaMn$_2$As$_2$ (inset of Fig. 30) shows a gradual increase with increasing temperature signifying the insulating ground state of the compound.

XII. BAND-THEORETICAL ESTIMATES OF THE EXCHANGE COUPLINGS

The quantitative analysis of the magnetic interactions in real magnets is based mostly on density functional theory. To a large extent this theory is very similar to the Fermi-liquid theory of Landau; however, strictly speaking, it allows one to obtain only the total energy of the ground state, the distribution of charge and spin densities, and other quantities that can be directly determined by these. Several notable exceptions (Mott insulators, rare earth systems, systems near quantum critical points) have been revealed but currently it is believed that for magnets of the Fe group the accuracy of the commonly used local density approximation (LDA) is acceptable for the description of the ground state properties including the equilibrium magnetic moments at $T = 0$ K.

While the numerical agreement between experimental and theoretical magnetic moments is often very good, there are certain cases when the local approximation numerically violates quantum mechanical laws. For instance, even in insulating systems or magnetic molecules where the total magnetic moment is close to an integer number of Bohr magnetons, the value obtained from density functional theory is usually not an integer. This discrepancy is related to the fact that the wave function of the density functional method is often not an eigenfunction of the square of total spin (even without relativistic effects). This effect of "spin contamination" usually cannot be eliminated or easily resolved. While noninteger values of the moment in metallic systems are traditionally explained by itinerancy of the system and partial occupation numbers, the problematic issue of whether or not $\mathbf{S}^2$ is an integral of the motion is usually ignored with the hope that such errors are small. The relationship between the single-particle spectrum obtained in the density functional theory and the physical properties of the magnetic excitations is not clearly defined. Nevertheless, the research of the last 20–25 years revealed that LDA often provides good agreement between theory and experiment for the magnetic excitation spectra if the ground state is properly described.
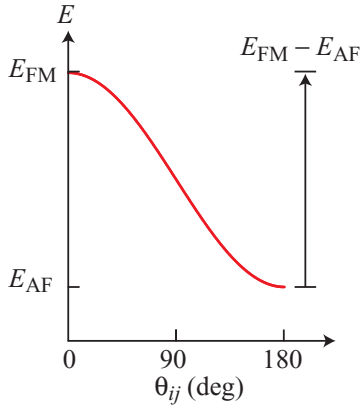
FIG. 31. (Color online) Total energy E of a system when the polar angle θ_{ij} between two local magnetic moments i and j is varied in band theory. The energies of the ferromagnetic E_{FM} and antiferromagnetic E_{AF} magnetic structures and their difference are indicated. Here the antiferromagnetic state is the ground state. For a ferromagnetic ground state, the minimum in energy would be at $\theta_{ij} = 0$.

The description of the intersite magnetic interactions represents a typical problem within the topic of magnetic excitations. By itself, the determination of a pairwise exchange parameter J_{ij} between atoms i and j in an arbitrary magnetic material is not well-posed. For instance, in very itinerant systems the effective spin Hamiltonian can have very non-Heisenberg behavior. However, from the phenomenological theory of ferromagnetism[69,70] the energy of any weak and smooth variation of spin density can be described by the effective classical Heisenberg Hamiltonian for equivalent classical spins $\mathbf{S}_i$ and $\mathbf{S}_j$ with magnitudes $S_i = S_j \equiv S$ given by

$$E = \sum_{\langle ij \rangle} J_{ij}\mathbf{S}_i \cdot \mathbf{S}_j = S^2 \sum_{\langle ij \rangle} J_{ij} \cos \theta_{ij}. \tag{115}$$

Traditionally, a set $\{J_{ij}\}$ of exchange coupling constants in the density functional theory can be calculated using two approaches. In the first approach, using the effective Heisenberg model (115) one can solve for the J_{ij} from the set $\{F_{\alpha\beta}(J_{ij})\}$ of equations for the differences of the energies between different magnetic structures α and β

$$F_{\alpha\beta}(J_{ij}) = \frac{E_\alpha\{J_{ij}\} - E_\beta\{J_{ij}\}}{2S^2} \tag{116}$$

obtained from band structure calculations as shown in Fig. 31. This is the usual way to obtain $\{J_{ij}\}$ for highly localized magnetic insulators and is usually the most suitable method for the calculation of magnetic phase transition temperatures.

Another approach is based on the definition of J_{ij} as the second derivative of the total energy in Eq. (115) with respect to rotation of moments from their magnetic alignment in a given magnetically ordered ground state

$$J_{ij} = -\frac{1}{S^2}\frac{\partial^2 E}{\partial \theta_{ij}^2}, \tag{117}$$

which is proportional to the curvature of the total energy E versus angle θ_{ij} near the minimum for an antiferromagnet at $\theta_{ij} = 180°$ in Fig. 31. This definition of J_{ij} corresponds

to a linear response scheme and is usually the most suitable technique for the analysis of the excitations above the ground state (spin waves) and is directly related to the dynamical magnetic susceptibility measured in inelastic neutron scattering experiments. The procedure for evaluating Eq. (117) depends on the band structure methods and the specifics of the linear response method employed. This technique has been used for many magnetic materials in the past.[71] This approach can be understood as a static limit of the dynamic linear response technique which has been used for calculations of spin waves and Stoner excitation spectra in magnets. One can analytically obtain an expression for the onsite stability parameter J_0 which should be the same as $\sum J_{ij}$. A comparison of J_0 and $\sum J_{ij}$ is a check on the consistency of the calculations and the reliability of the numerical scheme.

We first consider the exchange constants obtained from total energy differences and then in the subsequent section from the energy of excitations from the magnetically ordered ground state.

A. Exchange interactions from total energy calculations

Using density functional theory in the LDA, An *et al.* correctly deduced from total energy calculations, prior to the availability of the experimental results, that the G-type antiferromagnetic structure of $BaMn_2As_2$ has a lower energy than either the FM structure or of two types of stripe structure.[12] Their predicted ordered moment for the G-type AF structure was $\mu = 3.20 \, \mu_\mathrm{B}/\mathrm{Mn}$, somewhat smaller than the value of $\mu = 3.9(1) \, \mu_\mathrm{B}/\mathrm{Mn}$ observed later.[13] Their LDA total energies and ordered moments for the FM and G-type AF structures are listed in Table IX, together with their total energies of two commensurate collinear stripe states with the in-plane stripe structure shown in the bottom panel of Fig. 2.[12] The stripe-AF structure has AF alignment of the ordered moments along the c axis, whereas the stripe-FM structure has FM alignment along the c axis. As seen in Table IX, the ordered moment μ of the Mn in the FM structure is not the same as the value of μ in the G-type AF structure.

From the LDA total energies and ordered moments calculated by An *et al.*[12] for the magnetic structures listed in Table IX, one can obtain estimates of the exchange couplings in $BaMn_2As_2$ using the value for the spin S obtained from the ordered moment μ as

$$S = \frac{\mu}{g\mu_\mathrm{B}} = \frac{\mu}{2\mu_\mathrm{B}},$$

with $g = 2$. The classical energies per spin of the magnetic structures in Table IX obtained using Eqs. (3) and Fig. 2 are

$$\begin{aligned} E_{\mathrm{FM}} &= S_{\mathrm{FM}}^2(2J_1 + J_c + 2J_2), \\ E_{\mathrm{G}} &= S_{\mathrm{G}}^2(-2J_1 - J_c + 2J_2), \\ E_{\mathrm{stripe\,AF}} &= S_{\mathrm{G}}^2(J_c - 2J_2), \\ E_{\mathrm{stripe\,FM}} &= S_{\mathrm{G}}^2(-J_c - 2J_2). \end{aligned} \tag{118}$$

We have taken the Mn spin in the two stripe phases to be the same as in the G-type AF structure, since they were not given by An *et al.* Because the total energy contains a constant term proportional to the square of the magnetization, we solve for the exchange constants using only differences between

TABLE IX. Parameters of BaMn$_2$As$_2$ with NN (J_1), NNN (J_2), and interlayer (J_c) exchange interactions obtained from density functional theory. Here S is the calculated spin, E is the total energy per Mn atom, FM means ferromagnetic structure and G-type AF structure is the Néel (checkerboard) antiferromagnetic structure with an in-plane structure shown in the top panel of Fig. 2. The two stripe structures have the in-plane antiferromangetic structure shown in the bottom panel of Fig. 2, where the stripe-AF structure has AF stacking and the stripe-FM structure has FM stacking along the c axis. The estimated exchange constants J in rows 5 and 6 are calculated from Eqs. (119)–(121) using the total energy values in column 4. Our exchange constants using the LDA and GGA in the last two rows were calculated from the excitation energies from the magnetically ordered ground state. In the reference (Ref.) column, "PW" means "present work."

Magnetic structure	μ (μ_B/Mn)	S	E/Mn (meV)	$2J_1 + J_c$ (meV)	J_c (meV)	J_1 (meV)	J_2 (meV)	J_c/J_1	J_2/J_1	Ref.
FM	2.74	1.37	−330							12
G-type AF	3.20	1.60	−660							12
Stripe-AF	≡ 3.20	≡ 1.60	−515							12
Stripe-FM	≡ 3.20	≡ 1.60	−505							12
				41.0[a]	2.0[a]	19.5[a]	−5.4[a]	0.10[a]	−0.28[a]	12, PW
				28.5[b]	1.2[b]	13.7[b]	−2.5[b]	0.09[b]	−0.18[b]	12, PW
FM (LDA)	2.8	1.4			≈0	−9.1	−2.2			PW
FM (GGA)	3.0	1.5								PW
G-type AF (LDA)	3.3	1.65		27.2	1.03	13.1	2.8	0.08	0.21	PW
G-type AF (GGA)	3.6	1.8		26.2	1.0	12.6	2.7	0.08	0.21	PW

[a]Calculated using Eqs. (119)–(121) as written.
[b]Calculated by replacing S^2 by $S(S + 1)$ in Eqs. (119)–(121).

these total energies according to Eq. (116). From the last two expressions in Eqs. (118) we obtain

$$J_c = \frac{1}{2S_G^2}(E_{\text{stripe FM}} - E_{\text{stripe AF}}). \quad (119)$$

From the first two expressions in Eqs. (118) we obtain

$$2J_1 + J_c = \frac{1}{2}\left(\frac{E_{\text{FM}}}{S_{\text{FM}}^2} - \frac{E_G}{S_G^2}\right). \quad (120)$$

Thus Eqs. (119) and (120) determine the two exchange constants J_1 and J_c. Then from the second and fourth of Eqs. (118) we solve for J_2 according to

$$J_2 = \frac{J_1}{2} - \frac{E_{\text{stripe FM}} - E_G}{4S_G^2}. \quad (121)$$

It is not clear whether to retain S^2 or to insert the quantum mechanical expectation value $S(S + 1)$ of $\langle S^2 \rangle$ in place of S^2 in Eqs. (119)–(121), so we calculate two sets of exchange parameters based on these two assumptions, which are given in Table IX. Using the second assumption, the values of J_c and J_1 are respectively about the same as the values in Table II deduced from our inelastic neutron scattering experiments, but J_2 has the opposite sign in the theory and experiment.

We studied the properties of BaMn$_2$As$_2$ using density functional calculations of the electronic structure and magnetic interactions in the FM and G-type AF structures. For consistency, we used the experimental values of the lattice parameters $a = 4.15$Å and $c = 13.47$ Å and the theoretically optimized value of the internal As parameter $z_{As} = 0.3524$ utilized by An *et al.*[12] Our electronic structure calculations were performed using the recently developed full-potential linear muffin tin orbital program.[72] The accuracy of the exchange couplings obtained is about 2%–3%. The studies of the exchange couplings were done using the static linear response technique described in Refs. 73 and 74.

Our results using LDA and the generalized gradient approximation (GGA) are very similar to those reported by An *et al.*[12] We find that BaMn$_2$As$_2$ has a relatively large ordered moment in the G-type AF structure with $\mu = 3.3$ μ_B/Mn in LDA and 3.6 μ_B/Mn in GGA, as listed in Table IX, with a small band gap (0.15 eV) in the electronic spectrum as observed, and with the G-type AF ordering having the lowest energy among all considered magnetic structures. The ferromagnetic structure has no charge gap; that is, the compound would be metallic. Our total energy $E_{\text{FM}} - E_G$ differences were 350 meV/Mn (LDA) and 375 meV/Mn (GGA), which are similar to the values of 330 and 380 meV/Mn obtained in Ref. 12, respectively.

While the magnetic moments are relatively large, they show a significant dependence on the magnetic structure, in agreement with the results of Ref. 12. For instance, the ferromagnetically ordered BaMn$_2$As$_2$ has an ordered moment of 2.8 μ_B/Mn in LDA and 3.0 μ_B/Mn in GGA, which deviate from the corresponding values for G-type AF ordering (Table IX) by about 20%. Due to this relatively strong dependence of the ordered magnetic moment on the magnetic structure, estimates of exchange couplings from total energy calculations should be used with caution.

B. Exchange interactions from excitations from the magnetically ordered ground state

For comparison with the exchange constants deduced from inelastic magnetic neutron scattering experiments, calculations using the linear response technique[71] are preferable to the total energy technique, as noted above. Our calculations of the parameters of the Heisenberg model are $J_1 = 13.1$ meV, $J_2 = 2.8$ meV, $J_c = 1.03$ meV (LDA) and $J_1 = 12.6$ meV, $J_2 = 2.7$ meV, $J_c = 1.0$ meV (GGA), as summarized in Table IX. These values are quite comparable with the values

deduced from our inelastic neutron scattering measurements in Table II, and roughly similar to those in Table IV obtained from molecular field analysis of our magnetic susceptibility data in Fig. 7.

The G-type AF ordering temperatures obtained from our spin value and exchange parameters in Table IX using the molecular field expression (41) are

$$T_{\mathrm{N}} = 730 \text{ K} \quad \text{(G-type AF, LDA)},$$
$$T_{\mathrm{N}} = 810 \text{ K} \quad \text{(G-type AF, GGA)}. \tag{122}$$

These mean-field Néel temperatures are somewhat larger than the observed value of 625 K, as expected, and indeed are approaching the temperature of the maximum of the measured susceptibility in Fig. 7(a) which from Table VII is of order the mean-field transition temperature.

The other longer-range pair exchange parameters appear to be much smaller, suggesting very short-ranged exchange interactions in this material. In particular, the difference between the above parameter J_0 and $\sum J_{ij}$ over six NN and four NNN is only about 5%, suggesting very short-ranged exchange interactions in $BaMn_2As_2$. This is different from the corresponding results for many Fe pnictides, where the exchanges with further neighbors are not so small and definitely provide a finite contribution to the spin wave spectrum.[75] We attribute this difference to the metallic character of the Fe pnictides and the semiconducting character of $BaMn_2As_2$.

To check the dependence of $\{J_{ij}\}$ on the type of magnetic order we also performed linear response calculations of the $\{J_{ij}\}$ for the FM phase. The stability parameter J_0 for this phase appears to be negative, confirming the instability of such order with respect to the deviation of a single spin from the ordered moment direction (i.e., from $\theta_{ij} = 0$). This directly supports the qualitative behavior of the total energy versus θ_{ij} in Fig. 31. The pair exchanges in this phase are $J_1 = -9.1$ meV and $J_2 = -2.2$ meV with a very weak coupling along the z direction, which are compared in Table IX with the other exchange constant values discussed above. These results indicate that not only the ordered moments are different in the different magnetic phases, but the exchange coupling parameters depend on the type of magnetic order even in materials with a relatively large (3–4 μ_{B}) magnetic moment.

Overall, the localized Heisenberg model with four NN interactions J_1 and four NNN interactions J_2 in the ab plane and two NN interactions J_c along the c axis is sufficient to theoretically describe the magnetic properties of $BaMn_2As_2$ quite well.

XIII. ORDERED MOMENT IN THE J_1-J_2-J_c HEISENBERG MODEL FROM SPIN WAVE THEORY

As previously noted, an ionic picture suggests that the spin of the Mn^{2+} ion in $BaMn_2As_2$ is $S = 5/2$, yielding for $g = 2$ an ordered moment of

$$\langle \mu \rangle = gS \, \mu_{\mathrm{B}} = 5 \, \mu_{\mathrm{B}}. \tag{123}$$

On the other hand, the observed ordered moment

$$\langle \mu \rangle = g\langle S \rangle \, \mu_{\mathrm{B}} \tag{124}$$

is only 3.9(1) μ_{B}/Mn (Ref. 13) implying a substantial spin reduction $\langle S \rangle$. In view of the sizable frustrating AF next-nearest-neighbor exchange J_2 discussed above, it is natural to ascribe the moment reduction to enhanced quantum fluctuations. In the following, we use the conventional spin wave theory to examine the quantum spin reduction for the layered J_1-J_2-J_c square lattice Heisenberg antiferromagnet.

The spin wave theory provides an expansion of the sublattice magnetization in powers of $1/S$:

$$S - \langle S \rangle = n_0 + \frac{n_1}{2S} + \frac{n_2}{(2S)^2} + \cdots, \tag{125}$$

where the leading correction n_0 is determined by noninteracting spin waves, while higher order corrections $n_{k \geqslant 1}$ come from magnon interactions. For the nearest-neighbor square lattice Heisenberg antiferromagnet the two versions of the spin wave expansion based either on the Dyson-Maleyev[76] or the Holstein-Primakoff[77] representation of spin operators yield identical results: $n_0 = 0.196\,60$, $n_1 \equiv 0$, and $n_2 = -0.0035$, such that the series (125) rapidly converges and compares extremely well with existing numerical results.

Chandra and Doucot[78] used the harmonic spin wave theory to investigate the quantum renormalization of ordered moments for the next-nearest-neighbor J_1-J_2 square lattice Heisenberg antiferromagnet. They found that the leading order correction n_0 diverges as $J_2 \rightarrow J_1/2$ due to a softening of the excitation spectrum seen in the first of Eqs. (13) above. This fact is considered as an indication of a quantum spin-liquid state around the strongly frustrated point $J_2 = J_1/2$. Subsequently, Chakravarty, Halperin, and Nelson[79] calculated the next-order correction n_1, which becomes finite for $J_2 \neq 0$, has an opposite sign compared to n_0, and also diverges at $J_2 = J_1/2$. Below, we extend the results of Chakravarty *et al.* to a finite coupling between frustrated antiferromagnetic layers. Comparison of two consecutive terms in the series (125) is necessary to judge the accuracy of the spin wave expansion for large J_2.

In the spin wave calculations for the J_1-J_2-J_c model (2) with $H = 0$ we use a single-rotating-sublattice basis[80] for the Néel structure with $\mathbf{Q} = (\pi, \pi, \pi)$ and apply the Holstein-Primakoff transformation for spin operators expanded to first-order in $1/S$. The quantum reduction of ordered moments in the harmonic approximation is given by an integral over the paramagnetic Brillouin zone,

$$n_0 = -\frac{1}{2} + \frac{1}{N} \sum_{\mathbf{k}} \frac{A_{\mathbf{k}}}{2\omega_{\mathbf{k}}}, \tag{126}$$

where N is the number of spins,

$$A_{\mathbf{k}} = 1 - j_2(1 - \gamma_{2\mathbf{k}}) + \tfrac{1}{2}j_c,$$
$$B_{\mathbf{k}} = \gamma_{1\mathbf{k}} + \tfrac{1}{2}j_c \cos k_z, \quad \omega_{\mathbf{k}} = \sqrt{A_{\mathbf{k}}^2 - B_{\mathbf{k}}^2}, \tag{127}$$

with $j_2 = J_2/J_1$, $j_c = J_c/J_1$, where $\hbar\omega_{\mathbf{k}}$ is the magnon energy in units of $4J_1 S$, and

$$\gamma_{1\mathbf{k}} = \tfrac{1}{2}(\cos k_x + \cos k_y), \quad \gamma_{2\mathbf{k}} = \cos k_x \cos k_y. \tag{128}$$

Here the positive x and y directions are defined to be in the directions of the **a** and **b** primitive square lattice translation

vectors, respectively, the positive z direction is perpendicular to the layers in the direction of the **c** lattice translation vector, and we have set $a = b = c = 1$.

To treat the effect of magnon interaction one needs to introduce various Hartree-Fock averages of the bosonic operators compatible with the harmonic spectrum. For the present model this procedure yields in addition to n_0 in Eq. (126) three other integrals:

$$m = \frac{1}{N} \sum_{\mathbf{k}} \frac{A_{\mathbf{k}} \gamma_{2\mathbf{k}}}{2\omega_{\mathbf{k}}}, \quad \Delta_1 = \frac{1}{N} \sum_{\mathbf{k}} \frac{B_{\mathbf{k}} \gamma_{1\mathbf{k}}}{2\omega_{\mathbf{k}}},$$

$$\Delta_2 = \frac{1}{N} \sum_{\mathbf{k}} \frac{B_{\mathbf{k}} \cos k_z}{2\omega_{\mathbf{k}}}. \tag{129}$$

Then, the leading nonlinear correction to the sublattice magnetization in Eq. (125) is expressed as

$$n_1 = \frac{1}{N} \sum_{\mathbf{k}} \frac{B_{\mathbf{k}}}{\omega_{\mathbf{k}}^3} \Bigg[j_2 (m - \Delta_1) \gamma_{1\mathbf{k}} (1 - \gamma_{2\mathbf{k}}) + \frac{1}{2} j_2 j_c (m - \Delta_2)$$

$$\times (1 - \gamma_{2\mathbf{k}}) \cos k_z + \frac{1}{2} j_c (\Delta_1 - \Delta_2)(\gamma_{1\mathbf{k}} - \cos k_z) \Bigg]. \tag{130}$$

For vanishing interlayer coupling $J_c = 0$, Eq. (130) becomes

$$n_1 = j_2 \left[\frac{1}{N} \sum_{\mathbf{k}} \frac{\gamma_{1\mathbf{k}}^2 (1 - \gamma_{2\mathbf{k}})}{\omega_{\mathbf{k}}^3} \right] \left[\frac{1}{N} \sum_{\mathbf{k}} \frac{A_{\mathbf{k}} \gamma_{2\mathbf{k}} - \gamma_{1\mathbf{k}}^2}{2\omega_{\mathbf{k}}} \right],$$

$$\omega_{\mathbf{k}} = \sqrt{A_{\mathbf{k}}^2 - \gamma_{1\mathbf{k}}^2}, \tag{131}$$

as in Eq. (A3) of Chakravarty *et al.*[79] To obtain Eq. (131) we replaced the factor $(m - \Delta_1)$ in Eq. (130) with its integral representation from Eqs. (129) and $B_{\mathbf{k}}$ with $\gamma_{1\mathbf{k}}$ from Eqs. (127) and set $j_c = 0$ in $A_{\mathbf{k}}$.

Numerical values of n_0 and n_1 for a range of ratios $J_2/J_1 = 0$ to 0.49 and for $J_c/J_1 = 0, 0.05$ and 0.1 are listed in Table X. These allow one to compute the spin reduction $S - \langle S \rangle$ for any value of S. The spin reduction for $S = 5/2$ is plotted in Fig. 32 for $J_c/J_2 = 0$ and 0.1. Three-dimensional effects generally suppress quantum fluctuations, as seen in a comparison of Figs. 32(a) and 32(b), and extend the validity of the spin wave

TABLE X. The first-order and the second-order corrections [Eq. (125)] to the ordered moment in the J_1-J_2-J_c stacked square lattice Heisenberg antiferromagnet.

|	$J_c = 0$		$J_c = 0.05$		$J_c = 0.1$	
J_2/J_1	n_0	n_1	n_0	n_1	n_0	n_1
0.00	0.1966	0.0000	0.1427	0.0087	0.1260	0.0088
0.05	0.2124	−0.0047	0.1529	0.0071	0.1347	0.0075
0.10	0.2312	−0.0117	0.1648	0.0045	0.1447	0.0055
0.15	0.2542	−0.0227	0.1790	0.0003	0.1566	0.0024
0.20	0.2828	−0.0405	0.1963	−0.0065	0.1709	−0.0028
0.25	0.3198	−0.0710	0.2177	−0.0182	0.1885	−0.0115
0.30	0.3698	−0.1278	0.2455	−0.0392	0.2111	−0.0270
0.35	0.4423	−0.2485	0.2832	−0.0809	0.2414	−0.0573
0.40	0.5605	−0.5691	0.3389	−0.1784	0.2853	−0.1264
0.45	0.8074	−1.9842	0.4354	−0.5045	0.3594	−0.3483
0.49	1.6005	−23.899	0.6257	−2.6777	0.5008	−1.7482
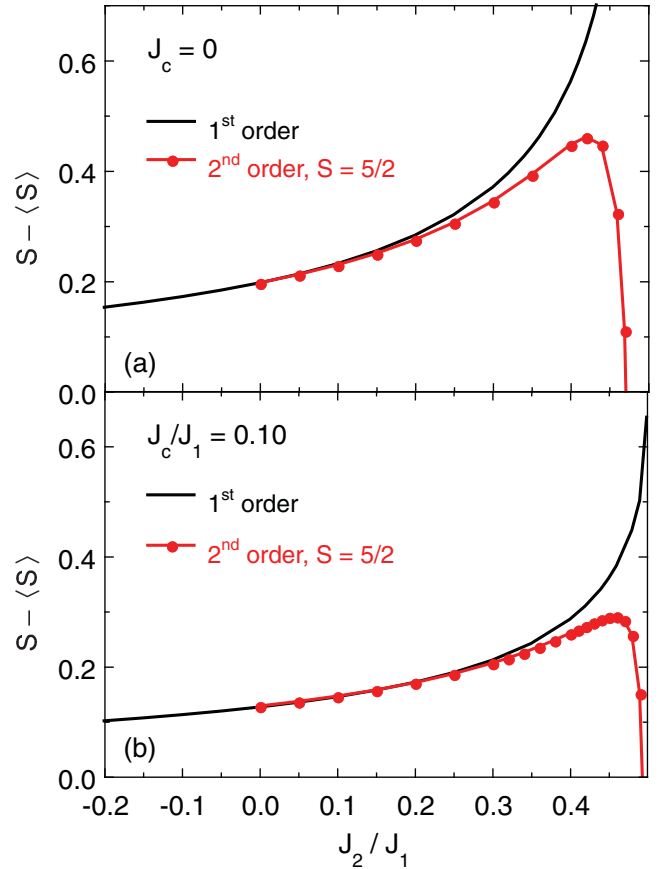
FIG. 32. (Color online) Reduction $S - \langle S \rangle$ in the ordered spin $\langle S \rangle$ from its value S in the absence of quantum fluctuations versus J_2/J_1 according to linear spin wave theory to first order (solid black curves) and second-order (solid circles) in $1/S$ for (a) $J_c = 0$ and (b) $J_c/J_1 = 0.1$.

expansion (125) to somewhat larger values of $J_2/J_1 \sim 0.44$, although the series remain divergent at $J_2/J_1 \sim 0.5$.

The above fits to our experimental neutron scattering and magnetic susceptibility results for $BaMn_2As_2$ and the band-theoretical estimates of the exchange parameters in this compound yielded $J_c/J_1 \approx 0.1$ and $J_2/J_1 = 0.2$–0.4. According to the second-order calculations in Fig. 32(b), together with Eq. (124) with $g = 2$, this parameter regime predicts an ordered moment reduction of ≈ 0.34–$0.52 \ \mu_B/Mn$ due to quantum fluctuations.[81] This result appears to rule out the possibility that the spin of the Mn is $S = 2$ because the ordered moment would then be a maximum of $\sim 3.66 \ \mu_B/Mn$ for $g = 2$, which is significantly smaller than the observed value[13] of $3.9(1) \ \mu_B/Mn$. On the other hand, if $S = 5/2$, then the corresponding predicted ordered moment is $\lesssim 4.66 \ \mu_B/Mn$, which is too large compared to the observed value.

It seems likely that charge and/or magnetic moment amplitude fluctuations, which arise from both on-site and intersite interactions, can account for the additional reduction needed to reach agreement with the observed ordered moment for a Mn spin $S = 5/2$. For example, the ordered moments of the Mn atoms are $3.50(4) \ \mu_B/Mn$ in $Sr_2Mn_3As_2O_2$,[14,15] $4.15(3) \ \mu_B/Mn$ in $La_2Mn_2Se_2O_3$,[82] and $4.04(8) \ \mu_B/Mn$ in Ba_2MnMoO_6,[83] all containing Mn^{+2} ions with nominal

spin $S = 5/2$. Such reductions are also often attributed to covalency. On the other hand, for the more ionic compound MnF_2, the ordered moment of 4.82 μ_B/Mn^{+2} is much closer to the value of 5 μ_B/Mn expected for $S = 5/2$ with $g = 2$,[84] consistent with expectation.

XIV. SUMMARY AND CONCLUSIONS

Our anisotropic magnetic susceptibility χ versus temperature T measurements from 300 to 1000 K of single crystals of $BaMn_2As_2$ yielded the Néel temperature $T_N = 618(3)$ K, close to the value of 625(1) K previously determined from neutron diffraction measurements on a polycrystalline sample.[13] The $\chi(T)$ above T_N is nearly isotropic, indicating that single-ion anisotropy effects are small and that a Heisenberg model for the spin interactions is appropriate. Below T_N, the χ becomes strongly anisotropic, with $\chi_\perp$ nearly independent of T and $\chi_\parallel$ dropping nearly to zero for $T \to 0$, which corresponds qualitatively to the textbook behavior for collinear antiferromagnets in MFT. However, the temperature dependence of χ above T_N continues to increase, rather than decrease as expected from MFT, indicating the presence of strong short-range AF order above T_N. Such short-range AF order above T_N is expected for a quasi-two-dimensional spin lattice as in $BaMn_2As_2$. Magnetic inelastic neutron scattering measurements were carried out on a polycrystalline $BaMn_2As_2$ sample at 8 K with momentum transfers up to 6 Å^{-1} and energy transfers up to 140 meV. These data allow estimates of the magnetic exchange interactions in this compound to be made using appropriate models. We also report ^{75}As NMR measurements in the antiferromagnetically ordered state of a polycrystalline $BaMn_2As_2$ sample from 4 to 300 K. The nuclear spin-lattice relaxation rate is found to obey the power law dependence $1/T_1 \propto T^3$ from 50 to 300 K which we interpret in terms of the exchange interactions in this compound.

We developed various theories for the J_1-J_2-J_c Heisenberg model in order to model our experimental data and extract values of the exchange constants between Mn spins and the value of the spin. Our inelastic neutron scattering measurements indicate that this is the minimal model needed to understand these data. For G-type antiferromagnetic ordering shown for the square spin lattice in the top panel of Fig. 2, and where the c-axis alignment is also antiferromagnetic, linear spin wave theory at $T \ll T_N$ was used to calculate the magnon dispersion relations in Sec. IV A 1. The in-plane spin waves soften as J_2 increases, and become unstable for $J_2 \geqslant J_1/2$, signaling a phase transition to the in-plane stripe state shown in the bottom panel of Fig. 2. Thus, the G-type AF ordered state requires $J_2 < J_1/2$. This theory is used in Sec. IV B to fit our inelastic magnetic neutron scattering data at 8 K, a temperature far below the Néel temperature of ≈ 625 K, and obtain estimates of SJ_1, SJ_2, and SJ_c for $BaMn_2As_2$, where S is the spin on the Mn atoms that is not determined separately in the spin wave fit to the data. From the ordered moment $\mu = 3.9(1)$ $\mu_B = gS\mu_B$, one would estimate $S = 2$ for $g = 2$. On the other hand, for the d^5 ion Mn^{+2} one would estimate a high-spin $S = 5/2$. In Sec. VIII B 1 we also calculated the spin wave contribution to the low-temperature heat capacity for comparison in Sec. VIII B 2 with our previously published[11] experimental heat capacity data for

a single crystal of $BaMn_2As_2$. We also used spin wave theory to extend the nuclear spin-lattice relaxation rate $1/T_1$ calculations of Beeman and Pincus for the isotropic cubic Heisenberg spin lattice[61] to the J_1-J_2-J_c model. We obtained Eqs. (109) and (110), which were used to analyze the fit to our ^{75}As $1/T_1$ NMR data with $1/T_1 \propto T^3$ from 50 to 300 K for $BaMn_2As_2$.

A MFT treatment of the J_1-J_2-J_c Heisenberg model was described in Sec. VII. In the paramagnetic state the system follows the Curie-Weiss law $C/(T + \theta)$ for $T \geqslant \theta$, which has the same form as described in many textbooks for the J_1-only model. The ratio f of the Weiss temperature θ to T_N, $f = \theta/T_N$, is found to be $f = 1$ for $J_2 = 0$, as expected for a bipartite spin lattice, but is $f > 1$ for frustrating AF $J_2 > 0$ and is $f < 1$ for nonfrustrating reinforcing FM $J_2 < 0$, which are intrasublattice interactions so the spin lattice is no longer bipartite. Thus, for $J_2 > 0$, the Curie-Weiss law continues to be followed below $T = \theta$ down to $T = T_N$, a characteristic already noted by Ramirez for geometrically frustrated antiferromagnets.[35] As shown in Fig. 8, we find that $\chi_\parallel(T)$ for $T < T_N$ strongly depends on J_2, whereas $\chi_\perp$ is independent of T and J_2 at $T < T_N$, apart from the implicit influence of J_2 on T_N. We further find that the staggered moment and the magnetic heat capacity versus T/T_N at $T < T_N$ are also independent of J_2, again apart from the implicit influence of J_2 on T_N.

We carried out QMC and CMC simulations of both $\chi(T)$ and the magnetic heat capacity $C_{mag}(T)$ in $H = 0$ versus J_c/J_1 and J_2/J_1. Most of the QMC simulations were for $J_2 = 0$ due to severe negative sign problems when J_2 was taken to be positive, which is antiferromagnetic and frustrating for G-type AF order. When we replaced the square of the spin, S^2, in the CMC simulations by the quantum mechanical expectation value $S(S + 1)$, the QMC simulations for $J_2 = 0$ for increasing S merged smoothly with the CMC simulation (which corresponds to $S \to \infty$) as shown in Fig. 23, so we used the CMC simulations to fit the experimental $\chi(T)$ data for $T > T_N$. The CMC simulations of $C_{mag}(T)$ as a function of J_c showed AF phase transitions at temperatures T_N that increased with $J_c > 0$ but decreased with $J_2 > 0$, as shown in Fig. 22. The $T_N(J_c, J_2)$ data are well fitted by Eq. (96).

We also carried out band-theoretical estimates of the exchange couplings in $BaMn_2As_2$. There are two generic ways to do this. The first is to take the differences between the total energies for different spin configurations such as in Eqs. (119)–(121), where the lowest energy spin configuration is the ground state. This method is often used to determine exchange constants to be used in the calculation of magnetic transition temperatures and yields the exchange constants in rows 5 and 6 of Table IX, which are not further discussed. The second is to measure the change in the total energy due to small deviations of the spin directions from the magnetically ordered ground state via Eq. (117), which gives the exchange values in rows 9 and 10 of Table IX. These values are considered to be more reliable for comparison with values extracted from inelastic neutron scattering experiments.

Our exchange constants from the MFT fit to our anisotropic $\chi(T)$ data for $BaMn_2As_2$ below T_N in Fig. 28 and Table VIII are probably not reliable because that fit assumes that $\chi(T)$ follows the Curie-Weiss law above T_N (i.e., that there are no two-spin AF correlations stronger than $1/T$ above T_N), which

TABLE XI. Summary of our most reliable exchange constants in BaMn$_2$As$_2$ obtained from band theory and from fitting our experimental data by our predictions of the J_1-J_2-J_c Heisenberg model. The notation "$\equiv$" means that the value that follows it was assumed, not fitted. Two spin values for the neutron fit are listed because the neutron fit gives the product of the spin S and the respective exchange constant, not the two separately. For the χ fit, a range of spin values can fit the data. We chose two spin values close to 2 and 5/2, corresponding to $J_2/J_1 = 0.2$ and 0.4, respectively. Two band theory estimates were obtained using the LDA and the GGA, as noted.

Data	S	J_1 (meV)	J_2/J_1	J_c/J_1
Neutrons	2	16.5 ± 1.5	0.29 ± 0.05	0.09 ± 0.02
	5/2	13.2 ± 1.2	0.29 ± 0.05	0.09 ± 0.02
$\chi(T > T_N)$	2.06	17.8	$\equiv 0.2$	$\equiv 0.1$
	2.64	18.1	$\equiv 0.4$	$\equiv 0.1$
^{75}As NMR	$\equiv 2$	14	$\equiv 0.29$	$\equiv 0.09$
($T \ll T_N$)				
Band theory				
LDA	1.65	13.1	0.21	0.08
GGA	1.8	12.6	0.21	0.08

is strongly violated by the data in Fig. 7(a). Similarly, although our fits by MFT to the ordered moment $\bar{\mu}_z(T)$ from neutron diffraction measurements[13] on BaMn$_2$As$_2$ in Fig. 14 and to the heat capacity $C_p(T)$ (Ref. 11) in Fig. 15 are reasonable, they are not sufficient to distinguish between the possible spins $S = 2$ and $S = 5/2$ discussed above. Furthermore, the fit to the $C_p(T)$ data near room temperature by the sum of the Debye lattice heat capacity and the MFT prediction of the magnetic heat capacity indicated that the measured magnetic heat capacity is too low. This discrepancy suggests the presence of strong AF fluctuations above T_N that reduce the magnetic entropy and magnetic heat capacity below T_N, consistent with the behavior of the magnetic susceptibility above T_N in Fig. 28. The calculated T^3 contribution to the heat capacity at low temperatures from spin waves, without an anisotropy gap in the spin wave spectrum, is about 40% of the measured value. However, an anisotropy gap would suppress the spin wave contribution exponentially to zero at low temperatures.

We have gathered together in Table XI our most reliable exchange constants in BaMn$_2$As$_2$ from our band theory calculations and from the theoretical fits to our experimental data by the J_1-J_2-J_c Heisenberg model. Several features are noteworthy. First, all three exchange constants are consistently positive (antiferromagnetic). Second, the estimates give similar values of $J_1 \approx 13$–18 meV for S values in the range from 2 to 5/2. For the susceptibility fits, nearly the same J_1 was obtained from the two fits despite the significant differences between the respective S and J_2/J_1 values. Third, the estimates of J_2/J_1 from band theory and from analysis of the neutron and magnetic susceptibility measurements are in the range 0.2–0.4, which are below the value of 0.5 at which the in-plane G-type AF order would classically become unstable with respect to the stripe-AF order [see Fig. 2 and Eq. (4)], and are therefore consistent with the observed G-type AF order. From our classical Monte Carlo simulations of the heat capacity of stacked square lattice layers, the exchange parameters from the neutron

scattering fit predict $T_N \approx 640$ K if the Mn spin is $S = 5/2$, in close agreement with the experimental value of ≈ 625 K.

Finally, with the above range of exchange parameters, our second-order spin wave calculations in Sec. XIII show that the ordered moment reduction due to quantum fluctuations alone is at least $\sim 0.4 \mu_B$/Mn. Because the measured ordered moment is $\langle \mu \rangle = 3.9(1) \mu_B$/Mn, this argues against assigning a spin $S = 2$ to the Mn^{2+} ions which gives $\langle \mu \rangle = gS\mu_B = 4 \mu_B$/Mn and favors $S = 5/2$ for which one would obtain $\langle \mu \rangle = 5 \mu_B$/Mn for $g = 2$ in the absence of quantum fluctuations. The additional reduction needed to reach the experimental value is likely due to charge and/or magnetic moment amplitude fluctuations which arise from both on-site and intersite interactions, and/or from hybridization effects, consistent with the reduced ordered moment measured for other Mn^{2+} compounds.[14,15,82,83] This effect cannot be described in the Heisenberg model formalism used in this paper. For instance, in Sec. XII we discussed that despite the large moment of the Mn, the magnitude of the magnetic moment can vary by $\sim 20\%$ depending on the specific magnetic configuration, suggesting that amplitude fluctuations of the magnetic moment may indeed be relevant.

As noted in the Introduction, the view that BaFe$_2$As$_2$ is an itinerant antiferromagnet is not universally held. Furthermore, the results of many magnetic inelastic neutron scattering measurements on BaFe$_2$As$_2$ have been analyzed in terms of local moment Heisenberg models, even when the authors of this modeling believe that the itinerant model is valid. The reason for this latter analysis, as has been stressed in the literature, is that the magnetism of itinerant models can often be parametrized by local moment Heisenberg models. Further review and discussion of this issue is given in Ref. 4.

We therefore now compare the exchange constants in BaMn$_2$As$_2$ with those in the isostructural (at room temperature) high-T_c AFe$_2$As$_2$ parent compounds ($A = $ Ca, Sr, Ba) within the context of the J_1-J_2-J_c local moment Heisenberg model. The AFe$_2$As$_2$ compounds order into an in-plane stripe-type antiferromagnetic structure below ~ 200 K (lower panel of Fig. 2) and the lattice distorts to orthorhombic symmetry at or above T_N.[4] Within the orthorhombic structure and assuming $S = 1/2$ and $gS\mu_B \approx 1 \mu_B$, one defines the average $\langle J_1 \rangle = (J_{1a} + J_{1b})/2$, yielding $\langle J_1 \rangle / J_2 = 0.7$–1.4 for a variety of AFe$_2$As$_2$ compounds,[4] which is in the regime $\langle J_1 \rangle / J_2 < 2$ expected for in-plane stripe-type ordering [see Eq. (4)]. These values can be compared with those for BaMn$_2$As$_2$ in Table XI, where $J_1/J_2 \sim 3$. In BaMn$_2$As$_2$ and also in the AFe$_2$As$_2$ compounds, the interlayer coupling J_c is weak compared to the in-plane couplings and the systems should be considered to have strongly spatially anisotropic exchange, but not necessarily two-dimensional. Thus, the AT_2As$_2$ systems, where T is a 3d-transition metal element, appear to be ideal systems to study the physics of the J_1-J_2-J_c Heisenberg model, including the possibility of tuning the system to and through the quantum critical point $J_1/J_2 = 2$ by doping. Indeed, doping-dependent studies of Ba(Fe$_{1-x}$Cr$_x$)$_2$As$_2$ have recently revealed a transition from stripe-type AF order to G-type AF order at $x \approx 0.3$,[85] and studies of Ba(Fe$_{1-x}$Mn$_x$)$_2$As$_2$ have revealed a transition to a new state, possibly due to competition between G-type and stripe-type AF ordering, at $x \approx 0.1$.[86]

APPENDIX A: HIGH-TEMPERATURE SERIES EXPANSIONS

From quite general considerations, one can show that the results of MFT at high temperatures for the magnetic susceptibility (the Curie-Weiss law) is an exact result arising from a quantum mechanical treatment of local moment magnetism using a high-temperature series expansion HTSE. We also discuss a complementary "Curie-Weiss law" for the magnetic heat capacity at high temperatures, which is useful when discussing our Monte Carlo simulations of the magnetic heat capacity in Sec. IX.

1. Magnetic susceptibility and the Curie-Weiss law

Using the fluctuation-dissipation theorem, one can express the diagonal $\alpha\alpha$ components χ_α ($\alpha = x, y, z$) of the magnetic susceptibility tensor in terms of the two-spin correlation functions,

$$\Gamma_{\mathbf{r}}^\alpha \equiv \langle S_{\mathbf{0}}^\alpha S_{\mathbf{r}}^\alpha \rangle, \tag{A1}$$

where $\mathbf{r}$ is the distance measured in the number n of bonds, including zero, of spin $S_{\mathbf{r}}$ from a typical central spin $S_{\mathbf{0}}$.[6,32] In the isotropic Heisenberg model, one obtains[32]

$$\chi = \frac{Ng^2\mu_B^2}{k_B T} \sum_{\mathbf{r}} \Gamma_{\mathbf{r}}^z. \tag{A2}$$

If one only considers the single-spin autocorrelation function ($\mathbf{r} = 0$), then one has $\Gamma_0^z = \langle S_z^2 \rangle = \langle S^2 \rangle / 3 = S(S+1)/3$, which gives the Curie law

$$\chi = \frac{Ng^2\mu_B^2 S(S+1)}{3k_B T}, \tag{A3}$$

which in turn is the Curie-Weiss law (22) with $\theta = 0$ and Curie constant (23).

Writing $r \equiv n = 0, 1, 2, \ldots$, in terms of the distance of a spin in number of bonds from the central spin at position $\mathbf{0}$ (i.e., n means the nth-nearest neighbor of the spin at the origin in terms of the minimum number of bonds between them), one can express the temperature dependences of the two-spin correlation functions as high-temperature series expansions in $1/T$ with the general form

$$\Gamma_n^z = \frac{\Gamma_{n,n}^z}{(k_B T/J)^n} + \frac{\Gamma_{n,n+1}^z}{(k_B T/J)^{n+1}} + \cdots, \tag{A4}$$

where $\Gamma_0^z = S(S+1)/3$, as noted above, and the lowest-order term for a given Γ_n^z is $1/T^n$.[32] Substituting the first three terms of Eq. (A4) into Eq. (A2) gives

$$\begin{aligned}
\chi &= \frac{Ng^2\mu_B^2}{k_B T} \left[\frac{S(S+1)}{3} + \frac{\Gamma_{1,1}^z}{k_B T/J} + \frac{\Gamma_{1,2}^z + \Gamma_{2,2}^z}{(k_B T/J)^2} + \cdots \right] \\
&= \frac{C}{T} \left[1 + \frac{3}{S(S+1)} \left(\frac{\Gamma_{1,1}^z}{k_B T/J} + \frac{\Gamma_{1,2}^z + \Gamma_{2,2}^z}{(k_B T/J)^2} + \cdots \right) \right],
\end{aligned} \tag{A5}$$

where the Curie constant C is the same as in Eq. (23). If one keeps only the first two terms in the square brackets and uses the Taylor series expansion $1 + x \approx 1/(1-x)$ for small x to put the quantity in square brackets into the denominator, one gets the Curie-Weiss law (22) with Weiss temperature

$$\theta = -\frac{3\Gamma_{1,1}^z J}{S(S+1)k_B}. \tag{A6}$$

Comparing Eqs. (25) and (A6) gives the coefficient

$$\Gamma_{1,1}^z = -\frac{z[S(S+1)]^2}{9}. \tag{A7}$$

2. The HTSE for the magnetic heat capacity

We discussed above that the Curie-Weiss law for the magnetic susceptibility of equivalent spins is rigorously derived from the first $(1/T)$ term in the HTSE of the nearest-neighbor two-spin correlation function and hence does not depend on the particular crystal structure or spin-lattice dimensionality. This suggests that there is an analogous term in the HTSE of the magnetic heat capacity C_{mag}. We show this to be the case [Eq. (A9)] and apply the result in Sec. IX.

From Hamiltonian (21), the thermal-average magnetic configuration energy in zero field only depends on the nearest-neighbor two-spin correlation function as[32]

$$E_{\mathrm{mag}}(T) = \tfrac{1}{2} N z J \langle \mathbf{S}_0 \cdot \mathbf{S}_1 \rangle_{\mathrm{T}}(T), \tag{A8}$$

where the factor of $1/2$ is introduced to avoid double counting the distinct AF NN bonds and $\langle \cdots \rangle_{\mathrm{T}}$ denotes a thermal average of the quantum mechanical expectation value. The magnetic specific heat $C_{\mathrm{mag}}(T)$ is obtained by differentiating Eq. (A8) with respect to T. Thus, the first $1/T$ HTSE term of $E_{\mathrm{mag}}(T)$ gives the first term in the HTSE of $C_{\mathrm{mag}}(T)$ as a $1/T^2$ term.

Rushbrooke and Wood showed that the first six terms of the HTSE of $\chi(T)$ and $C_{\mathrm{mag}}(T)$ of a Heisenberg spin lattice containing equivalent spins S can be expressed in terms of the identical NN exchange couplings J and the bond connectivity ("lattice parameters") of the specific spin lattice.[33] With respect to the present discussion, they found that the first $(1/T^2)$ term of the HTSE for $C_{\mathrm{mag}}(T)$ is independent of the type of spin lattice and of the spin lattice dimensionality and only depends on z, S, and J according to[33]

$$\frac{C_{\mathrm{mag}}}{R} = \frac{z}{6} \left[\frac{JS(S+1)}{k_B T} \right]^2. \tag{A9}$$

This term is the same for FM and AF interactions because the exchange constant is squared, which gives a positive-definite result for $C_{\text{mag}}(T)$. Thus, when comparing calculated $C_{\text{mag}}(T)$ data for lattices with the same coordination number z but different exchange constants and/or spins, a universal high-temperature behavior is obtained if the data are scaled according to

$$\frac{C_{\text{mag}}}{R} \quad \text{versus} \quad \frac{k_{\text{B}}T}{J S(S+1)}. \tag{A10}$$

The Curie law for the magnetic susceptibility arises because there is a nonzero susceptibility for isolated spins. This is modified at high temperatures by the addition of a $1/T^2$ term in Eq. (A5) arising from spin interactions, yielding a Curie-Weiss law with nonzero Weiss temperature θ. On the other hand, the magnetic heat capacity of isolated spins is zero, and hence there is no equivalent Curie law for $E_{\text{mag}}(T)$ or $C_{\text{mag}}(T)$: the values are just zero. Equation (A9) can therefore be considered to be a "Curie-Weiss law" for $C_{\text{mag}}(T)$.

APPENDIX B: ANISOTROPIC SUSCEPTIBILITY BELOW T_{N} FOR THE J_2-J_2-J_c MODEL IN MOLECULAR FIELD THEORY

1. Perpendicular susceptibility $\chi_\perp$ below T_{N}

Setting the external field H to zero and using the exchange fields in Eq. (29), the average exchange energy of the spin system is

$$E_{\text{exch}} = -\mathbf{M}_1 \cdot \mathbf{B}_1 = -\left(\lambda_{\text{s}} M_1^2 + \lambda_{\text{d}} \mathbf{M}_1 \cdot \mathbf{M}_2\right). \tag{B1}$$

We do not add a second term $-\mathbf{M}_2 \cdot \mathbf{B}_2$ to this, because that would double count the exchange interactions between the spins which occur *pairwise*.

We apply an external magnetic field $\mathbf{H}_\perp$ that is perpendicular to the ordered moment direction in the antiferromagnetically ordered state that induces a perpendicular magnetization $\mathbf{M}_\perp$ in the sample, where $\mathbf{M}_\perp = \mathbf{M}_1 + \mathbf{M}_2$ is the vector sum of the sublattice magnetizations. From Fig. 33, the angle ϕ between $\mathbf{M}_1$ and $\mathbf{M}_2$ is

$$\cos\phi = \cos(180° - 2\gamma) = -\cos(2\gamma) \approx -(1 - 2\gamma^2),$$

where we used $\cos(A - B) = \cos A \cos B + \sin A \sin B$ and on the right-hand side we used the small angle approximation $\cos x \approx 1 - x^2/2$. We assume that γ is very small because $\chi_\perp = \lim_{H_\perp \to 0} M_\perp / H_\perp$ by definition. Thus, the exchange energy in Eq. (B1) becomes

$$E_{\text{exch}} = M_i^2[-\lambda_{\text{s}} + \lambda_{\text{d}}(1 - 2\gamma^2)], \tag{B2}$$

where $M_1 = M_2 \equiv M_i$.

A perpendicular magnetic field $\mathbf{H}_\perp = H_\perp \hat{\mathbf{i}}$ causes the ordered AF spin sublattices to tilt toward the applied field direction, away from the ordered moment z direction, as shown in Fig. 33. The magnetic energy due to the perpendicular field is

$$E_\perp = -2\mathbf{M}_i \cdot \mathbf{H}_\perp = -2M_i H_\perp \sin\gamma \approx -2M_i H_\perp \gamma, \tag{B3}$$

where we have used the small-angle approximation $\sin x \approx x$. Thus, the total magnetic energy is

$$E = E_{\text{exch}} + E_\perp = M_i^2[-\lambda_{\text{s}} + \lambda_{\text{d}}(1 - 2\gamma^2)] - 2M_i H_\perp \gamma. \tag{B4}$$
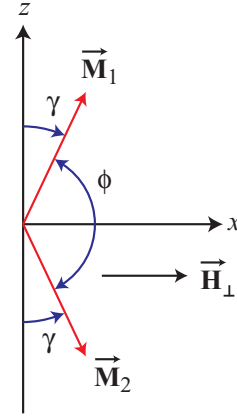

FIG. 33. (Color online) Influence of a perpendicular magnetic field $\mathbf{H}_\perp$ on the sublattice magnetizations of an ordered antiferromagnet. The $\mathbf{H}_\perp$ tilts the ordered sublattice magnetizations $\mathbf{M}_1$ and $\mathbf{M}_2$ that are initially pointed along the z axis by an angle γ toward the applied field $\mathbf{H}_\perp$ along the x axis. The angle γ is greatly exaggerated for clarity.

The stable configuration minimizes the energy. Taking the derivative of E with respect to γ and setting it to zero and setting $\lambda_{\text{d}} = -|\lambda_{\text{d}}|$ because λ_{d} is negative gives

$$\gamma = \frac{H_\perp}{2|\lambda_{\text{d}}|M_i}.$$

Thus, the interactions within the same sublattice (λ_{s}, i.e., J_2) have no influence on this equilibrium condition. The equilibrium value of the component $M_\perp$ of the total magnetization in the direction of $\mathbf{H}_\perp$, using the small-angle approximation $\sin\theta \approx \theta$, is

$$M_\perp = 2M_i \sin\gamma \approx 2M_i\gamma = \frac{H_\perp}{|\lambda_{\text{d}}|},$$

which gives the perpendicular susceptibility as

$$\chi_\perp = \frac{M_\perp}{H_\perp} = \frac{1}{|\lambda_{\text{d}}|}.$$

Note that M_i and hence also its temperature dependence have dropped out, so that $\chi_\perp$ in this treatment is independent of T below T_{N}.

From Eqs. (54) we have

$$|\lambda_{\text{d}}| = \frac{T_{\text{N}}(1 + f)}{C}. \tag{B5}$$

Thus, we obtain

$$\chi_\perp = \frac{1}{|\lambda_{\text{d}}|} = \frac{C}{T_{\text{N}}(1 + f)} = \frac{C}{T_{\text{N}} + \theta} = \chi(T_{\text{N}}) \quad (T \leqslant T_{\text{N}}),$$

which is Eq. (55) in the text. Although J_2 is not present explicitly, its influence is expressed through the implicit dependence of T_{N} on J_2.

2. Parallel susceptibility $\chi_\parallel$ below T_{N}

Here again we assume that the susceptibility in the absence of explicit exchange couplings is $\chi_0 = C/T$, which is isotropic above T_{N}. We apply a small magnetic field H. Below T_{N} a large exchange field develops as seen by each sublattice because

of the ordered moments. Therefore, we must use a Brillouin function to describe the magnetization of each sublattice.

The saturation magnetic moment of a spin S is

$$\mu_{\text{sat}} = g\mu_{\text{B}}S.$$

For N spins, the saturation magnetization is therefore

$$M_{\text{sat}} = NgS\mu_{\text{B}}. \tag{B6}$$

The magnetization of the N spins is written

$$M_z = M_{\text{sat}}B_S(y), \tag{B7}$$

where $B_S(y)$ is the Brillouin function given by

$$B_S(y) = \frac{1}{2S}\left\{(2S+1)\coth\left[(2S+1)\frac{y}{2}\right] - \coth\left(\frac{y}{2}\right)\right\}, \tag{B8}$$

where $0 \leqslant B_S(y) \leqslant 1$ for $y \geqslant 0$,

$$y = \frac{g\mu_{\text{B}}H}{k_{\text{B}}T}, \tag{B9}$$

and the g factor is usually set to the value $g = 2$.

In MFT, we replace H in the Brillouin function by the magnetic inductions B_i in Eqs. (28) and (29), which include the exchange fields. Thus, we have

$$\begin{aligned} M_1 &= \frac{1}{2}M_{\text{sat}}B_S\left(\frac{g\mu_{\text{B}}B_1}{k_{\text{B}}T}\right) \\ &= \frac{1}{2}M_{\text{sat}}B_S\left[\frac{g\mu_{\text{B}}(H + \lambda_{\text{s}}M_1 + \lambda_{\text{d}}M_2)}{k_{\text{B}}T}\right], \\ M_2 &= \frac{1}{2}M_{\text{sat}}B_S\left(\frac{g\mu_{\text{B}}B_2}{k_{\text{B}}T}\right) \\ &= \frac{1}{2}M_{\text{sat}}B_S\left[\frac{g\mu_{\text{B}}(H + \lambda_{\text{d}}M_1 + \lambda_{\text{s}}M_2)}{k_{\text{B}}T}\right]. \end{aligned} \tag{B10}$$

Substituting for λ_{s} and λ_{d} from Eqs. (54) gives

$$\begin{aligned} \frac{M_1}{M_{\text{sat}}} &= \frac{1}{2}B_S\left\{\frac{g\mu_{\text{B}}\left[H - \frac{T_{\text{N}}(f-1)}{C}M_1 - \frac{T_{\text{N}}(f+1)}{C}M_2\right]}{k_{\text{B}}T}\right\}, \\ \frac{M_2}{M_{\text{sat}}} &= \frac{1}{2}B_S\left\{\frac{g\mu_{\text{B}}\left[H - \frac{T_{\text{N}}(f+1)}{C}M_1 - \frac{T_{\text{N}}(f-1)}{C}M_2\right]}{k_{\text{B}}T}\right\}. \end{aligned} \tag{B11}$$

To simplify the notation and the solution to Eqs. (B11) we define reduced magnetic field, temperature, and ordered moment variables, respectively, by

$$\begin{aligned} \tilde{h} &= \frac{g\mu_{\text{B}}H}{k_{\text{B}}T_{\text{N}}(H=0)}, \quad t = \frac{T}{T_{\text{N}}(H=0)}, \\ \bar{\mu}_{iz} &= \frac{\mu_{iz}}{\mu_{\text{sat}}} = \frac{\mu_{iz}}{gS\mu_{\text{B}}}. \end{aligned} \tag{B12}$$

Then using $M_i = N\mu_{iz}/2$ and $M_{\text{sat}} = N\mu_{\text{sat}} = NgS\mu_{\text{B}}$ and the expression for the Curie constant C in Eqs. (23), Eqs. (B11) become

$$\begin{aligned} \bar{\mu}_{1z} &= B_S\left[\frac{\tilde{h}}{t} - \frac{3(f-1)}{2(S+1)}\frac{\bar{\mu}_{1z}}{t} - \frac{3(f+1)}{2(S+1)}\frac{\bar{\mu}_{2z}}{t}\right], \\ \bar{\mu}_{2z} &= B_S\left[\frac{\tilde{h}}{t} - \frac{3(f+1)}{2(S+1)}\frac{\bar{\mu}_{1z}}{t} - \frac{3(f-1)}{2(S+1)}\frac{\bar{\mu}_{2z}}{t}\right]. \end{aligned} \tag{B13}$$

For specified S, f, $\tilde{h}$, and t, one can solve these two simultaneous equations numerically for $\bar{\mu}_{1z}(t,\tilde{h})$ and $\bar{\mu}_{2z}(t,\tilde{h})$. The average reduced magnetization per spin is

$$\bar{\mu}_z(t,\tilde{h}) = \frac{1}{2}[\bar{\mu}_{1z}(t,\tilde{h}) + \bar{\mu}_{2z}(t,\tilde{h})]. \tag{B14}$$

This solution is valid in both the paramagnetic and antiferromagnetic states. The reduced parallel susceptibility per spin is

$$\tilde{\chi}(t) = \lim_{\tilde{h}\to 0}\frac{\bar{\mu}_z(t,\tilde{h})}{\tilde{h}}. \tag{B15}$$

In the AF phase, the order parameter is the staggered ordered moment

$$\bar{\mu}_z^{\dagger} = \frac{\bar{\mu}_{1z} - \bar{\mu}_{2z}}{2}, \tag{B16}$$

which is one-half the difference between the z components of the ordered moments of the two sublattices. The term "ordered moment," when used in the context of a collinear antiferromagnet, is the staggered moment.

The susceptibility is isotropic at T_{N} (at reduced temperature $t = 1$). Therefore, setting $t = 1$ and $\bar{\mu}_{1z} = \bar{\mu}_{2z}$ in Eqs. (B13) gives

$$\bar{\mu}_{iz} = B_S\left[\tilde{h} - \frac{3f}{S+1}\bar{\mu}_{iz}\right],$$

where $i = 1,2$. Using the expansion $B_S(y) = (S+1)y/3$ for $y \ll 1$ and solving for $\bar{\mu}_{iz}$ gives

$$\bar{\mu}_{iz}(t=1) = \frac{S+1}{3(f+1)}\tilde{h}. \tag{B17}$$

Then Eq. (B15) gives

$$\frac{\chi_{\parallel}(T)}{\chi_{\parallel}(T_{\text{N}})} = \frac{\tilde{\chi}_{\parallel}(t)}{\tilde{\chi}_{\parallel}(t=1)} = \frac{3(f+1)}{S+1}\lim_{\tilde{h}\to 0}\frac{\bar{\mu}_z(t,\tilde{h})}{\tilde{h}}. \tag{B18}$$

APPENDIX C: ORDERED MOMENT VERSUS TEMPERATURE BELOW T_{N}

In the AF state, setting the applied magnetic field $\tilde{h} = 0$ and the ordered moment $\bar{\mu}_{2z}(t) = -\bar{\mu}_{1z}(t)$ in the first of Eqs. (B13) gives the simple result

$$\bar{\mu}_z^{\dagger}(t) = B_S\left[\left(\frac{3}{S+1}\right)\frac{\bar{\mu}_z^{\dagger}(t)}{t}\right]. \tag{C1}$$

Thus, the reduced exchange field as in Eqs. (28) and (29) is

$$\tilde{h}_{\text{exch}}(t) = \frac{3}{S+1}\bar{\mu}_z^{\dagger}(t). \tag{C2}$$

APPENDIX D: ZERO-FIELD MAGNETIC HEAT CAPACITY C_{mag} BELOW T_{N}

In the presence of the staggered exchange field with z components $H_{1\,\text{exch}} = -H_{2\,\text{exch}}$ and nonzero $\mu_{1z} = -\mu_{2z}$, the energy of a collinear G-type AF system in zero applied field is

$$E_{\text{ave}} = -\frac{N}{2}\mu_{1z}H_{1\,\text{exch}} = -\frac{1}{2}M_{1z}H_{1\,\text{exch}}, \tag{D1}$$

where the factor of $1/2$ is included to avoid counting each magnetic moment twice (once in μ_{1z} or M_{1z} and again in

$H_{1\,\text{exch}}$). The exchange field seen by sublattice 1 can be written using Eqs. (29) and (42) as

$$H_{1\,\text{exch}} = (\lambda_s - \lambda_d)M_{1z} = \frac{3k_B T_N}{g^2 \mu_B^2 S(S+1)}\mu_{1z}. \quad \text{(D2)}$$

Then using the expression for the saturation moment $\mu_{\text{sat}} = gS\mu_B$, one can rewrite this as

$$H_{1\,\text{exch}} = \left(\frac{3k_B T_N S}{S+1}\right)\frac{\mu_{1z}}{\mu_{\text{sat}}^2}. \quad \text{(D3)}$$

Inserting Eq. (D3) into (D1) gives

$$E_{\text{ave}}(T) = -\frac{3Nk_B T_N S}{2(S+1)}\left[\frac{\mu_{1z}(T)}{\mu_{\text{sat}}}\right]^2. \quad \text{(D4)}$$

Using the dimensionless reduced variables introduced in Eqs. (B12) and the definition (B16) of the staggered moment, we obtain

$$E_{\text{ave}}(t) = -\frac{3Nk_B T_N S}{2(S+1)}(\bar{\mu}_z^\dagger)^2(t). \quad \text{(D5)}$$

By setting N equal to Avogadro's number N_A and using the definition of the molar gas constant $R = N_A k_B$ one obtains from Eq. (D5) the molar magnetic energy

$$E_{\text{ave}}(t) = -\frac{3RT_N S}{2(S+1)}(\bar{\mu}_z^\dagger)^2(t). \quad \text{(D6)}$$

The molar magnetic heat capacity is then

$$\frac{C_{\text{mag}}(t)}{R} = \frac{1}{RT_N}\frac{dE_{\text{ave}}(t)}{dt} = -\frac{3S}{S+1}\bar{\mu}_z^\dagger(t)\frac{d\bar{\mu}_z^\dagger(t)}{dt}. \quad \text{(56)}$$

APPENDIX E: LOW-TEMPERATURE HEAT CAPACITY OF SPIN WAVES

At low temperatures, only the lowest energy spin waves contribute to the heat capacity, so we can use generic Eq. (7) for the dispersion relation. To evaluate the integrals in Eq. (69), we change variables in the integrals from wave vector **q** to the vector $\vec{\epsilon}$ with dimensions of energy and with components

$$
\begin{aligned}
\epsilon_x &= \hbar v_x q_x, \quad \epsilon_a = \hbar v_x \pi/a, \\
\epsilon_y &= \hbar v_y q_y, \quad \epsilon_b = \hbar v_y \pi/b, \\
\epsilon_z &= \hbar v_z q_z, \quad \epsilon_c = \hbar v_z \pi/c.
\end{aligned}
\quad \text{(E1)}
$$

Now the dispersion relation (7) is written symmetrically as

$$E_{\vec{\epsilon}} = \hbar\omega_{\vec{\epsilon}} = \sqrt{\epsilon_x^2 + \epsilon_y^2 + \epsilon_z^2} \equiv \epsilon \quad \text{(E2)}$$

and Eq. (69) becomes

$$
\begin{aligned}
E_{\text{ave}} = &\frac{NV_{\text{spin}}}{(2\pi)^3 \hbar^3 v_x v_y v_z} \\
&\times \int_{-\epsilon_a}^{\epsilon_a} d\epsilon_x \int_{-\epsilon_b}^{\epsilon_b} d\epsilon_y \int_{-\epsilon_c}^{\epsilon_c} d\epsilon_z \frac{E_{\vec{\epsilon}}}{e^{E_{\vec{\epsilon}}/k_B T} - 1},
\end{aligned}
\quad \text{(E3)}
$$

in which the anisotropy in the dispersion relation (7) has been moved to anisotropies in the limits of integration and in the prefactor.

At low temperatures, only the lowest energy spin wave states are populated, so we can take the limits of each integral

to be $-\infty$ to ∞, which also eliminates the anisotropy between the limits of integration of the three integrals. We can then convert the integrals over the three Cartesian coordinates to an integral over radius in spherical coordinates according to $E_{\vec{\epsilon}} \to \epsilon$ and

$$\int_{-\infty}^{\infty} d\epsilon_x \int_{-\infty}^{\infty} d\epsilon_y \int_{-\infty}^{\infty} d\epsilon_z \to 4\pi \int_0^{\infty} d\epsilon\,\epsilon^2.$$

Now we will integrate only about the Γ point, so we must multiply by two to take into account the low-energy spin wave branches at the corners of the Brillouin zone of the primitive tetragonal direct lattice as discussed in the text. We then obtain

$$E_{\text{ave}} = \frac{NV_{\text{spin}}}{\pi^2 \hbar^3 v_x v_y v_z}\int_0^{\infty}\frac{\epsilon^3}{e^{\epsilon/k_B T} - 1}\,d\epsilon \quad \text{(low } T\text{)}. \quad \text{(E4)}$$

Changing variables in the integral to $x = \epsilon/k_B T$ gives

$$E_{\text{ave}} = \frac{NV_{\text{spin}}(k_B T)^4}{\pi^2 \hbar^3 v_x v_y v_z}\int_0^{\infty}\frac{x^3}{e^x - 1}\,dx \quad \text{(low } T\text{)}. \quad \text{(E5)}$$

The integral is $\pi^4/15$, yielding

$$E_{\text{ave}} = \frac{\pi^2 N V_{\text{spin}}(k_B T)^4}{15\hbar^3 v_x v_y v_z} \quad \text{(low } T\text{)}. \quad \text{(E6)}$$

Then setting $N = N_A$ (Avogadro's number), the magnetic heat capacity due to the spin waves per mole of spins is

$$\frac{C_{\text{mag}}}{R} = \frac{1}{R}\frac{dE_{\text{ave}}}{dT} = \left(\frac{4\pi^2 k_B^3 V_{\text{spin}}}{15\hbar^3 v_x v_y v_z}\right)T^3 \quad (T \ll T_N), \quad \text{(73)}$$

where $R = N_A k_B$ is the molar gas constant.

We now calculate the two-dimensional spin wave theory prediction of C_{mag} to check consistency with Eq. (101) that was derived using chiral perturbation theory. In two dimensions (i.e., $J_c = 0$), the area of the sample is $A = Na^2$, where N is the number of spins and $ab = a^2$ is the area of the square unit cell which contains one spin in its basis. Then Eq. (69) is replaced by

$$E_{\text{ave}} = \frac{1}{\frac{(2\pi)^2}{Na^2}}\int_{-\pi/a}^{\pi/a} dq_x \int_{-\pi/b}^{\pi/b} dq_y \frac{\hbar\omega_{\mathbf{q}}}{e^{\hbar\omega_{\mathbf{q}}/k_B T} - 1}. \quad \text{(E7)}$$

Following the same steps as for the three-dimensional case above, converting the two-dimensional integrals to polar coordinates according to

$$\int_{-\infty}^{\infty} d\epsilon_x \int_{-\infty}^{\infty} d\epsilon_y \to 2\pi \int_0^{\infty} d\epsilon\,\epsilon,$$

and multiplying by two to take into account the spin wave excitations at the corners of the Brillouin zone, gives

$$\frac{C_{\text{mag}}}{R} = \frac{6\zeta(3)}{\pi(\hbar v/a)^2}(k_B T)^2, \quad \text{(E8)}$$

where v is the isotropic spin wave velocity in the ab plane and we have used $\int_0^{\infty}\frac{x^2}{e^x - 1}dx = 2\zeta(3)$. Equation (E8) is identical to Eq. (101) obtained for the isotropic Heisenberg square lattice from chiral perturbation theory.[52]

*Present address: Indian Institute of Science Education and Research Trivandrum, CET Campus, Trivandrum-695016, Kerala, India.

†Present address: Indian Institute of Science Education and Research Mohali, MGSIPAP Complex, Sector 26, Chandigarh 160019, India.

[1] Y. Kamihara, T. Watanabe, M. Hirano, and H. Hosono, J. Am. Chem. Soc. **130**, 3296 (2008).

[2] C. Wang, L. Li, S. Chi, Z. Zhu, Z. Ren, Y. Li, Y. Wang, X. Lin, Y. Luo, S. Jiang, X. Xu, G. Cao, and Z. Xu, Europhys. Lett. **83**, 67006 (2008).

[3] M. Rotter, M. Tegel, and D. Johrendt, Phys. Rev. Lett. **101**, 107006 (2008).

[4] For a review, see D. C. Johnston, Adv. Phys. **59**, 803–1061 (2010).

[5] J. G. Bednorz and K. A. Müller, Z. Phys. B **64**, 189 (1986).

[6] For a review, see D. C. Johnston, in *Handbook of Magnetic Materials*, edited by K. H. J. Buschow (Elsevier, Amsterdam, 1997), Vol. 10, Chap. 1, pp. 1–237.

[7] L. Gao, Y. Y. Xue, F. Chen, Q. Xiong, R. L. Meng, D. Ramirez, C. W. Chu, J. H. Eggert, and H. K. Mao, Phys. Rev. B **50**, 4260 (1994).

[8] For a review, see M. D. Lumsden and A. D. Christianson, J. Phys.: Condens. Matter **22**, 203203 (2010).

[9] X. F. Wang, T. Wu, G. Wu, H. Chen, Y. L. Xie, J. J. Ying, Y. J. Yan, R. H. Liu, and X. H. Chen, Phys. Rev. Lett. **102**, 117005 (2009).

[10] G. M. Zhang, Y. H. Su, Z. Y. Lu, Z. Y. Weng, D. H. Lee, and T. Xiang, Europhys. Lett. **86**, 37006 (2009).

[11] Y. Singh, A. Ellern, and D. C. Johnston, Phys. Rev. B **79**, 094519 (2009).

[12] J. An, A. S. Sefat, D. J. Singh, and M.-H. Du, Phys. Rev. B **79**, 075120 (2009).

[13] Y. Singh, M. A. Green, Q. Huang, A. Kreyssig, R. J. McQueeney, D. C. Johnston, and A. I. Goldman, Phys. Rev. B **80**, 100403(R) (2009).

[14] S. L. Brock, N. P. Raju, J. E. Greedan, and S. M. Kauzlarich, J. Alloys Compd. **237**, 9 (1996).

[15] R. Nath, V. O. Garlea, A. I. Goldman, and D. C. Johnston, Phys. Rev. B **81**, 224513 (2010).

[16] D. Schmalfuß, R. Darradi, J. Richter, J. Schulenburg, and D. Ihle, Phys. Rev. Lett. **97**, 157201 (2006).

[17] J. R. Viana, J. R. de Sousa, and M. A. Continentino, Phys. Rev. B **77**, 172412 (2008).

[18] W. A. Nunes, J. R. de Sousa, J. R. Viana, and J. Richter, J. Phys.: Condens. Matter **22**, 146004 (2010).

[19] D.-X. Yao and E. W. Carlson, Front. Phys. China **5**, 166 (2010).

[20] M. Holt, O. P. Sushkov, D. Stanek, and G. S. Uhrig, Phys. Rev. B **83**, 144528 (2011).

[21] K. Majumdar, J. Phys.: Condens. Matter **23**, 046001 (2011); **23**, 116004 (2011).

[22] O. Rojas, C. J. Hamer, and J. Oitmaa, e-print arXiv:1103.1679.

[23] D. Stanek, O. P. Sushkov, and G. S. Uhrig, Phys. Rev. B **84**, 064505 (2011).

[24] E. Brechtel, G. Cordier, and H. Schaefer, Z. Naturforsch. **34b**, 777 (1979).

[25] S. L. Brock and S. M. Kauzlarich, J. Alloys Compd. **241**, 82 (1996).

[26] M. Raczkowski and A. M. Oleś, Phys. Rev. B **66**, 094431 (2002).

[27] R. J. McQueeney, J. Q. Yan, S. Chang, and J. Ma, Phys. Rev. B **78**, 184417 (2008).

[28] J. Van Kranendonk and J. H. Van Vleck, Rev. Mod. Phys. **30**, 1 (1958).

[29] O. V. Kovalev, *Representations of the Crystallographic Space Groups* (Gordon and Breach, Langhorn, PA, 1993).

[30] P. J. Brown, in *International Tables for Crystallography*, edited by E. Prince (International Union of Crystallography, 2006), Vol. C, pp. 454–461.

[31] C. Kittel, *Introduction to Solid State Physics*, 4th ed. (Wiley, New York, 1966).

[32] M. E. Fisher, Philos. Mag. **7**, 1731 (1962).

[33] G. S. Rushbrooke and P. J. Wood, Mol. Phys. **1**, 257 (1958).

[34] G. S. Rushbrooke, G. A. Baker Jr., and P. J. Wood, in *Phase Transitions and Critical Phenomena*, Vol. 3, eds. C. Domb and M. S. Green (Academic Press, London and New York, 1974), Chap. 5, pp. 245–356.

[35] For a review, see A. P. Ramirez, Annu. Rev. Mater. Sci. **24**, 453 (1994).

[36] J. S. Smart, *Effective Field Theories of Magnetism* (W. B. Saunders, Philadelphia, 1966).

[37] S. L. Bud'ko, N. Ni, and P. C. Canfield, Phil. Mag. **90**, 1219 (2010).

[38] R. Mittal, S. K. Mishra, S. L. Chaplot, S. V. Ovsyannikov, E. Greenberg, D. M. Trots, L. Dubrovinsky, Y. Su, Th. Brueckel, S. Matsuishi, H. Hosono, and G. Garbarino, Phys. Rev. B **83**, 054503 (2011).

[39] P. W. Anderson, Phys. Rev. **86**, 694 (1952).

[40] R. Kubo, Phys. Rev. **87**, 568 (1952).

[41] M. Creutz, Phys. Rev. D **36**, 515 (1987).

[42] M. Takahashi, Phys. Rev. B **40**, 2494 (1989).

[43] D. Hinzke, U. Nowak, and D. A. Garanin, Eur. Phys. J. B **16**, 435 (2000).

[44] N. D. Mermin and H. Wagner, Phys. Rev. Lett. **17**, 1133 (1966); **17**, 1307(E) (1966).

[45] C. Yasuda, S. Todo, K. Hukushima, F. Alet, M. Keller, M. Troyer, and H. Takayama, Phys. Rev. Lett. **94**, 217201 (2005).

[46] I. Juhász Junger, D. Ihle, and J. Richter, Phys. Rev. B **80**, 064425 (2009).

[47] M. Troyer, B. Ammon, and E. Heeb, Lect. Notes Comput. Sci. **1505**, 191 (1998).

[48] A. F. Albuquerque, F. Alet, P. Corboz, P. Dayal, A. Feiguin, S. Fuchs, L. Gamper, E. Gull, S. Gürtler, A. Honecker, R. Igarashi, M. Körner, A. Kozhevnikov, A. Läuchli, S. R. Manmana, M. Matsumoto, I. P. McCulloch, F. Michel, R. M. Noack, G. Pawłowski, L. Pollet, T. Pruschke, U. Schollwöck, S. Todo, S. Trebst, M. Troyer, P. Werner, and S. Wessel, J. Magn. Magn. Mater. **310**, 1187 (2007).

[49] F. Alet, S. Wessel, and M. Troyer, Phys. Rev. E **71**, 036706 (2005).

[50] O. F. Syljuåsen and A. W. Sandvik, Phys. Rev. E **66**, 046701 (2002).

[51] K. Harada, M. Troyer, and N. Kawashima, J. Phys. Soc. Jpn. **67**, 1130 (1998).

[52] P. Hasenfratz and F. Niedermayer, Z. Phys. B **92**, 91 (1993).

[53] C. J. Hamer, Z. Weihong, and J. Oitmaa, Phys. Rev. B **50**, 6877 (1994).

[54] J.-K. Kim and M. Troyer, Phys. Rev. Lett. **80**, 2705 (1998).

[55] A. W. Sandvik, in *Lectures on the Physics of Strongly Correlated Systems XIV: Fourteenth Training Course*, edited by A. Avella and F. Mancini (American Institute of Physics, New York, 2010), pp. 135–338, and cited references.

[56] As a result of this inconsistency, we recently asked Professor Niedermayer to check the calculations that led to their result in Eq. (97).[52] He kindly agreed and confirmed to us that Eq. (97) is correct, in particular including the T^2 term.

[57] Z. Weihong and C. J. Hamer, Phys. Rev. B **47**, 7961 (1993).

[58] C. P. Hofmann, Phys. Rev. B **81**, 014416 (2010).

[59] K. Kitagawa, N. Katayama, K. Ohgushi, M. Yoshida, and M. Takigawa, J. Phys. Soc. Jpn. **77**, 114709 (2008).

[60] W. W. Simmons, W. J. O'Sullivan, and W. A. Robinson, Phys. Rev. **127**, 1168 (1962).

[61] D. Beeman and P. Pincus, Phys. Rev. **166**, 359 (1968).

[62] M. Belesi, F. Borsa, and A. K. Powell, Phys. Rev. B **74**, 184408 (2006).

[63] R. Nath, Y. Furukawa, F. Borsa, E. E. Kaul, M. Baenitz, C. Geibel, and D. C. Johnston, Phys. Rev. B **80**, 214430 (2009).

[64] R. J. Mahler, A. C. Daniel, and P. T. Parrish, Phys. Rev. Lett. **19**, 85 (1967).

[65] S.-H. Baek, T. Klimczuk, F. Ronning, E. D. Bauer, J. D. Thompson, and N. J. Curro, Phys. Rev. B **78**, 212509 (2008).

[66] S.-H. Baek, N. J. Curro, T. Klimczuk, E. D. Bauer, F. Ronning, and J. D. Thompson, Phys. Rev. B **79**, 052504 (2009).

[67] Y. Nakai, K. Ishida, Y. Kamihara, M. Hirano, and H. Hosono, J. Phys. Soc. Jpn. **77**, 073701 (2008).

[68] K. Matano, Z. A. Ren, X. L. Dong, L. L. Sun, Z. X. Zhao, and G.-Q. Zheng, Europhys. Lett. **83**, 57001 (2008).

[69] C. Kittel, *Quantum Theory of Solids* (Wiley, New York, 1987).

[70] T. Moriya, *Spin Fluctuations in Itinerant Electron Magnetism* (Springer-Verlag, Berlin, 1985).

[71] V. P. Antropov, B. N. Harmon, and A. N. Smirnov, J. Magn. Magn. Mater. **200**, 148 (1999).

[72] T. Kotani and M. van Schilfgaarde, Phys. Rev. B **81**, 125117 (2010).

[73] V. P. Antropov, J. Magn. Magn. Mater. **262**, L192 (2003).

[74] V. P. Antropov, M. van Schilfgaarde, S. Brink, and J. L. Xu, J. Appl. Phys. **99**, 08F507 (2006).

[75] K. D. Belashchenko and V. P. Antropov, Phys. Rev. B **78**, 212505 (2008).

[76] C. J. Hamer, Z. Weihong, and P. Arndt, Phys. Rev. B **46**, 6276 (1992).

[77] J. Igarashi, Phys. Rev. B **46**, 10763 (1992).

[78] P. Chandra and B. Doucot, Phys. Rev. B **38**, 9335 (1988).

[79] S. Chakravarty, B. I. Halperin, and D. R. Nelson, Phys. Rev. B **39**, 2344 (1989).

[80] A. L. Chernyshev and M. E. Zhitomirsky, Phys. Rev. B **79**, 144416 (2009).

[81] The second-order data in Fig. 32(b) for $J_c/J_1 = 0.1$ and $j_2 \equiv J_2/J_1 = 0$ to 0.42 are described by $S - \langle S \rangle = 0.127\,76 + 0.1747\,4j_2 - 0.026\,127j_2^2 + 1.0365j_2^3$ with an rms deviation of 2.1×10^{-4}.

[82] N. Ni, E. Climent-Pascual, S. Jia, Q. Huang, and R. J. Cava, Phys. Rev. B **82**, 214419 (2010).

[83] M. J. Martínez-Lope, J. A. Alonso, and M. T. Casais, Z. Naturforsch. **58b**, 571 (2003).

[84] Y. Noda, H. Kimura, S. Komiyama, R. Kiyanagi, A. Kojima, I. Yamada, Y. Morii, N. Minakawa, and N. Takesue, Appl. Phys. A **74**, S121 (2002).

[85] K. Marty, A. D. Christianson, C. H. Wang, M. Matsuda, H. Cao, L. H. VanBebber, J. L. Zarestky, D. J. Singh, A. S. Sefat, and M. D. Lumsden, Phys. Rev. B **83**, 060509 (2011).

[86] M. G. Kim, A. Kreyssig, A. Thaler, D. K. Pratt, W. Tian, J. L. Zarestky, M. A. Green, S. L. Bud'ko, P. C. Canfield, R. J. McQueeney, and A. I. Goldman, Phys. Rev. B **82**, 220503 (2010).